Utah State University

DigitalCommons@USU

8-2021

Passive Cavity Deflation after Water Entry Facilitated by a Vented Tube

Emma R. Fraley
Utah State University

Follow this and additional works at: https://digitalcommons.usu.edu/etd

Part of the Aerospace Engineering Commons

PASSIVE CAVITY DEFLATION AFTER WATER ENTRY FACILITATED BY A

VENTED TUBE

by

Emma R. Fraley

A thesis submitted in partial fulfillment
of the requirements for the degree

of

MASTER OF SCIENCE

in

Aerospace Engineering

Approved:

_____   _____
Tadd T. Truscott, PhD   Doug Hunsaker, PhD
Major Professor   Committee Member

_____   _____
Kelli Hendrickson, PhD   D. Richard Cutler, Ph.D.
Committee Member   Interim Vice Provost of Graduate Studies

UTAH STATE UNIVERSITY
Logan, Utah

2021

ABSTRACT

Passive Cavity Deflation after Water Entry Facilitated by a Vented Tube

by

Emma R. Fraley, Master of Science

Utah State University, 2021

Major Professor: Tadd T. Truscott, PhD
Department: Mechanical and Aerospace Engineering

When objects enter water, air cavities form and persist deep underwater. Cavities decrease drag for energy saving applications but there are instances where it is beneficial to dissipate cavities before they collapse naturally. This research proposes a method of cavity dissipation by means of cavity deflation. To facilitate cavity deflation after water entry, a tube with radial vent holes is attached to a projectile. The radial vent holes are located near the projectile, where the cavity forms, to provide the air in the cavity a means to escape after deep seal pinch-off. High-speed camera images and image processing are used to quantify and compare cavity size for spherical projectiles with and without a vented tube. Different vented tube lengths, vented tube diameters, vent hole areas, and impact velocities are compared. If the vented tube is longer than the lower cavity at deep seal pinch-off, the cavity will deflate. As vented tube length and vented tube diameter increase, the amount of cavity deflation increases. Similarly, as vent hole area increases, the amount of cavity deflation increases up to a limit and then the vented tube fills with water before the cavity can fully deflate. The effect of impact velocity on the amount of cavity deflation varies depending on the vented tube length. The critical vented tube length required for deflation to occur is a function of sphere radius, impact velocity, and vented tube diameter. When

comparing acoustic signals and acceleration profiles for deflating cavities and non-deflating cavities, cavity deflation reduces both noise and acceleration after deep seal.

(115 pages)

PUBLIC ABSTRACT

Passive Cavity Deflation after Water Entry Facilitated by a Vented Tube

Emma R. Fraley

When an object enters water, a crater, or air cavity, can form around the object and remain attached as the object travels underwater. Cavities can be beneficial and reduce drag force but there may be times when the cavity needs to be removed. This research proposes a method to remove air cavities by letting air leave the cavity, deflating the cavity similar to how a balloon is deflated. To provide air a path to leave the cavity, a tube with vent holes is attached to the object. The vent holes are located near the object, where the air cavity forms, and allow the air to move from the cavity out through the tube. Cavities for objects with and without the vented tube are compared using images from a high-speed cameras. Different vented tube lengths, vented tube diameters, vent hole areas, and impact velocities are compared. If the vented tube is long enough that it is outside of the cavity then the air will leave and the cavity deflates. As the vented tube length and vented tube diameter increase, the amount of air that leaves the cavity increases. Similarly as vent hole area increases, the amount of air that leaves the cavity increases until the holes get too large and the cavity fills with water before all the air can leave, trapping the remaining air in the cavity. How impact velocity effects the amount of air that leaves the cavity depends on the vented tube length. The critical vented tube length required for deflation to occur depends on the sphere radius, impact velocity, and vented tube diameter. The noise the cavity makes and the acceleration of the object as it travels underwater are compared for deflating cavities and non-deflating cavities and the results show that cavity deflation reduces both noise and acceleration.

ACKNOWLEDGEMENTS

I would first like to thank my advisor Dr. Tadd Truscott for bringing me on as a grad student during unexpected circumstances and for his expertise, guidance, support, and mentorship throughout this project.

I would like to thank my committee members Kelli Hendrickson and Doug Hunsaker for their guidance on and support of this project. I would also like to thank Kelli Hendrickson for proposing the topic of this research.

I would like to thank my original advisor Dr. Areti Kiara, I wish we had been able to work together longer.

I would like thank the members of the Splash Lab for their assistance and support. In particular I would like to thank Rafsan Rabbi for his expertise and guidance throughout this project.

Finally, I would like to thank my parents and sister for their love and support over these past three years.

CONTENTS

LIST OF TABLES

LIST OF FIGURES

CHAPTER 1

INTRODUCTION

When objects enter water, air cavities can form. Understanding the cavities formed after water entry is important for military applications such as air-to-sea ballistics [5]. Cavities can be desired as they can reduce projectile drag [6] which has energy saving benefits. There may be instances though where cavities need to be dissipated before they collapse naturally due to hydrostatic pressure. This thesis proposes a method for the dissipation of cavities formed after water entry by passive cavity deflation. To facilitate cavity deflation after water entry, a tube with radial vent holes is attached to a projectile. The radial vent holes are located near the projectile, where the cavity forms, to provide the air in the cavity a means to escape after pinch-off.

Cavity deflation is a new area of study and this proof of concept research focuses on the deflation of cavities formed by air-entrainment around a spherical projectile to gain an introductory understanding of cavity deflation after water entry. Three different cavity deflation measurements are presented in this thesis: cavity area, acoustic, and acceleration. The goals of the cavity area study are to compare the cavity sizes of deflating cavities and non-deflating cavities, to determine what parameters affect the time and amount of cavity deflation, and to find the critical vented tube length required for cavity deflation to occur. The goal of the acoustic study is to compare the acoustic signals of deflating cavities and non-deflating cavities to determine how cavity deflation affects water entry acoustics. Similarly, the goal of the acceleration study is to compare the acceleration profiles of deflating cavities and non-deflating cavities to determine how cavity deflation affects water entry acceleration.

1.1 Background

This section provides a brief overview of water entry and then reviews prior studies on cavity dynamics, acoustics, and forces. The section concludes with potential reasons for

cavity dissipation after water entry as well as a review of prior studies on the manipulation of cavity size.

When a sphere impacts a water surface, the sphere displaces the water and a thin, upward-moving film forms around the sphere, known as a splash crown (Fig. 1.1(a)). As the sphere descends below the free surface, air from above is entrained behind the sphere, forming a cavity (Fig. 1.1(b)). As the sphere continues to descend the hydrostatic pressure causes the cavity walls to collapse inward until the walls touch one another at a single point, an event known as pinch-off, (Fig. 1.1(c)) and the cavity splits into an upper and a lower cavity. At the pinch-off point, two jets are formed due to the high pressure. One jet moves upwards through the upper cavity to the atmosphere and the other moves downward through the lower cavity until it impacts the sphere (Fig. 1.1(d)).

(a)	(b)	(c)	(d)
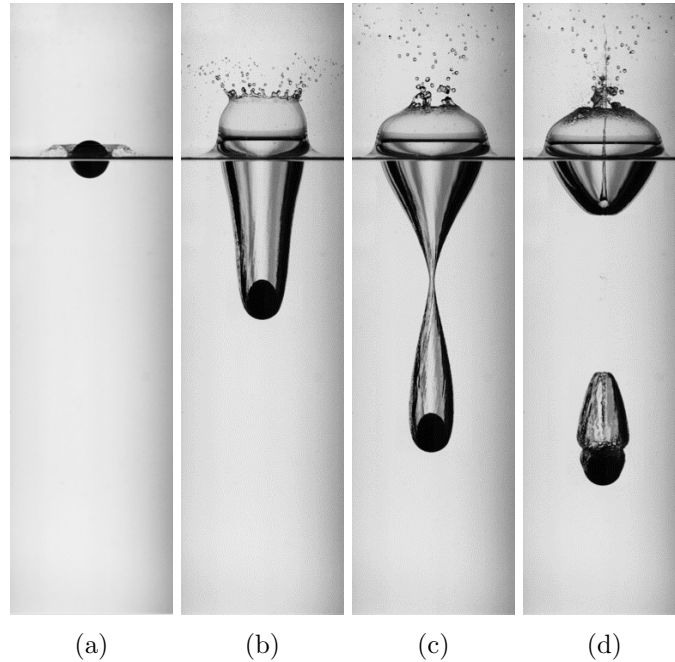
Fig. 1.1: Water entry of a 2.54 cm diameter sphere with a contact angle of 120° and impact velocity of 2.6 m/s. The image sequence shows (a) splash crown formation, (b) air-entrainment cavity formation, (c) pinch-off, and (d) dual jets.

The forces involved in cavity dynamics are gravitational, surface tension, inertial, and viscous [7]. The relative magnitude of these forces are compared with four non-dimensional

parameters: the Bond number $Bo = \rho g R^2/\sigma$, the Weber number $We = \rho U_0^2 R/\sigma$, the Froude number $Fr = U_0^2/gR$, and the Reynolds number $Re = \rho U_0 R/\mu$, where ρ is the fluid density, σ is the surface tension, μ is the viscosity, g is the gravitational acceleration, U_0 is the impact velocity, and R is the radius of the sphere (R can be replaced with another length scale such as sphere diameter D). The Bond number is the ratio of the gravitational force to the surface tension force, the Weber number is the ratio of the inertial force to the surface tension force, the Froude number is the ratio of the inertial force to the gravitational force, and the Reynolds number is the ratio of inertial force to viscous force. These non-dimensional numbers are used to characterize various cavity behaviors.

Duez, et al. [8], examined when air cavities form and found that air cavity formation after water entry depends on impact velocity and contact angle. They found that an air cavity formed when the impact velocity was above a threshold which depends on the contact angle of the projectile. In water, for hydrophillic spheres, which have a contact angle of $\theta < 90°$, there is a constant threshold velocity of around $V = 7$ m/s for air entrainment, below which cavities are not formed. For hydrophobic spheres, which have a contact angle of $\theta > 90°$, the threshold velocity ($V = 7$ m/s) decreases as the contact angle increases from the constant threshold velocity at $\theta = 90°$ to near zero at $\theta = 180°$. As velocity reaches the threshold, or critical velocity, the contact line between the sphere and the water becomes destabilized and the thin film that forms around the sphere during impact detaches which leads to air entertainment and cavity formation. Otherwise the film remains attached to the sphere which does not provide a means for air entrainment and no cavity is formed. The critical velocity is dependent on the contact angle for hydrophobic spheres but only weakly dependent on the contact angle for hydrophillic spheres.

Aristoff and Bush [1] investigated cavity formation for hydrophobic spheres with a contact angle of $120°$. They found that there are four different cavity shapes, or types, that can form. The four different cavity types, which are defined by their pinch-off location and depend on the Bond and Weber numbers, are quasi-static, shallow seal, deep seal, and surface seal. Quasi-static cavities are defined by a pinch-off near the sphere surface and

occur at low Weber numbers. There is minimal air entrainment and the cavity is very small. Shallow seal cavities are defined by pinch-off at a depth on the order of the capillary length and occur at higher Weber numbers and low Bond numbers. The air-entrainment volume is several times larger than the volume of the sphere. Deep seal cavities are defined by a pinch-off depth roughly halfway between the water surface and the sphere and occur at similar Weber numbers as shallow seal but higher Bond numbers. A typical deep seal cavity and a deep seal cavity for a vented tube case are seen in Fig. 1.2(a) and Fig. 1.2(b), respectively. Surface seal cavities are defined by a pinch-off depth of near zero, or near the surface, and occur at the highest Weber numbers. A typical surface seal cavity and a surface seal cavity for a vented tube case are seen in Fig. 1.2(c) and Fig. 1.2(d), respectively. After surface seal occurs, multiple pinch-offs can occur that each decrease the volume of the cavity over time. This thesis will focus on deep seal and surface seal cavities. The Bond and Weber numbers investigated by Aristoff and Bush and resulting cavity regimes are shown in Fig. 1.3, remade from Aristoff and Bush [1] and Speirs, et al [2] with the addition of the Bond and Weber numbers and cavity type for the cavity deflation study, designated by solid markers.

The work of Speirs, et al. [2] expanded upon the work of Duez, et al. and Aristoff and Bush by investigating cavity formation for different contact angles. They found that cavity formation depends on the formation and behavior of the splash crown, and that cavity shape depends on the contact angle as well as the Bond and Weber numbers. For contact angles of $\theta = 86°$ and $\theta = 101°$, surface seal occurs above the critical velocity as predicted by Duez. Just below the critical velocity, no cavities form as expected but as the Weber number continues to decrease, quasi-static cavities form. This is explained by the thick splash crown that forms around the sphere at low Weber numbers. The thick crown moves slowly up the sphere which allows for air entrainment behind the sphere as it descends and quasi-static cavities are formed. As the Weber number increases, the crown thins and the upward velocity increases which causes the crown to move up the sphere faster than it descends, preventing air entrainment and therefore cavity formation. When
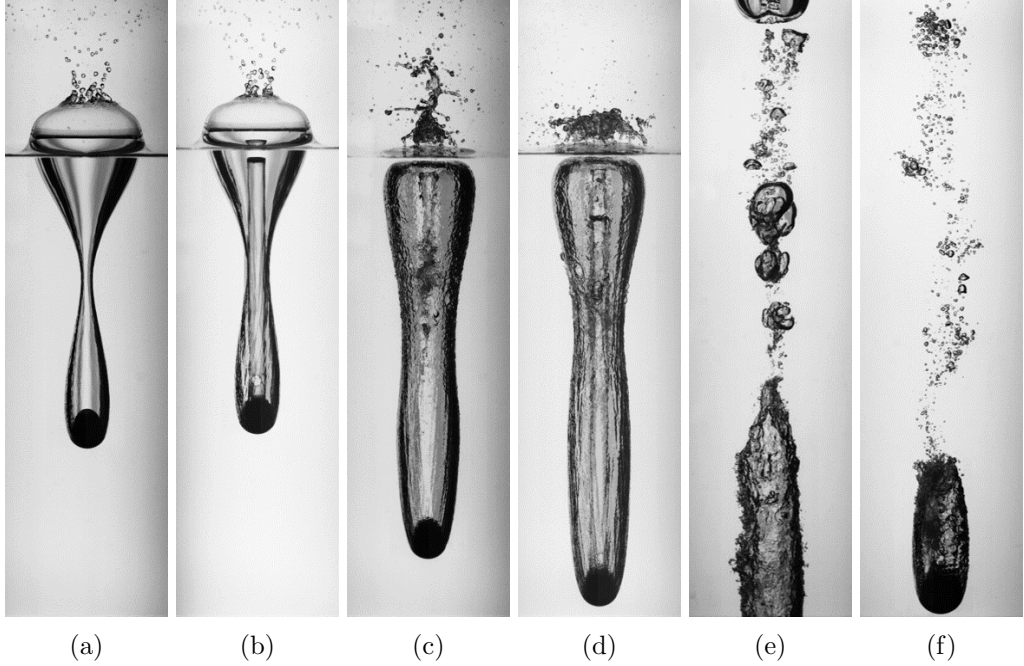
Fig. 1.2: (a) Deep seal cavity. (b) Deep seal cavity for vented tube case. (c) Surface seal cavity. (d) Surface seal cavity for vented tube case. (e) Air-bubble shedding. (f) Air-cloud shedding. For all figures, the sphere diameter is 2.54 cm and the contact angle is 120°. The impact velocity is 2.6 m/s for (a), (b) and (f) and 5.9 m/s for for (c)-(e). The vented tube diameter is 1.27 cm and the the vented tube length is 15.24 cm for (b) and the vented tube diameter is 1.27 cm and the vented tube length is 22.86 cm for (d).

the critical velocity is reached, the splash crown has a high velocity and separates from the sphere which allows for air entrainment and the formation of surface seal cavities. For the lower contact angles investigated, $\theta = 86°$ and $\theta = 101°$, the cavity shapes that form are described above. For a contact angle of $\theta = 141°$ the different cavity shapes occur at similar Bond and Weber numbers as those described by Aristoff and Bush.

Duclaux, et al. [3] developed an analytical solution to model the evolution of a cavity, assuming a sphere with constant velocity, and the theoretical results were compared against experimental data for $1 < Fr < 330$. They found that the pinch-off depth is close to half the depth of the cavity at pinch-off and that the depth of the sphere at pinch-off increases as the square root of the Froude number $Fr^{1/2}$. Duclaux also found that the pinch-off time is independent of impact velocity but increases as the sphere radius increases. The pinch-off times and Froude numbers for the 2.54 cm sphere used in the cavity deflation study are
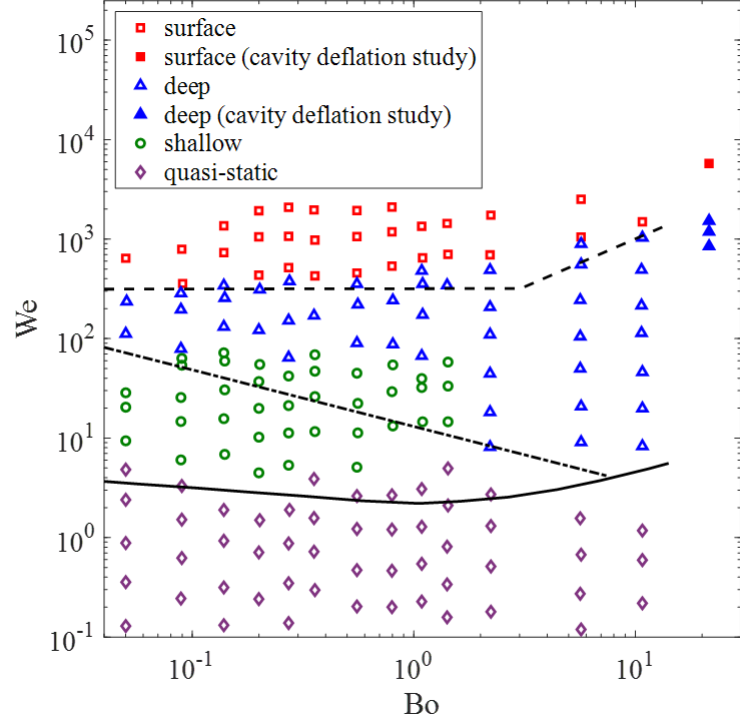
Fig. 1.3: Cavity regimes for $\theta = 120°$ remade from Aristoff and Bush [1] and Speirs, et al [2] with the addition of the Bond and Weber numbers and cavity type for the cavity deflation study, designated by solid markers.

plotted in Fig. 1.4 which shows the pinch-off time is independent of impact velocity. The contact angle is $120°$ and each point is the average pinch-off time for five trials. Aristoff, et al. [9] further developed the cavity evolution model to include the influence of cavity deceleration and compared theoretical results and experimental data for low density spheres for $3 < Fr < 100$. They found that as sphere density decreases, the pinch-off depth and pinch-off time also decrease. The decrease in pinch-off time was found to be small while the decrease in pinch-off depth and depth of the cavity at pinch-off were more noticeable.

Ripples on the surface of descending cavities after pinch-off were first mentioned by Worthington [10]. Grumstrup, et al. [11] studied deep seal air-entrainment cavity ripples and found that the ripples occur after pinch off. They suggest that pressure perturbations caused by pinch-off induce volume oscillations in the cavity. To cancel out oscillations at the projectile body, so that the cavity remains attached to the body, an acoustic wave is reflected off the projectile surface and that acoustic wave is a ripple. Grumstrup, et al. [11]
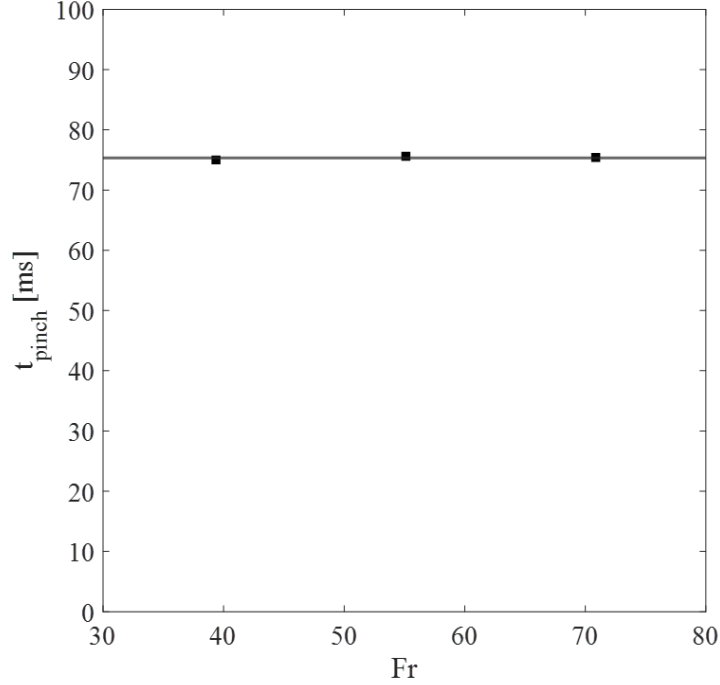
Fig. 1.4: Pinch-off time as a function of Froude number for 2.54 cm diameter sphere used in cavity deflation study. The contact angle is 120° and each point is the average pinch-off time for five trials.

also noted that the amplitude of the ripples decreased as the projectile decreased and that the ripples sometimes induce periodic breakup of the cavity. Bodily, et al. [12] noticed similar ripples formed on cavities behind slender axisymmetric projectiles. Mansoor, et al. [13] investigated extended cavity formation for hydrophobic spheres and observed ripples in their cavities after pinch-off. They also observed the periodic breakup of the cavity due to ripples which they termed "cavity shedding". They found that the crests of the ripples acted as favorable points for cavity closure which created the multiple pinch-off events, or cavity shedding.

Zhang, et al. [14] investigated cavity shedding for deep seal and surface seal cavities ($8 < Bo < 140$, $1700 < We < 15400$) and observed that cavities have two shedding modes: air-bubble shedding and air-cloud shedding. Air-bubble shedding is characterized by the repeated shedding of a large bubble and then consecutive smaller bubbles, where the the release of the smaller bubbles is equal to the frequency of the cavity ripples. Air-bubble

shedding (Fig. 1.2(e)) occurs for surface seal cavities at lower Bond numbers. Air-cloud shedding is characterized by the collapse of the cavity tail which produces a cloud of small bubble. Air-cloud shedding (Fig. 1.2(f)) occurs for surface seal cavities at higher Bond numbers and all deep seal cavities. Zhang, et al. [14] also observed differences in the normalized acoustic signals for deep seal and surface seal cavities. After pinch-off, the acoustic signal for deep seal is dominated by cavity volume pressure oscillations while pressure oscillations due to shedding are observed in the surface seal acoustic signal. Additionally, the amplitude of the acoustic signal after pinch-off is is larger for deep seal than for surface seal. The high pressure at deep seal induces high pressure oscillations in the cavity which cause the cavity tail to collapse, resulting in air-shedding. Surface seal suppresses the pressure oscillations, resulting in the more regular bubble-shedding.

Vakarelski, et al. [6] found, for spheres, that cavity ripples eventually dampen and the cavity reaches a stable-streamlined state. They observed that the cavity stabilization depth increased with sphere density, sphere size, and drop height and ranged from around 1 meter to 2 meters for the cases they tested. They also observed that most of the cavities remain attached and stable as they reached the bottom of the tank. Vararelski, et al. [6] characterized the drag for stable-streamlined bodies and found that the drag coefficient is near-zero and close to an order of magnitude lower than the drag coefficient of similar streamline shaped projectiles and spheres without cavities.

Acoustic signatures of water entry are studied for different projectiles and cavity types to understand how objects can be identified underwater. Uber and Fegan [15] studied acoustic signatures for the water entry of metal spheres, missile shaped projectiles, and bowling balls and found that the dominate frequency occurs at impact and is related to the kinetic energy and shape of the projectile. They predicted that if the dominate frequency of a projectile was detected and the kinetic energy at impact could be estimated, that a projectile type could potentially be identified. Bodily, et al. [12] studied the acoustic signature of slender axisymmetric projectiles with three different nose shapes: cone, ogive, and flat. They found that for the cone and ogive nose that pinch-off has a more prominent

acoustic signature than impact while for the flat nose, impact has a more prominent acoustic signature than pinch-off. Rabbi, et al. [16] investigated the acoustic signature of the different cavity types studied by Aristoff, et al. [1] and Speirs, et al. [2] and found that the acoustic signature is directly related to the seal type.

Studies of water entry forces often focus on the impact force as the sudden deceleration of a projectile at impact can cause structural damage [5]. Shiffman and Spencer [17] developed a theoretical estimate for the impact force of spheres for sphere depths between zero and the radius of the sphere, before cavity formation began. They found that maximum impact force occurs at a sphere depth between 10% and 20% of the sphere radius and their results were experimentally validated for impact velocities of 1 to 3 m/s by Moghisi and Squire [18]. The primary source of the maximum impact force is added mass [5]. There have been many additional studies, both experimental and theoretical, on the impact force of water entry for various projectile shapes [12, 19–25] as well as studies on how to reduce impact forces [4, 26–28].

Other studies of water entry forces look at forces after impact, during the cavity forming phase. Truscott, et al. [29] investigated forces on spheres for non-cavity forming and cavity forming cases. They found that the two cases experience different types of forces and the forces in cavity forming cases are lower than the forces in non-cavity forming cases. Cavities reduce vortex formation and therefore vortex shedding which causes high unsteady forces in non-cavity forming cases. Li, et al. [30] looked at forces on hydrophillic and hydrophobic spheres at cavity forming impact velocities and found that the forces for hydrophillic spheres with cavities are lower than the forces for hydrophobic spheres with cavities. Shepard, et al. [31] investigated forces on spheres for different sphere densities and impact velocities and found that an increase in sphere density or impact velocity leads to a slight decrease in force.

For the cavity deflation study, the impact acceleration peak across all the cases is very similar and all of the cases use hydrophobic spheres and form cavities. The focus for the cavity deflation study is not on early water entry forces but instead on the forces after

pinch-off. Both Bodily, et al. and Louf, et al. looked at forces after pinch-off. Bodily, et al. [12] compared cavity ripple formation after pinch-off for slender axisymmetric bodies with acceleration data and observed oscillations in the acceleration data after pinch-off that corresponded to the formation of cavity ripples. They found that the ripple formation and acceleration oscillation frequencies were similar. They also observed that both the cavity ripples and acceleration oscillations decay over time and that the acceleration data shows decaying oscillations continue even after ripples are no longer noticeable in the images. Louf, et al. [32] compared cavity ripple formation after pinch-off for cones with force data. They found that the wavelength of the force data oscillations after pinch-off were similar to the cavity ripple wavelength and that the amplitude of the force data oscillations after pinch-off were similar to the estimated cavity ripple amplitude based on pressure variation in the cavity.

While the formation of near-zero drag cavities might have important energy saving applications, there may be scenarios where it is beneficial to remove cavities. As mentioned previously, cavity pinch-off and subsequent cavity ripples produce noise which can be detrimental for military applications where it is important to remain undetected. The U.S. Navy's Committee for Undersea Weapons Science and Technology has described the quieting of existing torpedoes as an issue of paramount importance [33]. While outside the scope of this thesis, for high-speed water entry, cavitation can occur. Cavitation is a dynamic process that occurs in regions of a liquid where the local pressure drops below the vapor pressure [34]. The vapor cavities that form collapse when the vapor cavity moves to a region where the local pressure is above the vapor pressure [34]. If collapse occurs close to a solid surface such as torpedo propellers, it can cause material damage [35]. The ability to passively control cavity dissipation could have applications in missile control and performance [36]. Additionally, cavity dissipation could be important in applications where a projectile that enters from the free surface needs to be wetted to operate.

There have been no studies on the dissipation of cavities by cavity deflation but there have been several studies that alter the shape of the cavity which in some cases results in

a reduced cavity. The Aristoff, et al. [9] study on decelerating sphere found that as sphere density decreases, the pinch-off depth approaches the cavity depth at pinch-off which results in a decreased volume of air entrained in the lower cavity at pinch-off. Mathaia, et al. and Truscott, et al. looked at how the nose shape of a projectile affects cavity shape. Mathaia, et al. [37] compared the impact of axisymmetric bodies with concave noses and convex noses. They found that the convex nose produced well defined cavities with a maximum length of about 20 diameters while the concave nose produced two smaller cavities with a maximum length of about 2 diameters. Truscott, et al. [7] looked at how projectile nose shape impacts the cavity shape for four different nose shapes: cone, cusp, ogive, and flat. The conical nose produced slender cavities that remained close to the projectile while the ogive and flat noses produced larger, more open cavities. The cusp nose produced a significantly smaller cavity, similar to the cavity formed by the concave nose.

CHAPTER 2

APPROACH

This chapter describes the equipment and processes used to collect experimental data for the three cavity deflation studies: cavity area, acoustic, and acceleration. The sphere-vented tube device, experimental setup, experimental parameters, and acoustic setup, as well as the inertial measurement unit used in the acceleration study, are described in the following sections.

2.1 Sphere-Vented Tube Device

To facilitate cavity deflation, a sphere-vented tube device, shown in Fig. 2.1(a), is designed. The general design of the sphere-vented tube device is a hollow tube with evenly spaced radial vent holes that is attached to a spherical projectile. The radial vent holes are located near the spherical projectile, where the air cavity is formed, and the goal of the device is to provide the air in the cavity a means to escape after deep seal. For this thesis, the vented tubes are made of poly-carbonate and attached to the spherical projectile with E6000 adhesive. The vented tube lengths (L) vary from 3.81 cm to 22.86 cm, the inner diameters (d) vary from 0.635 cm to 1.27 cm, and the wall thickness is 0.159 cm. Steel rings that have the same inner and outer diameter as the vented tubes and a thickness of 0.3175 cm are attached to the open ends of the vented tube so that the sphere-vented tube device can be held by an electromagnet.

The radial vent holes in the vented tube are machine drilled to ensure accurate dimensions and placement. Most of the vented tubes have a single row of three evenly spaced radial vent holes and the distance from the center of the radial vent holes to the edge of the vented tube that is attached to the projectile is 1.27 cm. Two of the vented tubes have multiple rows of three evenly spaced radial vent holes. The distance between rows, from the center of the radial vent holes in one row to the center of the radial vent holes in the
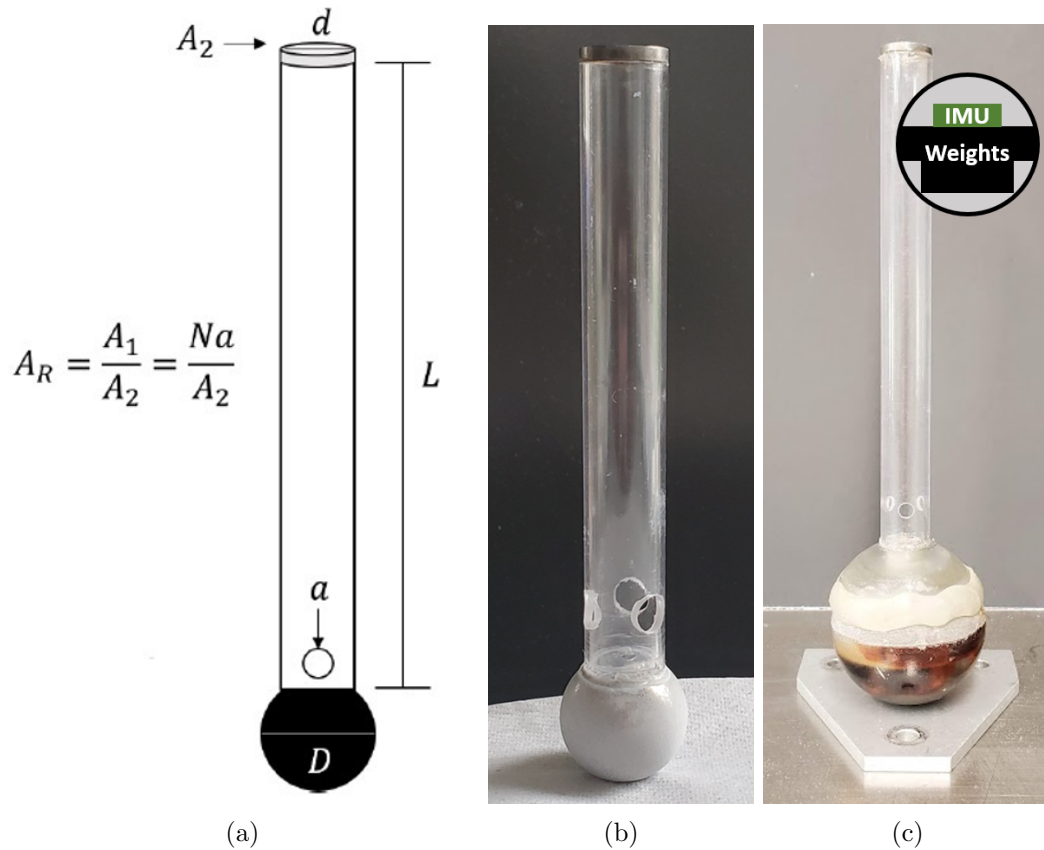
Fig. 2.1: (a) Diagram of basic sphere-vented tube device used to facilitate cavity deflation. (b) Sphere-vented tube device used for cavity area and acoustic studies. (c) Sphere-vented tube device used for acceleration study with an inset diagram showing the IMU inside the sphere.

next row is 1.35 cm and the holes in each row are offset by 60° from the holes in the previous row. The ratio of the combined radial vent hole area (A_1) to the vented tube opening area (A_2) ranges from 0.1 to 10. The combined radial vent hole area is found by multiplying the area of each radial vent hole (a) by the number of radial vent holes (N). A spherical projectile with no vented tube is used as the control and is referred to as a sphere only case.

Fig. 2.1(b) shows the sphere-vented tube device for the cavity area and acoustic studies. The spherical projectile is a 2.54 cm diameter (D) stainless steel sphere. The spheres are cleaned and coated with Cytonix WX2100 which has a contact angle of $116 \pm 7°$. To clean the spheres, they are thoroughly washed with soap and water, dried with a paper towel, and rinsed with ethyl alcohol. Once the spheres are clean they are evenly coated in two layers

of Cytonix WX2100 and left to dry for 24 hours before use. Between every few drops, the old coating is removed with ethyl alcohol and the spheres are cleaned and re-coated.

Fig. 2.1(c) shows the sphere-vented tube device for the acceleration study. The spherical projectile is a 5 cm diameter hollow Vero plastic sphere 3D printed in two parts to hold an inertial measurement unit (IMU). The two parts of the sphere are not halves but rather one third and two thirds of the sphere so the seam between the two parts is above the center of the sphere to reduce the influence of the seam on water entry dynamics. The inset diagram in Fig. 2.1(c) shows the inside of the hollow sphere. Weights are glued into the lower part of the sphere to reduce sphere rotation. The IMU is securely attached to the top of the weights with putty tape and then the two parts of the sphere are sealed with putty tape. The vented tube is centered on the upper part of the sphere. The sealed sphere is cleaned and coated with Glaco Mirror Coat Zero which has a contact angle of $141 \pm 4°$. The same cleaning process described above for the stainless steel spheres is used. Once the sphere is clean it is evenly coated in two layers of Glaco Mirror Coat Zero and left to dry for 1 hour before use. Between every few drops the IMU needs to be recharged which requires the sphere to be unsealed to access the accelerometer. If multiple trials are required for each case, data for all of the trials is taken in one acceleration charge to ensure the putty is consistent across the trials. Once the IMU is charged and the sphere is resealed, the old Glaco Mirror Coat Zero coating is removed with ethyl alcohol and the sphere is cleaned and re-coated.

2.2   Experimental Setup

The experimental setup used for the cavity deflation studies is shown in Fig. 2.2(a). The sphere-vented tube device is dropped from an electromagnet into a 45.7 x 45.7 x 116.8 cm tank of water that is backlit by a light panel. The free surface of the water is 91.4 cm from the bottom of the tank. The impact and subsequent cavity is recorded by two synchronized Phantom Fastcam SA3 high-speed cameras at 1000 frames per second. The image resolution is 1024 by 1024 and the shutter is 1/7500 sec. The electromagnet moves vertically along an 80/20 t-slot aluminum track so that the drop height (h), which determines the impact
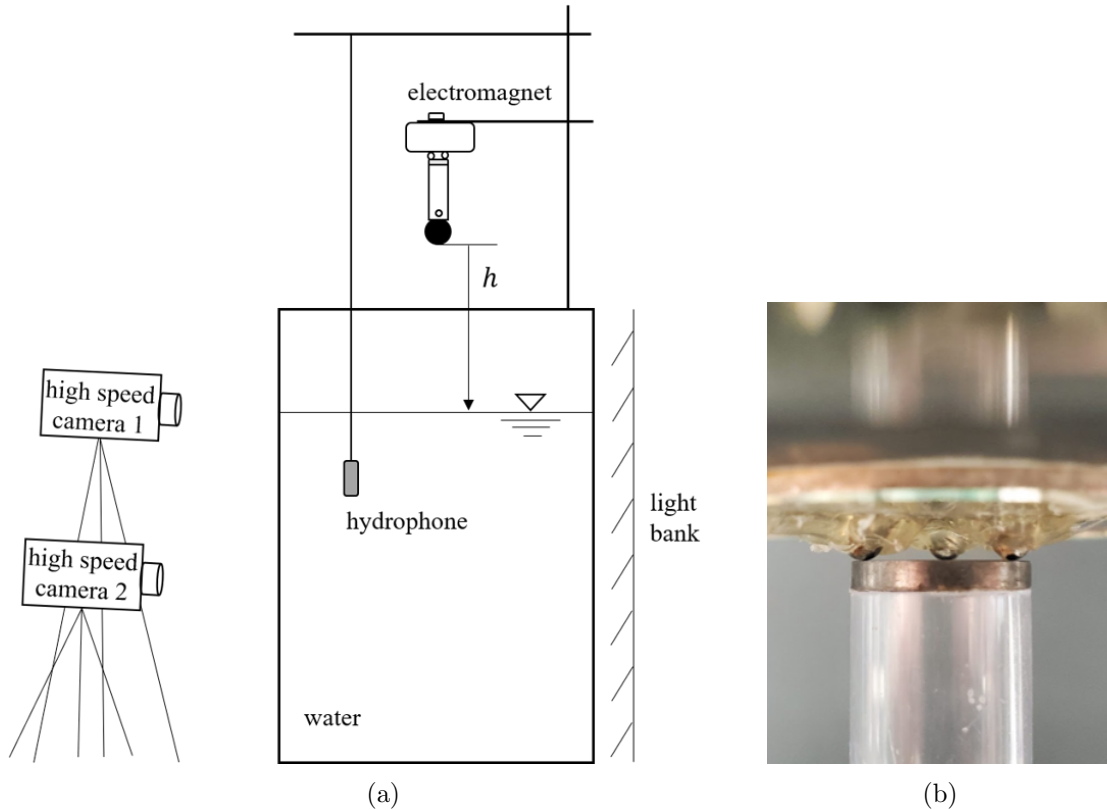
Fig. 2.2: (a) Basic experimental setup for the cavity deflation studies. (b) Close-up view of electromagnet with three small spheres that are used to hold the sphere-vented tube device before it is released.

velocity (U_o), can be adjusted.

To provide an even release of the sphere-vented tube device from the electromagnet, the device is not directly held by the magnet but by three small spheres glued in a triangle at the center of the electromagnet that aligns with the diameter of the steel ring as seen in Fig. 2.2(b). The small spheres are used to reduce the number of contact points which provides a more even release of the sphere-vented tube device and helps ensure that the vented tube remains vertical during the drop. For every drop, the sphere-vented tube device is placed on the electromagnet in the same orientation, with one of the radial vent holes facing the front of the tank. This ensures the same view of deflation is captured for each drop.

2.3   Experimental Parameters

For this introductory cavity deflation study, a small range of vented tube lengths, vented tube diameters, area ratios, and impact velocities are tested to gain an understanding of what parameters affect cavity deflation. The experimental parameters selected for the cavity area, acoustic, and acceleration studies are presented in Table 2.1. The number of cases tested and the number of trials per case for each study are also presented in Table 2.1.

Parameters	Cavity Area Study	Acoustic Study	Acceleration Study
Sphere Diameter D [cm]	2.54	2.54	5
Sphere Contact Angle θ [°]	117 ± 7	117 ± 7	141 ± 4
Drop Height h [m]/ Impact Velocity U_o [m/s]	0.25/2.2 (deep seal), 0.35/2.6 (deep seal), 0.45/3.0 (deep seal), 1.75/5.9 (surface seal)	0.35/2.6 (deep seal)	0.35/2.6 (deep seal)
Vented Tube Diameter d [cm]	0.635, 1.27	1.27	1.27
Vented Tube Length L [cm]	0, 3.81, 7.62, 11.43, 15.24, 22.86	0, 7.62, 11.43, 15.24	0, 7.62, 11.43, 15.24
Area Ratio A_r	0.1, 0.3, 0.5, 1, 2, 4, 10	0.5, 1, 2	0.5, 1, 2
Number of Cases	72	7	7
Number of Trials per Case	5	3	3

Table 2.1: Experimental parameters used for the cavity area, acoustic, and acceleration studies as well as the number of cases tested and the number of trials per case for each study.

2.4   Acoustic Setup

Acoustic data is collected with an Aquarian Audio Products H2a-XLR hydrophone. The hydrophone is horizontally unidirectional and has a sensitivity of -180dB and a useful range of 10 Hz to 100 kHz [38]. The hydrophone signal is recorded with LabVIEW at a

sampling rate of 44100 Hz. To compare the acoustic signal to what is physically occurring during water entry and cavity deflation, the hydrophone data is synchronized with the images from the high-speed cameras. To synchronize the data and images, the camera record state signal is also recorded with LabVIEW. When the camera is not recording, the record state output is set to low (0 V) and when the camera is recording, the record state output is set to high (5 V). The camera trigger mode is set to 'start' so that the first image corresponds with first time in acoustic data after the switch in camera state from low to high.

To position the hydrophone, a horizontal bar, made of 80/20 t-slot aluminum, is attached to the electromagnet track and the hydrophone cord is placed over the horizontal bar. The hydrophone cord is moved up and down over the bar and radially along the bar to set the hydrophone depth and radial position, respectively. To hold the hydrophone in place at a selected position the cord is clamped against the bar.

Preliminary acoustic data was collected to determine the hydrophone placement and effects of reverberations from the tank walls on the acoustic signal.

2.4.1 Hydrophone Placement

The hydrophone placement was selected based on signal strength. To determine the hydrophone placement, acoustic data for a sphere only case was collected at six different hydrophone positions. For each position the depth from the free surface and radial distance from the center of the sphere were adjusted. The six hydrophone positions in relation to a sphere at deep seal depth are shown in Fig. 2.3 and the depth and radial distance for each position are presented in Table 2.2. For all of the hydrophone position data collected the sphere diameter is 2.54 cm, the contact angle is 117°, and the impact velocity is 2.6 m/s.

The acoustic waveforms for the six positions are seen in Fig. 2.4. Each waveform is the average of three trials. It was assumed that the strongest signal would be observed when the hydrophone was closest to the lower cavity at deep seal and the acoustic waveforms (Fig. 2.4) show that this assumption is correct. The amplitude of the oscillations after deep seal increase as the hydrophone moves closer, both in depth and radial position, to the lower
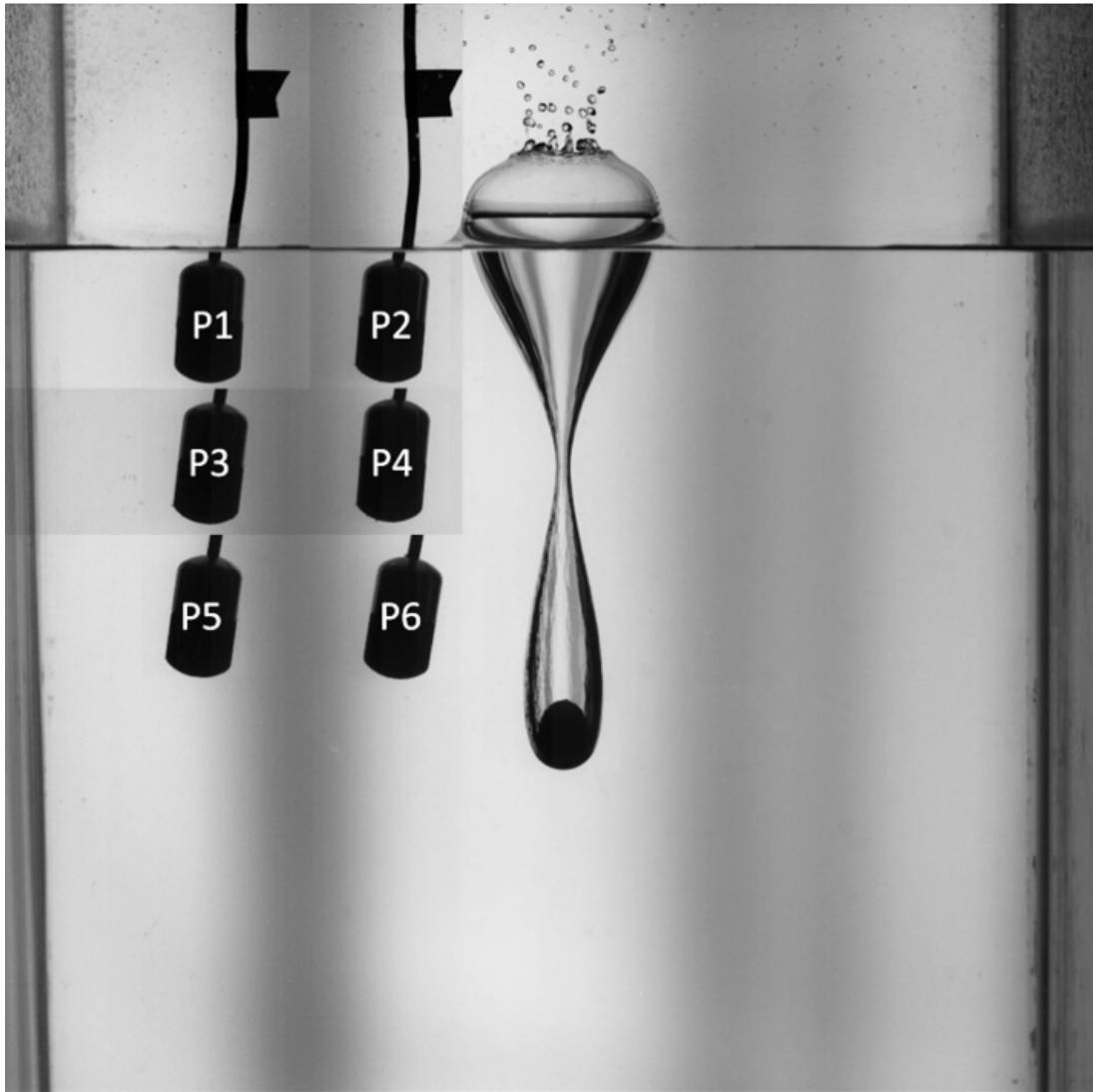
Fig. 2.3: Six hydrophone positions tested to determine the optimal hydrophone position for acoustic data collection. The positions are shown in relation to a sphere at deep seal depth.

Position	P1	P2	P3	P4	P5	P6
Depth [cm]	4	4	10	10	14	14
Radial Distance [cm]	14	7	14	7	14	7

Table 2.2: Depth from the free surface to the bottom of the hydrophone and radial distance from the center of the sphere to the center of the hydrophone for each of the six hydrophone positions tested.
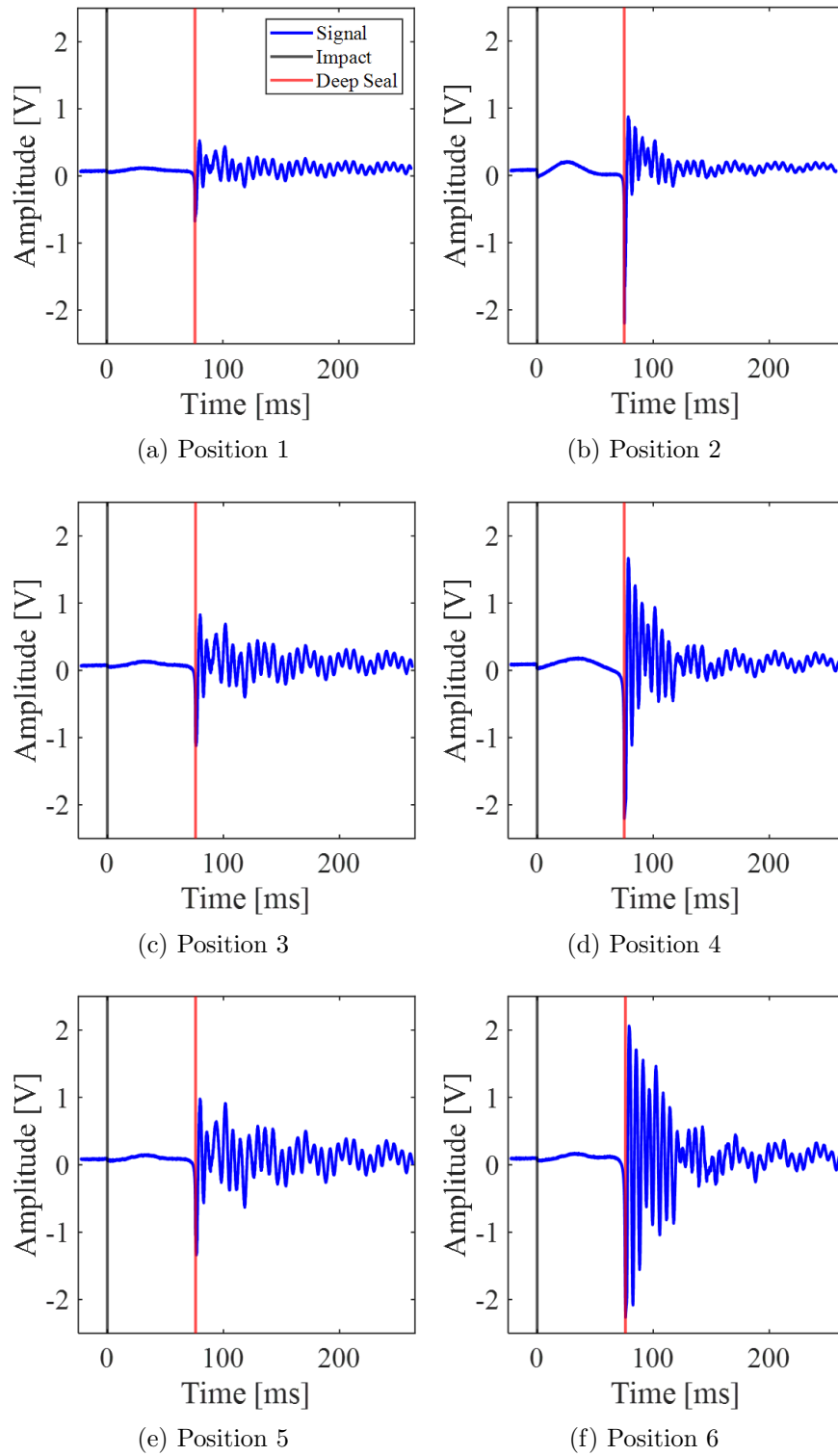
Fig. 2.4: Acoustic waveforms for sphere only case measured at six different hydrophone positions. The black and red lines represent impact time and deep seal time, respectively.

cavity at deep seal. Position 6 (Fig. 2.4(f)) was selected for the hydrophone placement as that is where the strongest signal was observed. For the remainder of this thesis all acoustic data presented is collected at a hydrophone depth of 14 cm from the free surface and radial position of 7 cm from the center of the sphere.

The power spectrums for the six positions are seen in Fig. 2.5. Each power spectrum is the average of three trials. The signal was cropped from 0 to 250 ms for the power spectrum so that the number of points used in the fft is 0.25% of the sampling frequency and the power was normalized from 0 to 1 by the maximum value of position 6. The power spectrum frequency was cropped at 0.4 kHz as higher frequencies provide no useful information. The dominate frequencies are similar across the six hydrophone positions but the power varies by position, generally increasing as the hydrophone moves closer to the lower cavity at deep seal.

Minnaert [39] observed that air bubbles surrounded by water pulsate when they close and developed a formula to estimate the pulsation frequency, know as the Minnaert resonance. The Minnaert resonance formula is

$$f = \frac{1}{2\pi r} \left(\frac{3\gamma P_\infty}{\rho} \right)^{1/2} \tag{2.1}$$

where r is radius of the bubble, γ is specific heat ratio, P_∞ is ambient pressure, and ρ is water density. The frequency of the lower cavity immediately after deep seal was estimated using (2.1), assuming the cavity volume is spherical. The estimated Minnaert frequency is between 164 and 166 Hz for all six hydrophone positions which is close to the frequency peak of 172 Hz in the power spectrums (Fig. 2.5). The power spectrums show that the power at 172 Hz increases as the hydrophone moves closer, both in depth and radial position, to the lower cavity at deep seal. This follows the expected behavior for the Minnaert frequency: as the hydrophone moves closer to the lower cavity, source of the pulsations, the Minnaert frequency increases in strength. Similar to the waveform results, the strongest Minnaert frequency is observed at position 6 (Fig. 2.5(f)), the selected hydrophone position.

(a) Position 1

(b) Position 2

(c) Position 3

(d) Position 4

(e) Position 5
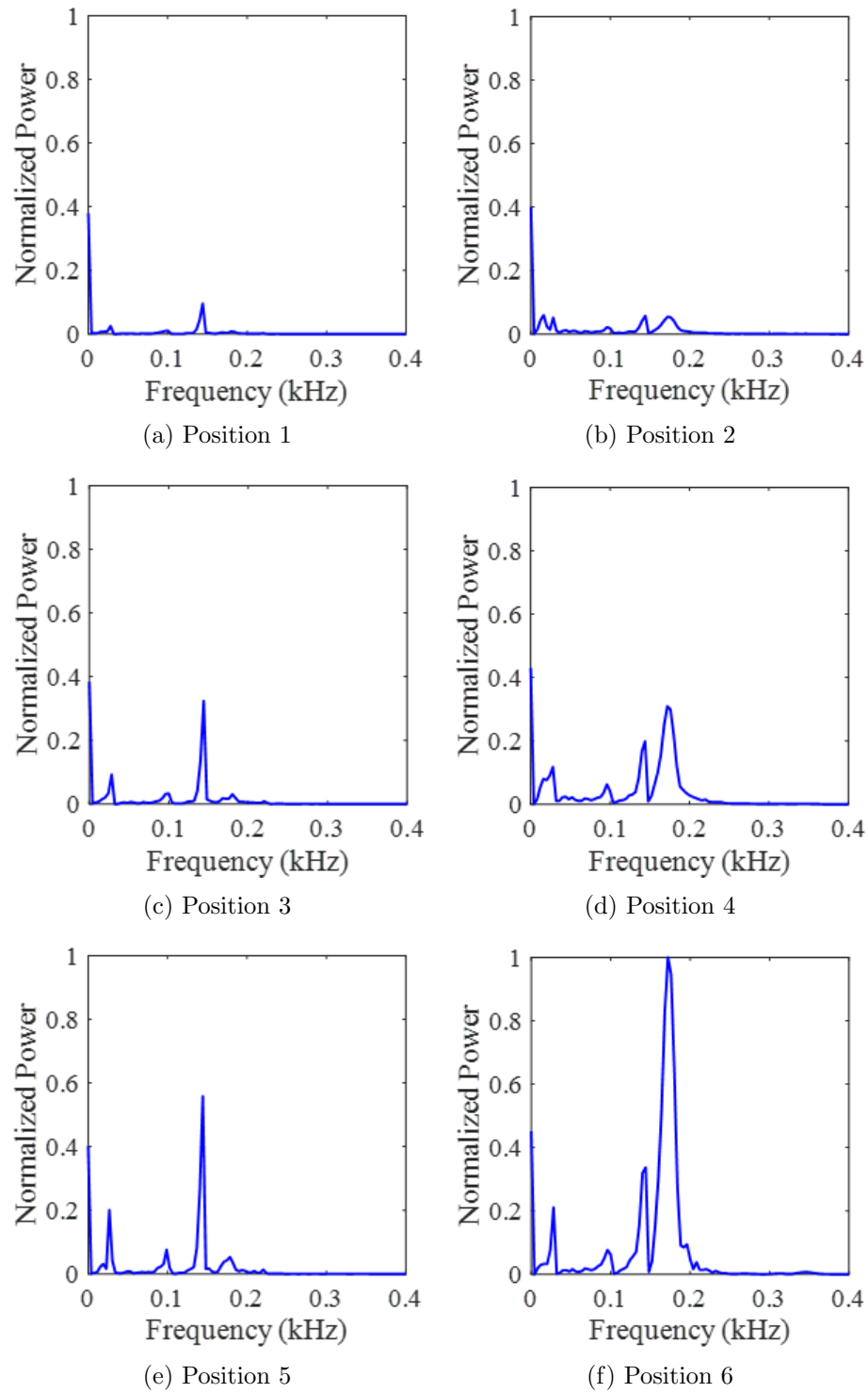
(f) Position 6

Fig. 2.5: Power spectrums for sphere only case measured at six different hydrophone positions. The frequency is cropped at 0.4 kHz as higher frequencies provide no useful information.

2.4.2 Tank Reverberations

To determine the effect of reverberations from the tank walls on the acoustic signal, data collected in a bare tank for a sphere only case was compared with data collected in a mass loaded vinyl (MLV) lined tank for a sphere only case. The bare tank setup is the same as the experimental setup described in Section 2.2 and seen in Fig. 2.2(a). The MLV lined tank setup is similar to the experimental setup described in Section 2.2 and seen in Fig. 2.2(a) except that the tank walls and bottom of the tank are lined with MLV, an acoustic damping material. Additionally, the high-speed cameras are not used as the damping material blocks their view. For all of the tank reverberation data collected the sphere diameter is 2.54 cm, the contact angle is 117°, and the impact velocity is 2.6 m/s.

The acoustic waveforms and power spectrums for a sphere only case dropped in a bare tank and in a MLV lined tank are seen in Fig. 2.6(a) and Fig. 2.6(b) respectively. Each waveform and power spectrum is the average of three trials. The signal was cropped from 0 to 250 ms for the power spectrums so that the number of points used in the fft is 0.25% of the sampling frequency and the power was normalized from 0 to 1 by the maximum value of the bare tank signal. The power spectrum frequency was cropped at 0.4 kHz as higher frequencies provide no useful information. The acoustic waveforms (Fig. 2.6(a)) show that the oscillations in the acoustic signals for the bare and MLV lined tanks are almost identical while the amplitude of acoustic signal decreases slightly with the addition of MLV, indicating that MLV does have some damping effect on the tank reverberations. To qualitatively compare the damping effect of MLV on the acoustic signal, the amplitudes of the two waveforms were normalized between -1 and 1 and the RMS of the amplitude was calculated for each waveform. The difference between the two RMS values is 20% which means that the addition of MLV damps the acoustic signal by 20% compared to the bare tank. The power spectrums (Fig. 2.6(b)) show that the dominate frequencies are the same for both the bare and MLV lined tanks. Similar to the acoustic waveform amplitude, the power decreases slightly with the addition of MLV. The difference between the RMS values of the normalized power is 32%.
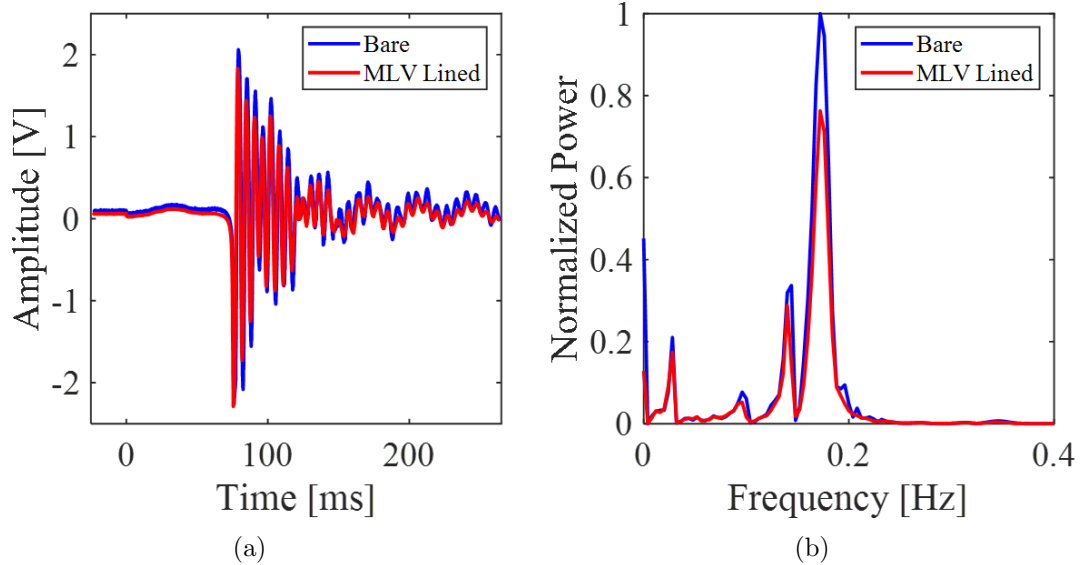
Fig. 2.6: Comparison of (a) acoustic waveform and (b) power spectrum for a sphere only case dropped in a bare tank (blue) and in a mass loaded vinyl lined tank (red). The power spectrum frequency is cropped at 0.4 kHz as higher frequencies provide no useful information.

While the MLV lined tank did damp the signal, the bare tank was selected since the difference between the two acoustic signals at the selected hydrophone position was not drastic and the bare tank allows for the synchronized collection of acoustic data and high-speed camera images.

2.5 Inertial Measurement Unit

The inertial measurement unit (IMU) was built in-house and includes a STMicro-electronics H3LIS331DL high-range accelerometer chip and a InvenSense Inc. MPU-9250 MotionTracking device that consists of a low-range accelerometer, a gyroscope, and a magnetometer. The low-range accelerometer is the only sensor used for this study and has a measurement range of ±16 g, sensitivity scale factor of $2,048$ LSB/g, nonlinearity of $\pm0.5\%$, cross-axis sensitivity of $\pm2\%$, and sampling rate set at 1000 Hz [40]. The low-range accelerometer has been used in two recently published studies [27] [4].

CHAPTER 3

CAVITY AREA STUDY

This chapter presents the data processing methods and results for the cavity area study. The parameters for this study are presented in Table 2.1. For all cases presented in this chapter the sphere diameter is $D = 2.54$ cm and the contact angle is $\theta = 117°$.

3.1 Data Processing

To quantify cavity deflation for this study, cavity area is estimated using an image processing code written in MATLAB. This section firsts describes the image processing code and then presents an example cavity area plot to highlight important features. Finally, this section discusses why multiple trials are conducted for each case and why cavity area is selected to quantify cavity deflation.

3.1.1 Image Processing

Cavity area is used to quantify cavity deflation due to the planar view of the cavity captured by the high-speed camera images. Further detail about why cavity area rather than cavity volume is selected to quantify cavity deflation is discussed in Section 3.1.4. Both the time frame and what area is being tracked were considered as the image processing code was developed. The time frame selected to estimate the cavity area over is from the first frame the sphere is fully submerged to the last frame the sphere is fully in the lower camera's view. The first frame after the sphere is fully submerged is selected rather than impact due to how the images are processed and all that is missed from starting at this frame is the first few milliseconds of cavity formation. Fig. 3.1 highlights what areas are tracked during the image processing. The red trace outlines the area of the cavity that is being tracked at the sphere descends. While the sphere is not technically part of the cavity it is tracked with the cavity to simplify the image processing and then subtracted later. Before and at
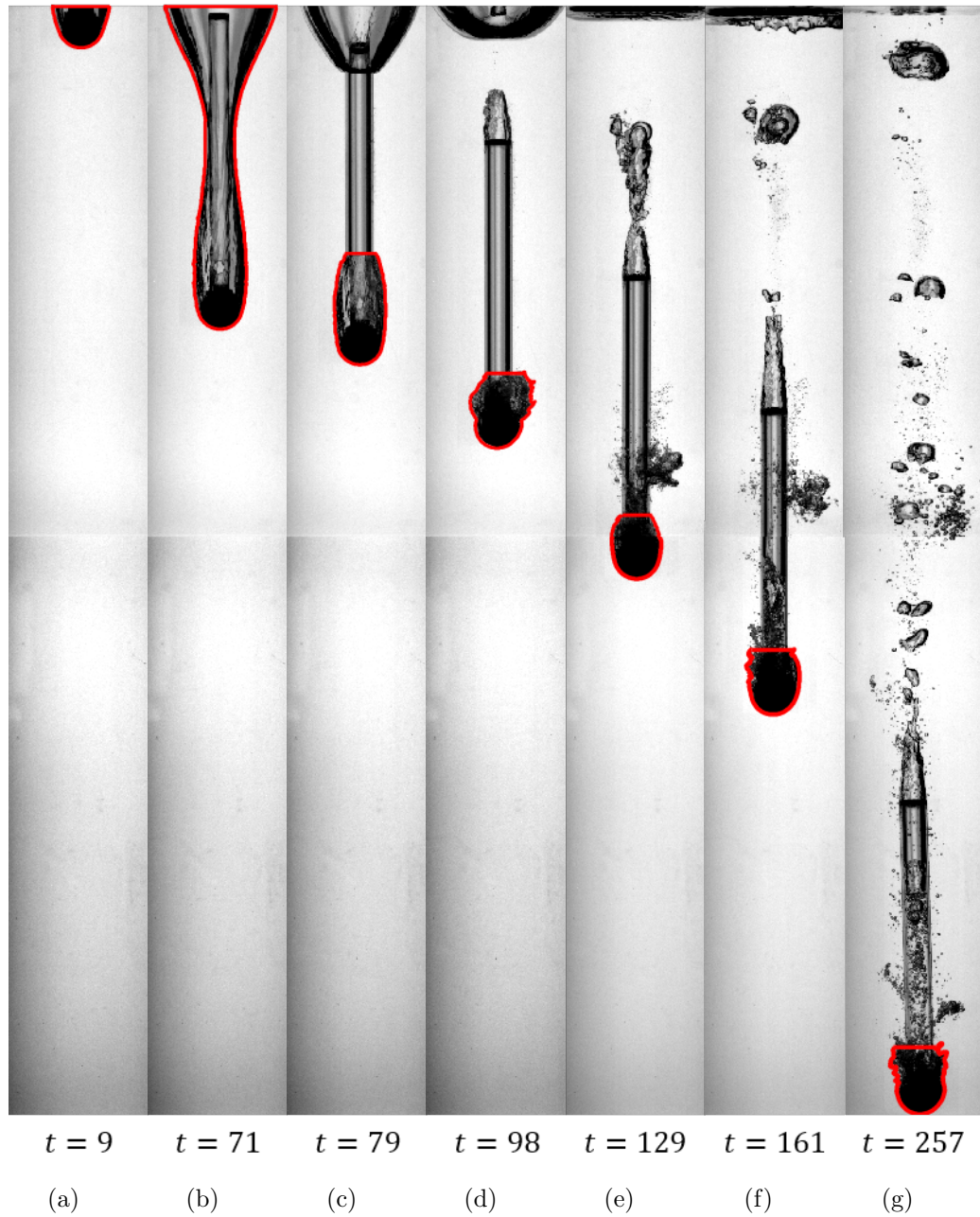
Fig. 3.1: High-speed camera images of a sphere-vented tube device, times from impact as marked. The impact velocity is $U_o = 2.6$ m/s, the sphere diameter is $D = 2.54$ cm, the contact angle is $\theta = 117°$, the vented tube diameter $d = 1.27$ cm, the vented tube length is $L = 15.24$ cm, and the area ratio is $A_r = 1$. The red trace outlines the area of the cavity that is being tracked at the sphere descends.

deep seal, the entire cavity, from the free surface to the bottom of the sphere, is tracked (Fig. 3.1(a)-(b)). After deep seal, only the lower cavity and the portion of the vented tube inside the lower cavity are tracked (Fig. 3.1(c)-(g)). The portion of the vented tube inside the lower cavity is included in the cavity area estimation as the air inside that part of the vented tube would be part of the cavity if the vented tube was not there. The portion of vented tube outside of the cavity, the air bubble at the top of the vented tube, and the upper cavity are not tracked after deep seal for this study since the focus is on the deflation of the lower cavity.

To estimate the cavity area for an image, the image is first cropped. The upper camera (C1) images are cropped at the average free surface as this study is only interested in the cavity below the surface. The lower camera (C2) images are cropped to remove any overlap between the bottom of C1 and the top of C2. For both cameras the images are also cropped close to the sides of the cavity to reduce the data processing time. To calculate the average free surface the first image of the dataset is used, before the water had been disturbed by impact. A morphological matrix converts the C1 image from gray scale to binary so that the free surface is made up of nonzero pixels and the air above and water below the surface are made up of zero-valued pixels. The bottom of the free surface is then the maximum nonzero pixel in each column of pixels. Two free surface points ($0.125 \times$ image width from the left and right edges) are selected and these values are averaged to get the average free surface.

To remove overlap between the two cameras, the last image that the entire sphere is in C1's view is used. A morphological matrix converts the C1 image from gray scale to binary so that the cavity and sphere is made up of nonzero pixels and the background is made up of zero-valued pixels. The maximum nonzero pixels out of all the columns represents the bottom of the sphere and the pixel distance from the bottom of the sphere to the bottom of the image is calculated. This pixel distance is converted to inches using the C1 calibration factor. A morphological matrix converts the corresponding C2 image from gray scale to binary so that the bottom of the sphere that overlaps between images is made up of

nonzero pixels and the background is made up of zero pixels. The distance from the bottom of the sphere to the bottom of the C1 image in inches is converted to the C2 pixel distance using the C2 calibration factor. The C2 pixel distance is then added to the bottom of the sphere (maximum nonzero pixel out of all the columns) in the C2 image and the distance from the top of the image to this point is the overlap between the two cameras.

Once an image is cropped, a morphological operation is used to convert the image from gray-scale to binary so that the cavity and sphere-vented tube device is made up of nonzero pixels and the background is made up zero pixels. For each row of pixels from the top of the cavity to the bottom of the sphere, the first nonzero pixel is subtracted from the last nonzero pixel to find the diameter for that row of pixels. The diameters, from each row of pixels, are summed together to calculate the planar area of the cavity and sphere in pixels^2. The pixel area is calculated for each frame for both the C1 and C2 images. The C1 and C2 pixel areas are converted to cm^2 using the C1 and C2 calibration factors, respectively. For each frame the converted areas from C1 and C2 are then added together to account for frames where the cavity is split between the two cameras (Fig. 3.1(e)). Finally, the area of the sphere is subtracted to get the area of the cavity only.

To compute the calibration factors used to convert between pixels and standard dimensions, a calibration image is taken for each dataset which is an image of a ruler placed vertically in the tank of water. In MATLAB, two inch markers on the image of the ruler are user selected and the number of inches between the two markers is input. The difference in vertical pixels between the two selected points are divided by the number of inches between the two points to get a calibration factor of pixels per inch. Unit conversions are then used to convert pixels in^{-1} to pixels cm^{-1}. Separate calibration factors are calculated for C1 and C2. To ensure there was no distortion due to the slight angle of the camera, for a few datasets for each camera the calibration factor was computed for each set of inch markers on the image of the ruler and the values were compared with each other. The error was not greater than one or two pixels, the bias due to human error, so it was determined that any effect due to distortion was within the error of the measurement. For the data presented in

this thesis the first method described in this paragraph is used to compute the calibration factors.

3.1.2   Example Cavity Area Plot

Cavity area over time is plotted in Fig. 3.2(c) for a sphere only case and a vented tube case. For each case one trial is plotted. For both cases the impact velocity is $U_o = 2.6$ m/s. For the vented tube case the vented tube diameter is $d = 1.27$ cm, the vented tube length is $L = 15.24$ cm, and the area ratio is $A_r = 1$. Corresponding image sequences for the sphere only and the vented tube cases are presented in Fig. 3.2(a) and Fig. 3.2(b), respectively. The image sequences are outlined in the line color and style of the corresponding case in the cavity area plot. Fig. 3.2 is used to highlight important features of the cavity area results that will be presented Section 3.2.

The image sequences (Fig. 3.2(a)-(b)) start at deep seal and the time between frames is 15 ms. In the cavity area plot (Fig. 3.2(c)), deep seal, which is marked by the vertical red line, occurs at $t = 0$ ms. Deep seal is selected as the starting time for this study rather than impact which is traditionally used in water entry studies as the focus of this study is cavity deflation which begins immediately after deep seal for vented tube cases. Aligning all of the cases at deep seal makes it easier to directly compare the time and amount of deflation. For all of the cavity area plots presented in this thesis, deep seal occurs at $t = 0$ ms with impact and cavity formation occurring in the past.

Fig. 3.2(c) shows that deep seal for the vented tube case occurs 5 ms before deep seal for the sphere only case. This is explained in the first frame of the two image sequences (Fig. 3.2(a)-(b)). For the sphere only case, deep seal occurs when the walls of the cavity touch at one point. For the vented tube case, the walls of the cavity touch the vented tube before they can touch at one point which causes an early deep seal pinch-off. Deep seal for the vented tube case is more abrupt than for the sphere only case as there is only a slight decrease in cavity area before the cavity walls touch the vented tube compared to the greater decrease in cavity area before the walls of the cavity touch naturally. The slight difference in deep seal between the sphere only and vented tube cases does not impact aligning the
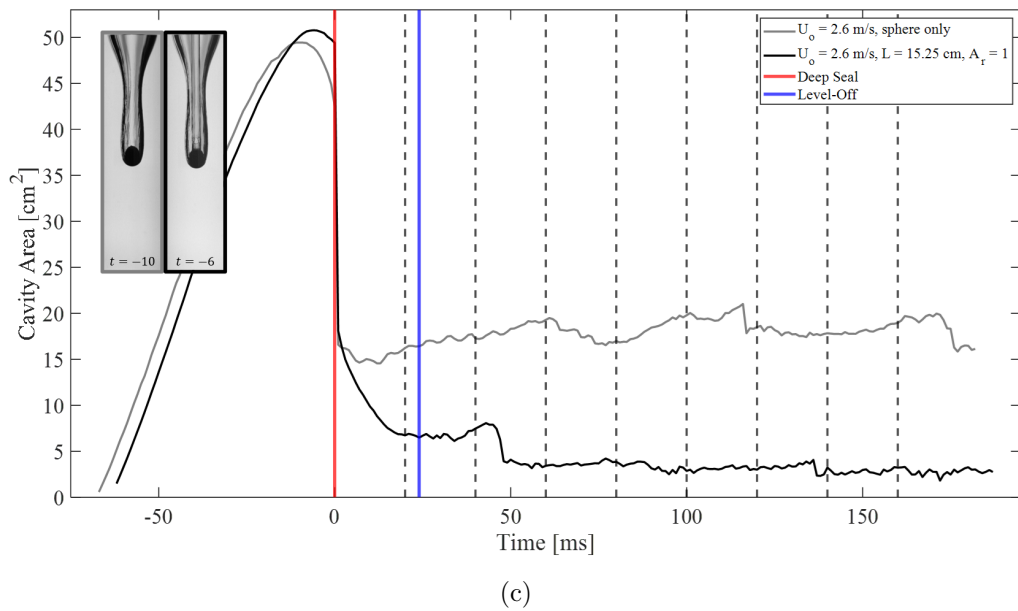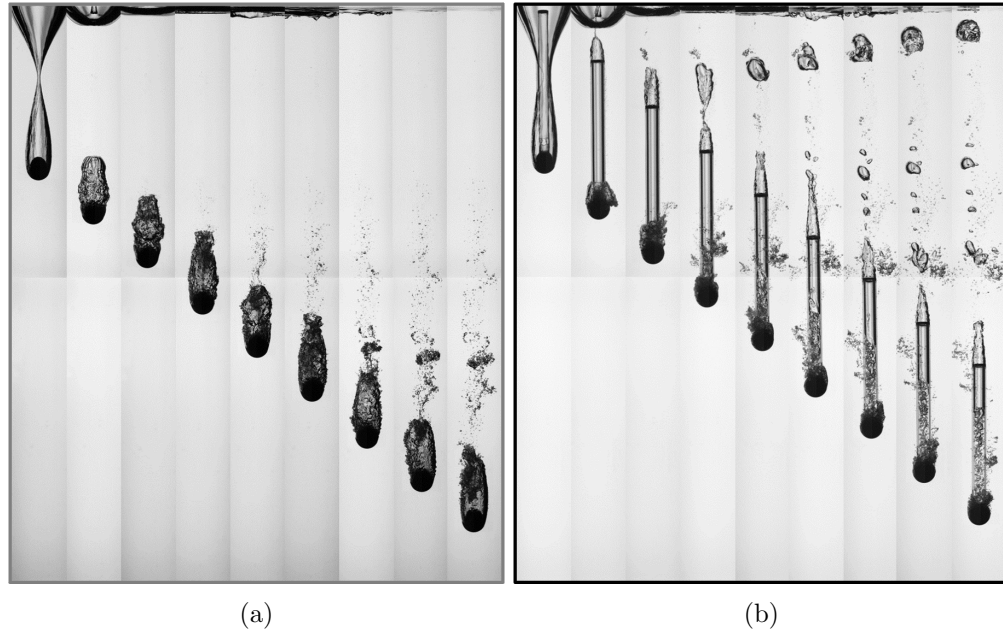
Fig. 3.2: Image sequences of (a) sphere only case and (b) vented tube case and corresponding (c) cavity area plot. For both cases the impact velocity is $U_o = 2.6$ m/s, the sphere diameter is $D = 2.54$ cm, and the contact angle is $\theta = 117°$. For the vented tube case the vented tube diameter is $d = 1.27$ cm, the vented tube length is $L = 15.24$ cm, and the area ratio is $A_r = 1$. For both image sequences the time starts at deep seal and the time between frames is $\Delta t = 20$ ms. The red and blue lines in the cavity area plot represent time of deep seal and time of deflation level-off, respectively. For the cavity area study, deep seal is at $t = 0$ so that deflation is easily compared. The vertical dashed lines correspond with frames $2 - 9$ of the image sequences in (a) and (b).

two case at deep seal. They are aligned so that the lower cavities of the vented tube case and sphere only case can be compared. The vertical dashed lines in the cavity area plot (Fig. 3.2(c)) correspond with frames $2 - 9$ of the image sequences (Fig. 3.2(a)-(b)). All of the cavity area plots presented in this thesis that have corresponding image sequences use vertical dashed lines to designate the frames of the image sequences.

Fig. 3.2(c) shows that before deep seal, the maximum cavity area for the vented tube case is slightly larger than the cavity area for the sphere only case. The images of both cavities when they are at their maximum cavity area, 117 ms after impact for both cases, are inset in Fig. 3.2(c)). The inset images show that the cavity depth (measured from the free surface to the center of the sphere) at the time of maximum cavity area is slightly greater for the vented tube case and therefore, the vented tube case cavity has entrained more air than the sphere only case cavity. The actual impact velocity for both cases is calculated using the first few frames before impact and the difference in impact velocity is less than 0.01 m/s which indicates that trajectory for the vented tube case is altered below the free surface by the presence of the vented tube. Comparison of the first frame of the image sequences (Fig. 3.2(a)-(b)) shows that at deep seal the two cavities are similar in size but that the cavity for the vented tube case is slightly larger due to the additional area of the vented tube. These same observations are present in the cavity area plot (Fig. 3.2(c)). The cavity area for the vented tube case at deep seal is about 7 cm^2 larger than the cavity area of the sphere only case at deep seal. Immediately after deep seal the cavity area drops dramatically which is due to what area is tracked. As highlighted in Section 3.1.1, for deep seal and the frames before deep seal, the entire cavity is tracked (Fig. 3.1(a)-(b)) while after deep seal only the lower cavity is being tracked (Fig. 3.1(c)-(g)).

In the second frame of the image sequences (Fig. 3.2(a)-(b)) it is observed that 20 ms after deep seal, the cavity for the vented tube case is already dramatically smaller than the traditional cavity in the sphere only case. The dramatic change in cavity area after deep seal for the vented tube case is due to cavity deflation facilitated by the vent holes in the vented tube and is seen in Fig. 3.2(c). Between deep seal and 20 ms the cavity for the vented

tube case decreases by almost two thirds while the cavity for the sphere only case remains relatively constant. At 20 ms the vented tube case cavity area is 40% of the sphere only case cavity area. Cavity deflation occurs between deep seal and the level-off point which is marked by the vertical blue line in Fig. 3.2(c). Level-off occurs when the distance between the top of the cavity and the top of the vent holes stops decreasing (found from separate plots) and the deflation levels-off. For this vented tube case, deflation level-off occurs at 24 ms, when the cavity reaches the vent holes, at which point deflation is no longer possible as water begins to fill the vented tube, trapping any remaining air.

The sphere only case image sequence (Fig. 3.2(a)) illustrates that there are ripples on the surface of the cavity after deep seal and that the ripples induce cavity shedding as previously studied by Grumstrup et al. [11], Mansoor, et al. [13], and Zhang, et al. [14]. Cavity shedding is seen in the cavity area plot (Fig. 3.2(c)) as the fluctuations in the sphere only cavity area. The cavity area increases slowly as the cavity prepares to shed and then decreases when the cavity sheds air bubbles. The volume of the cavity remains the same as the cavity prepares to shed but the since the shape of the cavity changes during this process it shows up as a small change in cavity area due to the planar view of the cavity. The volume does decrease when the cavity sheds bubbles. Despite the fluctuations due to cavity shedding, Fig. 3.2(c) and Fig. 3.2(a) show that as the sphere only case continues to descend, the cavity size remains relatively constant.

As the vented tube case continues to descend after level-off, Fig. 3.2(c) shows that the cavity area remains relatively constant for the next 10 ms before it begins to increase slightly. As with the sphere only case, the increase in cavity area for the vented tube case is due to cavity shedding. As the cavity area prepares to shed, the cavity area increases slightly due to the change in cavity shape as described in the previous paragraph and seen in frame 3 of Fig. 3.2(b). The vented tube case image sequence (Fig. 3.2(b)) and cavity area profile (Fig. 3.2(c)) show that between 30 and 40 ms a significant portion (40%) of the remaining cavity is shed. For the remaining time the cavity dissipates slowly by shedding small air bubbles. By the final frame of the image sequences (Fig. 3.2(a)-(b)), the cavity

for the vented tube case is dramatically reduced compared to the sphere only case. At the end of the time frame the cavity area for the sphere only case is virtually unchanged while the cavity area for the vented tube case is reduced to 15% of the original cavity.

3.1.3 Averaged Trials

While the cavity area example plot in Section 3.1.2 shows one trial for each case, for the actual cavity area data presented in the rest of this thesis five trials are conducted and averaged for each case. Fig. 3.3 and Fig. 3.5 present the image sequences of five trials conducted for the sphere only case and vented tube case described in Section 3.1.2, respectively. Fig. 3.4 and Fig. 3.6 present the corresponding cavity area plots. For Fig. 3.4 and Fig. 3.6, the cavity area of the five individual trials as well as the average cavity area of the five trials is plotted. Multiple trials are conducted for the sphere only case and averaged to ensure the results are consistent and to reduce fluctuations in the cavity area due to shedding, as seen in Fig. 3.4 and Fig. 3.6, that result from only using one angle of the cavity in the cavity area calculations.

As described in Section 3.1.2 for both the sphere only and vented tube cases, as cavities prepare to shed, the cavity shape changes resulting in an altered cavity area due to the planer view. If multiple angles of the cavity were averaged in the cavity area calculations for each case, the estimated cavity area would account for the differences in the cavity shape at each angle. A large area variation in the cavity at one angle would be averaged out by a smaller area variation in the cavity at another angle. Multiple camera angles are infeasible for this thesis so the average cavity area of multiple trials is used instead. As seen in Fig. 3.3 and Fig. 3.5 for both the sphere only and vented tube cases there are variations in how the cavities shed between multiple trials for the same case. The average of the cavity area between multiple trials acts similarly to the average of the cavity area of multiple angles for one trial by averaging out the variations between trials seen in Fig. 3.3 and Fig. 3.5.

Five trials per case were selected based on standard error analysis. Ten trials were conducted for one vented tube case (U_o = 2.2 m/s, d = 1.27 cm, L = 15.24 cm, A_r = 0.5) and the average cavity area over time and error within a 95 percent confidence interval was

(a) Trial 1　　　　　　(b) Trial 2　　　　　　(c) Trial 3

(d) Trial 4　　　　　　(e) Trial 5
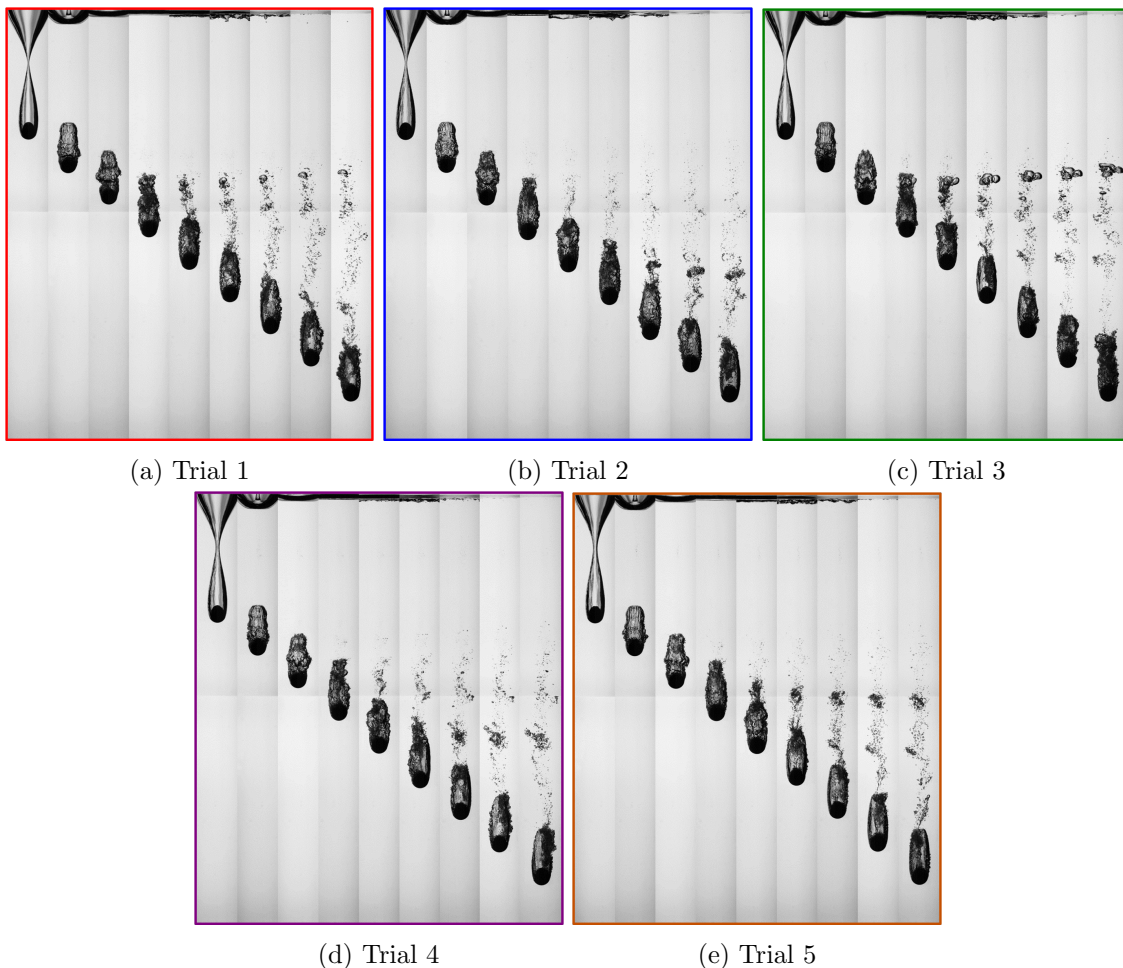
Fig. 3.3: Image sequences for five trials for a single sphere only case. For all of the trials the impact velocity is $U_o = 2.6$ m/s, the sphere diameter is $D = 2.54$ cm, and the contact angle is $\theta = 117°$. For all five image sequences the time starts at deep seal and the time between frames is $\Delta t = 20$ ms.

calculated for three, four, five, seven, and ten trials. The results are plotted in Fig. 3.7. For ten and seven averaged trials the error is very similar. For five averaged trials the error starts to deviate slightly. For four and three averaged trials the deviation in the error increases. Based on these results, five trials were selected as that is the minimum number of trials before the error started to increase drastically. For the remainder of this thesis all of the cavity area calculations shown in the plots are averages of five trials per case.
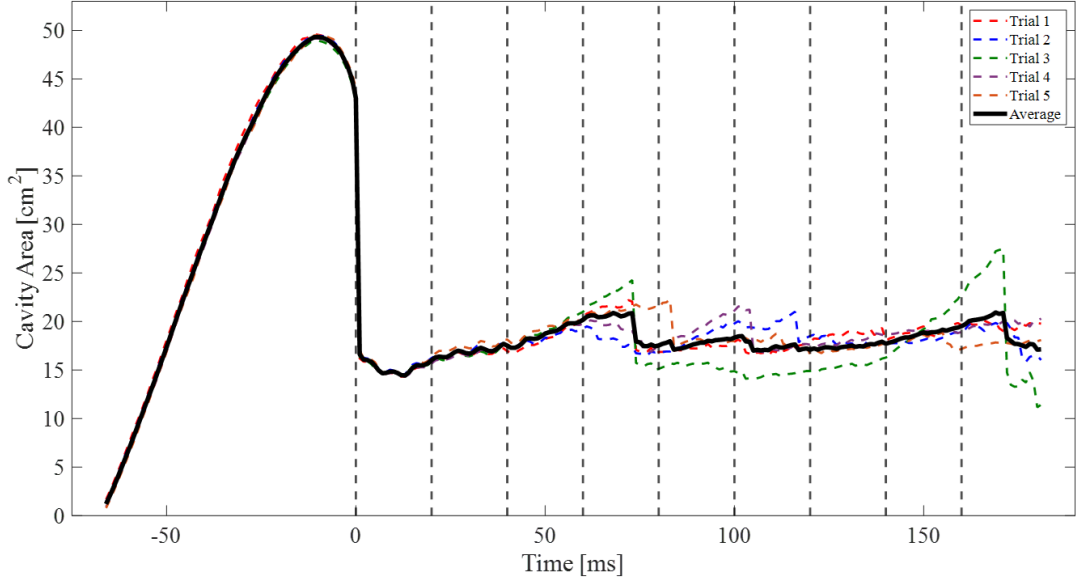
Fig. 3.4: Cavity area plot of five trials for a single sphere only case and the averaged cavity area. For all of the trials the impact velocity is $U_o = 2.2$ m/s, the sphere diameter is $D = 2.54$ cm, and the contact angle is $\theta = 117°$. The vertical dashed lines correspond with each frame of the image sequences in Fig. 3.3.

3.1.4 Cavity Area Selection

As discussed in Section 3.1.1, cavity area vs time is estimated from the high-speed camera images which provide a planar view of the cavity. This estimation is based on two assumptions. First, as the cavity forms and during deflation, the cavity has an axis of symmetry (Fig. 3.1(a)-(c)), and the planar cavity area is representative of the cavity volume by a factor of 2π. Second, the increase in uncertainty observed in Fig. 3.7 occurs when the cavity prepares to shed, at which point the cavity no longer has an axis of symmetry (Fig. 3.1(d)-(g)), and the planar cavity area is no longer representative of the cavity volume. Despite an increase in uncertainty in the cavity area estimate as the cavity prepares to shed, the planar cavity area provides a valid means to quantify cavity deflation from a planar view of the cavity across the entire time frame, while cavity volume is only represented by the planar cavity area for part of the time the cavity is tracked.

(a) Trial 1   (b) Trial 2   (c) Trial 3

(d) Trial 4   (e) Trial 5
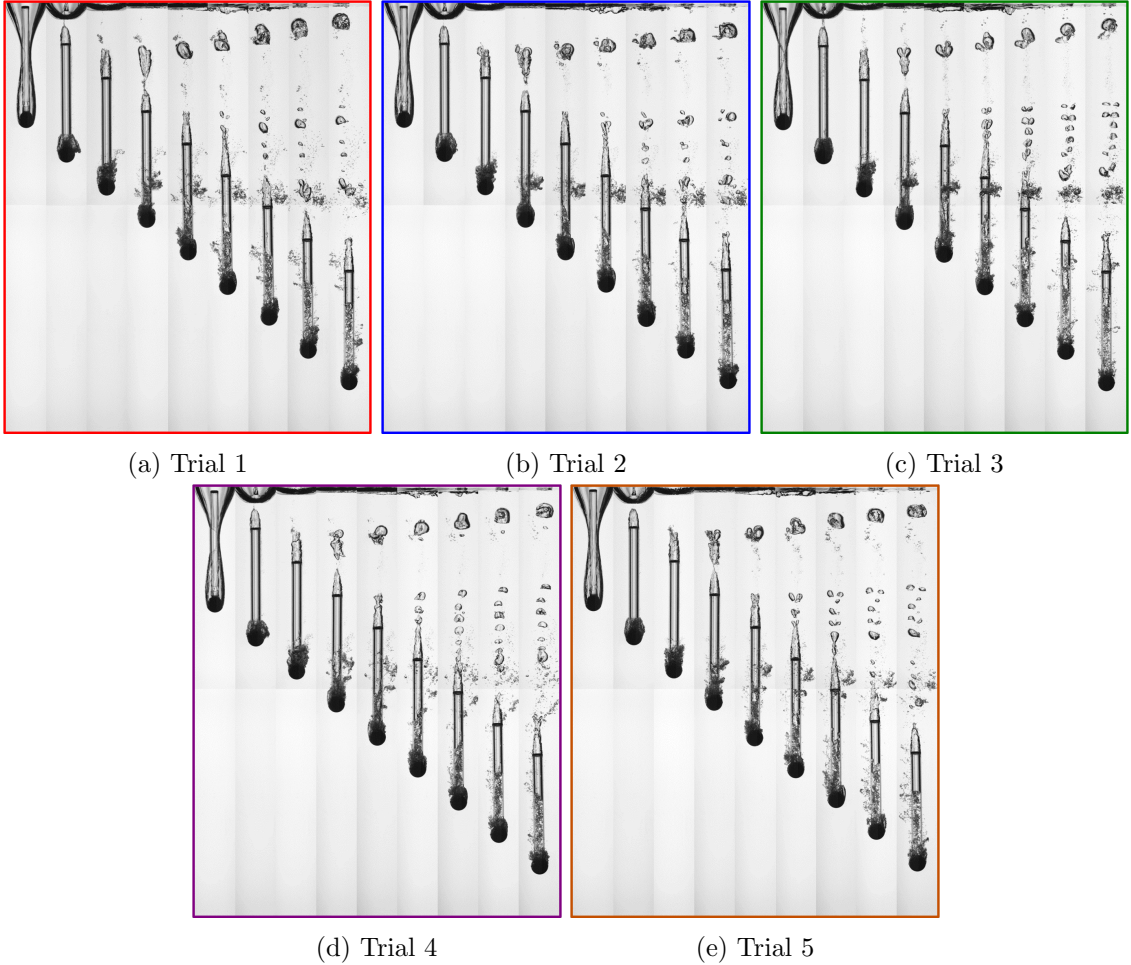
Fig. 3.5: Image sequence of five trials for a single vented tube case. For all of the trials the impact velocity is $U_o = 2.6$ m/s, the sphere diameter is $D = 2.54$ cm, the contact angle is $\theta = 117°$, the vented tube diameter is $d = 1.27$ cm, the vented tube length is $L = 15.24$ cm, and the area ratio is $A_r = 1$. For all five image sequences the time starts at deep seal and the time between frames is $\Delta t = 20$ ms.

3.2 Results and Discussion

This section presents the results of the cavity area study. For this introductory study of cavity deflation, three main parameters are varied to determine how they affect the amount of cavity deflation for deep seal cases: vented tube length, area ratio, and impact velocity. The following results present image sequences and cavity area plots comparing different cases, first looking at the parameters individually and then comparing the combined effects of two parameters. How vented tube diameter and surface seal affect cavity deflation are
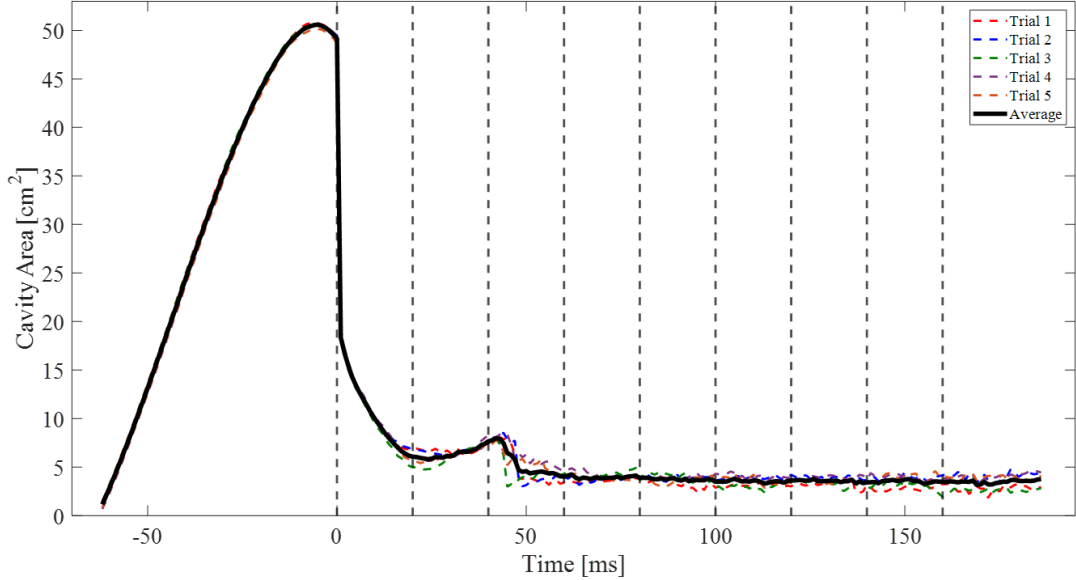
Fig. 3.6: Cavity area plot of five trials for a single vented tube case and the averaged cavity area. For all of the trials the impact velocity is $U_o = 2.6$ m/s, the sphere diameter is $D = 2.54$ cm, the contact angle is $\theta = 117°$, the vented tube diameter is $d = 1.27$ cm, the vented tube length is $L = 15.24$ cm, and the area ratio is $A_r = 1$. The vertical dashed lines correspond with each frame of the image sequences in Fig. 3.5.

also briefly discussed. Finally, this section concludes with a theoretical model for the critical vented tube length needed for cavity deflation to occur as a function of sphere radius, impact velocity, and vented tube diameter.

The following important features discussed in Section 3.1 are relevant to the image sequences and cavity area plots presented in this section. For each case presented, the cavity area is an average of five trials. For a given impact velocity, the presence of a vented tube appears to slightly alter the cavity trajectory and therefore slightly alter how much air is entrained before deep seal. The cavity area is aligned so that deep seal occurs at $t = 0$. Deep seal occurs more abruptly for cases with vented tube pinch-off compared to cases with natural pinch-off due to early pinch-off. The cavity area at deep seal is larger for vented tube cases compared to sphere only cases due to the additional area of the vented tube. Only the lower cavity is tracked after deep seal for both the sphere only and vented tube cases. Sphere only cases never experience deflation. For vented tube cases, if the cavity
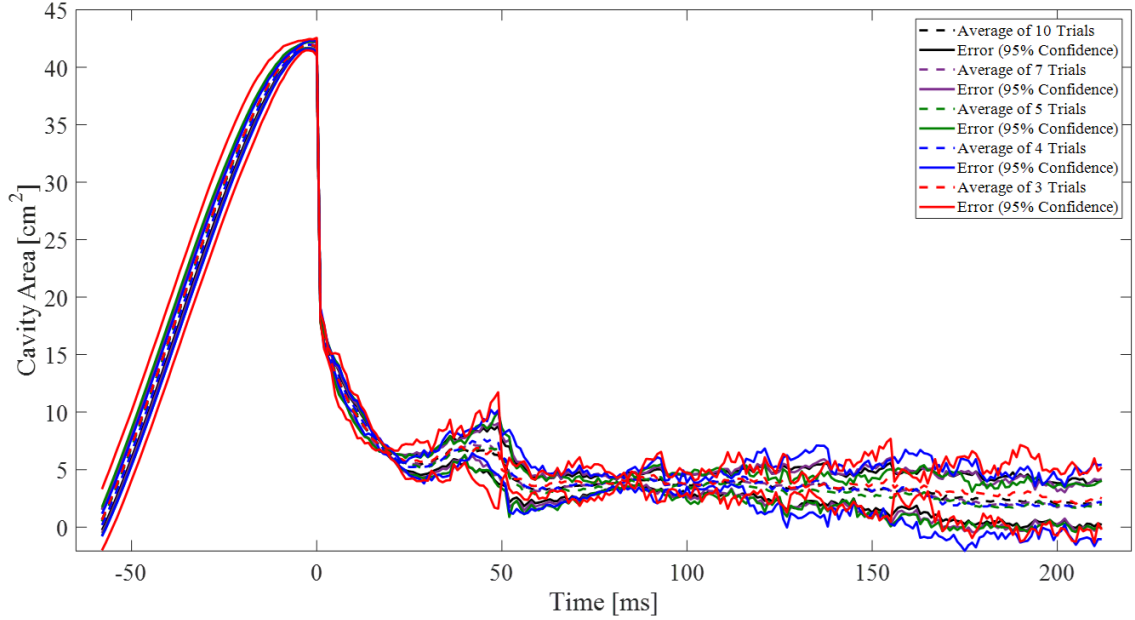
Fig. 3.7: Average cavity area and corresponding error within a 95% confidence interval for 10, 7, 5, 4, and 3 trials. For all of the trials the impact velocity is $U_o = 2.2$ m/s, the sphere diameter is $D = 2.54$ cm, the contact angle is $\theta = 117°$, the vented tube diameter is $d = 1.27$ cm, the vented tube length is $L = 15.24$ cm, and the area ratio is $A_r = 0.5$.

reaches the vent holes, deflation is no longer possible as water begins to fill the vented tube, trapping any remaining air. The uncertainty in the cavity area estimate increases when the cavity first prepares to shed and the cavity area starts to level out. For cavity area plots with corresponding image sequences, the vertical dashed lines in the plot designate the frames of the image sequences and the image sequences are outlined in the line color and style of the corresponding cases in the plot.

Two additional plots are presented in the cavity area results for each cavity area plot. The first is the total change in cavity area at each time step of deflation, from the first frame after deep seal to the level-off time. The second is the ratio of the remaining cavity at each time step of deflation to the initial lower cavity, which is the lower cavity immediately after deep seal (the next frame). Only cases that experience deflation are included in these two plots and the goal is to highlight the time and amount of cavity deflation which can be difficult to extract from the big picture cavity area plots.

3.2.1 Vented Tube Length

The first set of results looks at how vented tube length affects cavity deflation. A sphere only case and four vented tube length cases ($L = 3.81$ cm, $L = 7.62$ cm, $L = 11.43$ cm, $L = 15.24$ cm) are compared in the image sequences in Fig. 3.8 and the cavity area and deflation plots in Fig. 3.9. For all cases the impact velocity is $U_o = 2.6$ m/s and for all vented tube cases the vented tube diameter is $d = 1.27$ cm and the area ratio is $A_r = 1$. The image sequences (Fig. 3.8(b)-(e)) and cavity area profiles (Fig. 3.9(a)) after deep seal for the four vented tube cases show that no deflation occurs for the $L = 3.81$ cm vented tube case and deflation does occur for the $L = 7.62$ cm, $L = 11.43$ cm, and $L = 15.24$ cm vented tube cases. As the vented tube length increases, the amount of deflation increases. For the $L = 3.81$ cm vented tube case (Fig. 3.8(b)), natural deep seal occurs and the vented tube is fully inside of the lower cavity at deep seal which provides no outlet for the air that enters the vented tube and the air remains trapped in the cavity. As the $L = 3.81$ cm vented tube case cavity descends it is similar to the sphere only case cavity (Fig. 3.8(a)) with minimal change in size except for the release of small bubbles due to shedding.

For the three longer vented tube lengths (Fig. 3.8(c)-(e)), deep seal occurs on the vented tube and the vented tube is outside of the lower cavity at deep seal which allows air that enters the vented tube to escape to free surface. The the depth of pinch-off is similar for all cases, so the location of vented tube deep seal varies based on the vented tube length. For the $L = 7.62$ cm vented tube case (Fig. 3.8(c)) deep seal occurs at the top of the vented tube, for the $L = 11.43$ cm vented tube case (Fig. 3.8(d)) a few centimeters below the top of the vented tube, and for the 15.24 cm vented tube case (Fig. 3.8(e)) near the midpoint of the vented tube. Where deep seal occurs on the vented tube, and therefore the vented tube length, determines how long the vented tube is in the upper cavity between deep seal and when the upper cavity seals, which impacts how much air can escape to the free surface. The upper cavity seal time is marked with 'o' in the deflation plots (Fig. 3.9(b)-(c)) for the three deflating vented tube cases and it is observed that most of the deflation occurs before the upper cavity seals and that the later the upper cavity seals, the more deflation occurs.
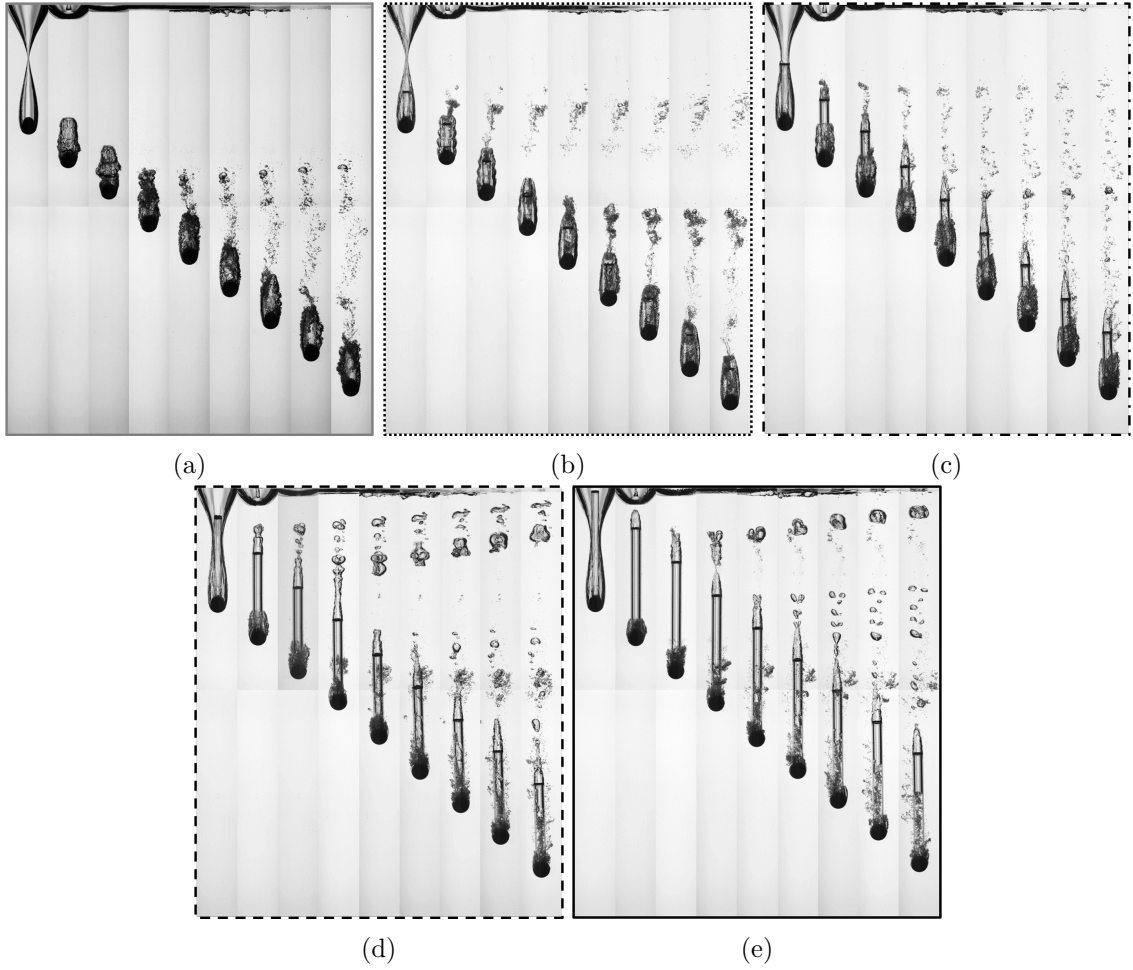
Fig. 3.8: Image sequences comparing (a) sphere only case and four vented tube length cases: (b) $L = 3.81$ cm, (c) $L = 7.62$ cm, (d) $L = 11.43$ cm, and (e) $L = 15.24$ cm. For all cases the impact velocity is $U_o = 2.6$ m/s, the sphere diameter is $D = 2.54$ cm, and the contact angle is $\theta = 117°$. For all vented tube cases the vented tube diameter is $d = 1.27$ cm and the area ratio is $A_r = 1$. For all five image sequences the time starts at deep seal and the time between frames is $\Delta t = 20$ ms.

Deflation can still occur after upper cavity seal, as seen in (Fig. 3.9(b)-(c)), as air is released in the form of the air bubble at the top of the vented tube, but the rate of deflation slows significantly as the air in the cavity has to wait for the release of the air bubble. For the $L = 15.24$ cm vented tube case, the cavity has almost deflated by the time upper cavity seal occurs and so only needs to deflate a short time more before the cavity reaches the vent holes and no more deflation is possible. For the $L = 11.43$ cm vented tube case, the cavity
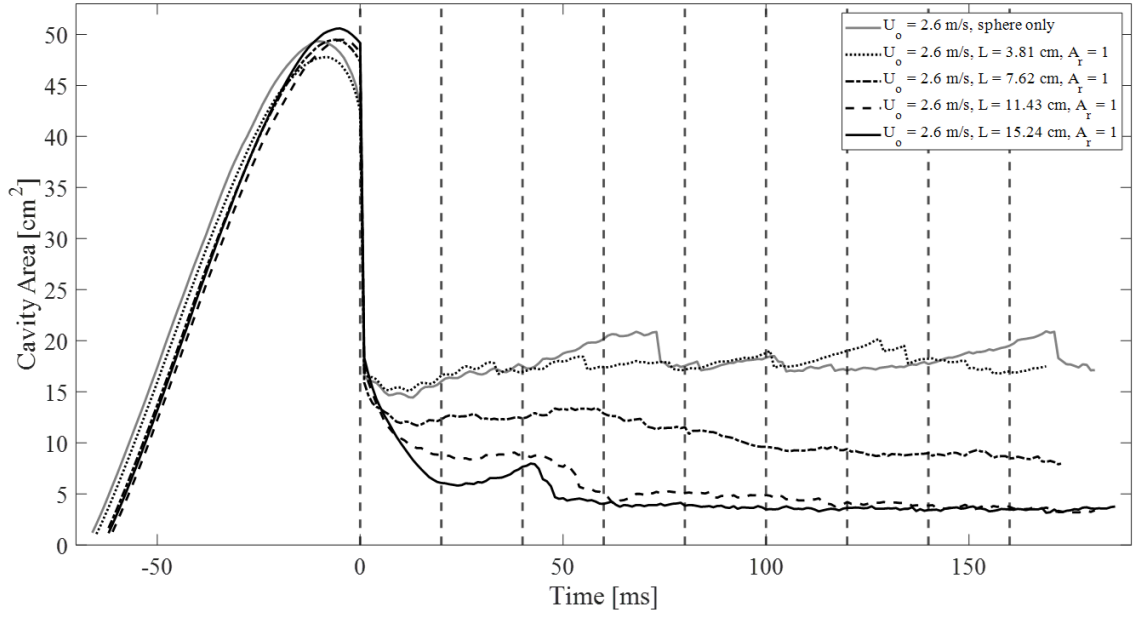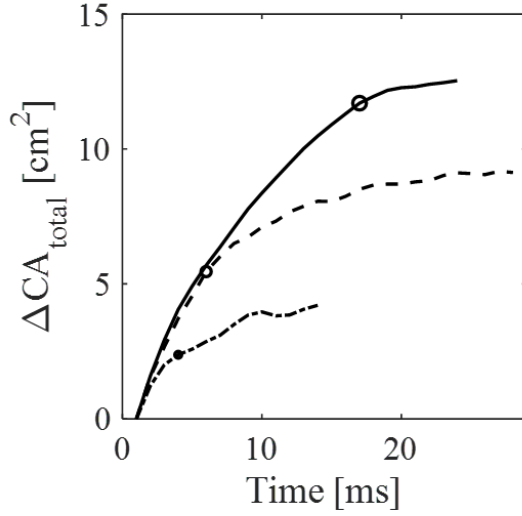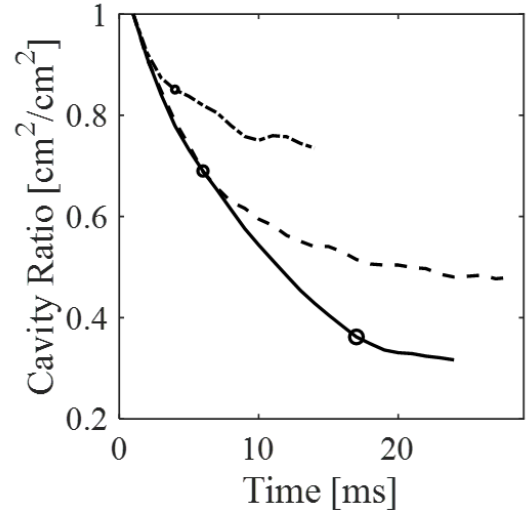
Fig. 3.9: (a) Cavity area plot comparing sphere only case and four vented tube length cases: $L = 3.81$ cm, $L = 7.62$ cm, $L = 11.43$ cm, and $L = 15.24$ cm. (b) Total change in cavity area as function of time and (c) ratio of remaining cavity to initial lower cavity as a function of time over the deflation period for the three vented tube cases that deflate. The upper cavity seal time is marked in (b) and (c) by 'o'. For all cases the impact velocity is $U_o = 2.6$ m/s, the sphere diameter is $D = 2.54$ cm, and the contact angle is $\theta = 117°$. For all vented tube cases the vented tube diameter is $d = 1.27$ cm and the area ratio is $A_r = 1$. The vertical dashed lines correspond with each frame of the image sequences in Fig. 3.8.

continues to deflate until it begins to shed. It is possible slow deflation still occurs at this point, but it is overpowered in the cavity area calculations by the change in cavity area due to shedding. For the $L = 7.62$ cm vented tube case, the cavity deflation ends abruptly with a significant portion of the cavity remaining when cavity ripples are observed which appear to suppress further deflation.

3.2.2 Area Ratio

The second set of results looks at how area ratio affects cavity deflation. A sphere only case and seven area ratio cases ($A_r = 0.1$, $A_r = 0.3$, $A_r = 0.5$, $A_r = 1$, $A_r = 2$, $A_r = 4$, $A_r = 10$) are compared in the image sequences in Fig. 3.10 and the cavity area and deflation plots in Fig. 3.11 and Fig. 3.12. For all cases the impact velocity is $U_o = 2.6$ m/s and for all vented tube cases the vented tube diameter is $d = 1.27$ cm and the vented tube length is $L = 15.24$ cm. Fig. 3.11 first compares the cavity area for area ratio cases $A_r = 0.1$-$A_r = 2$ which have one row of radial vent holes. For the five area ratio cases, the second frame of the image sequences (Fig. 3.10(b)-(f)) and the cavity area profiles (Fig. 3.11(a)) after deep seal show all five cavities deflate, the amount of deflation increases as the area ratio increases, and the impact of a larger area ratio weakens as the area ratio increases.

As the vented tube length is the same for all five area ratio cases, the upper cavity seal time is the same for all five cases (Fig. 3.11(b)-(c)) which means that for all five cases the air has the same amount of time to escape to the free surface. The difference in deflation for the area ratio cases is determined by the vent hole area. The area of the vent holes impacts how much air can enter the vented tube at a given time. As the area ratio increases, the vent hole area increases, which allows more air to enter the vented tube while air can escape to the free surface compared to smaller area ratios, as observed in the cavity deflation rates before upper cavity seal (Fig. 3.11(b)-(c)). After upper cavity seal all five area ratio cases continue to deflate until the cavity reaches the vent holes ($A_r = 1$, $A_r = 2$) or the cavity begins to shed ($A_r = 0.1$, $A_r = 0.3$, $A_r = 0.5$). For a single row of radial holes, there is a limit to the impact of increased vent hole area. The limit occurs when the vent hole area is large enough that enough air can escape for the cavity to reach the vent holes. Based on
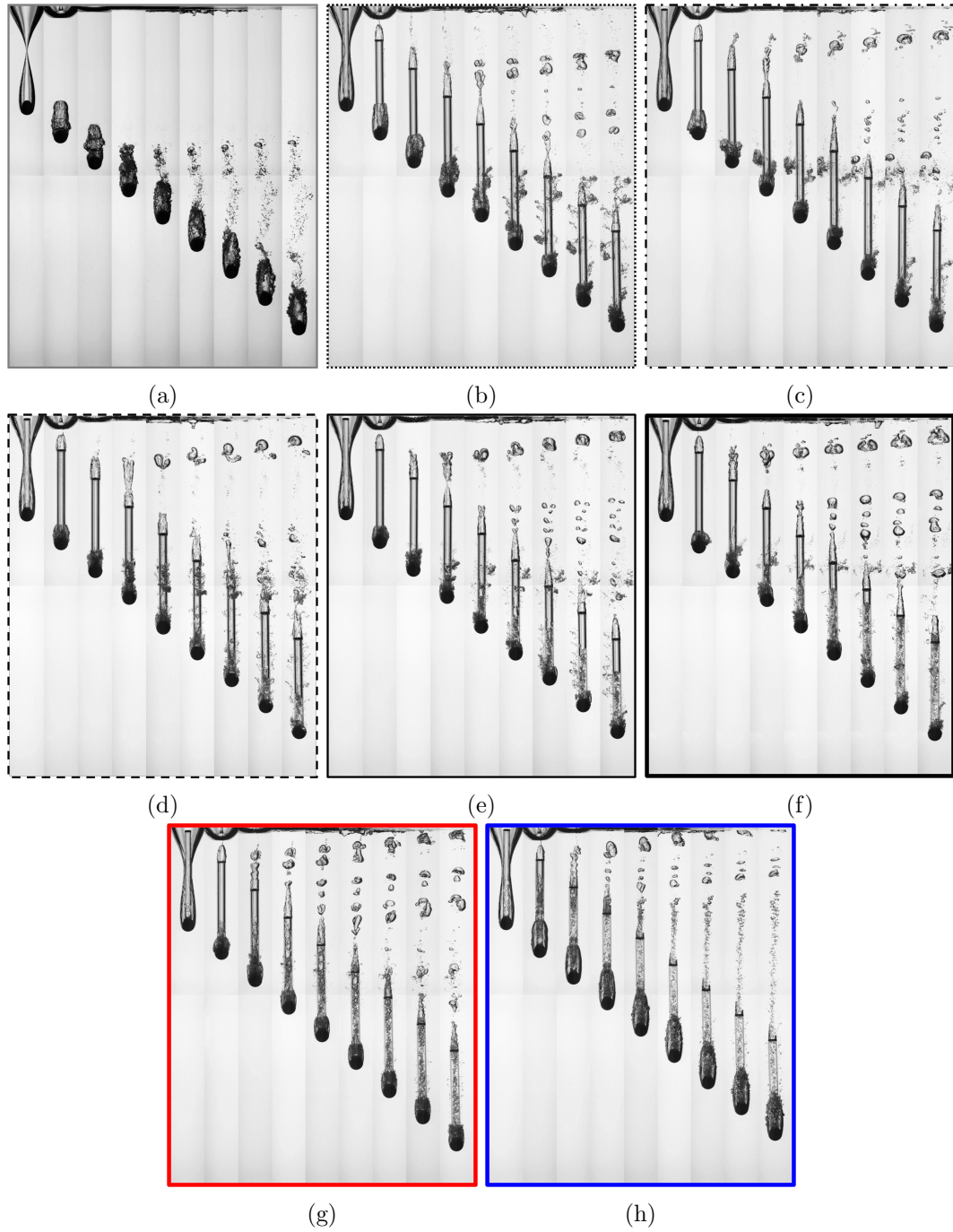
Fig. 3.10: Image sequences comparing (a) sphere only case and seven area ratio cases: (b) $A_r = 0.1$, (c) $A_r = 0.3$, (d) $A_r = 0.5$, (e) $A_r = 1$, (f) $A_r = 2$, (g) $A_r = 4$, and (h) $A_r = 10$. For all cases the impact velocity is $U_o = 2.6$ m/s, the sphere diameter is $D = 2.54$ cm, and the contact angle is $\theta = 117°$. For all vented tube cases the vented tube diameter is $d = 1.27$ cm and the vented tube length is $L = 15.24$ cm. For all eight image sequences the time starts at deep seal and the time between frames is $\Delta t = 20$ ms.
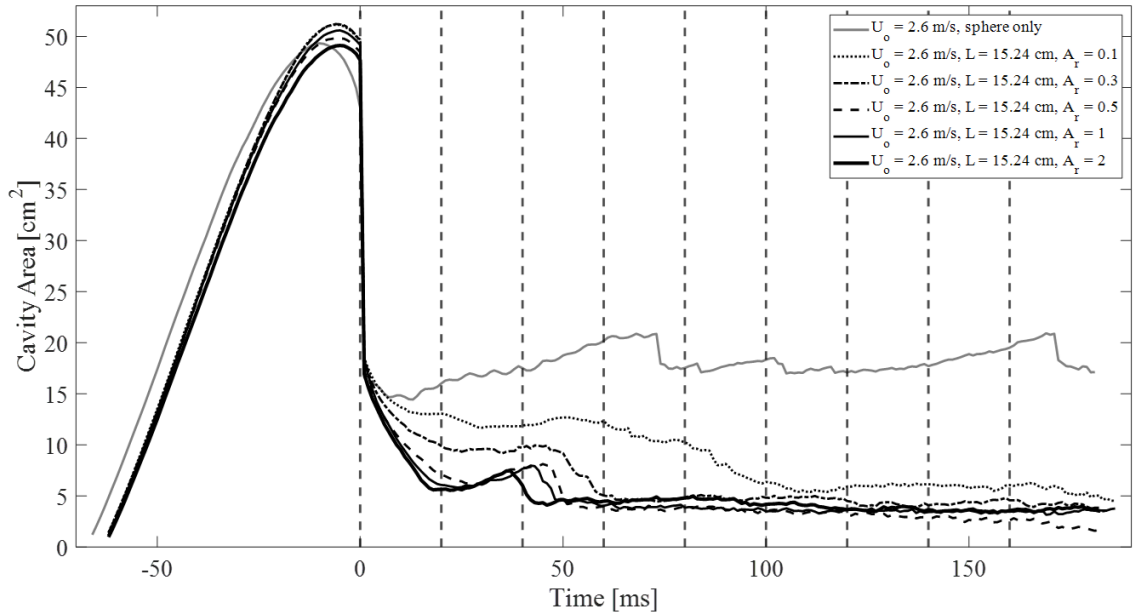
(a)
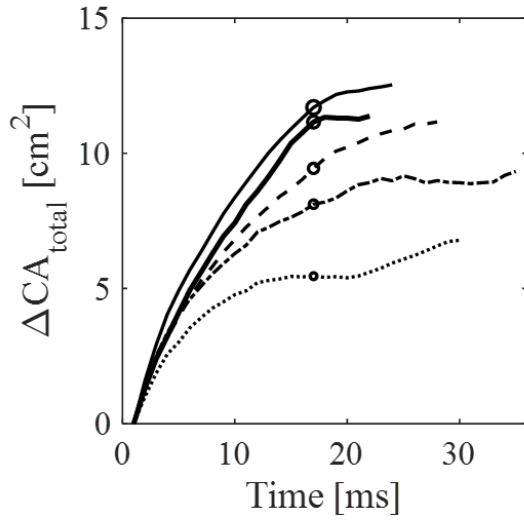
(b)
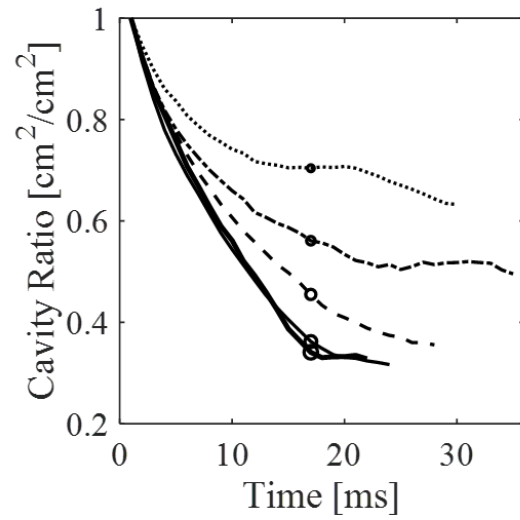
(c)

Fig. 3.11: (a) Cavity area plot comparing sphere only case and five area ratio cases: $A_r =$ 0.1, $A_r = 0.3$, $A_r = 0.5$, $A_r = 1$, and $A_r = 2$. (b) Total change in cavity area as function of time and (c) ratio of remaining cavity to initial lower cavity as a function of time over the deflation period for the five vented tube cases that deflate. The upper cavity seal time is marked in (b) and (c) by 'o'. For all cases the impact velocity is $U_o = 2.6$ m/s, the sphere diameter is $D = 2.54$ cm, and the contact angle is $\theta = 117°$. For all vented tube cases the vented tube diameter is $d = 1.27$ cm and the vented tube length is $L = 15.24$ cm. The vertical dashed lines correspond with each frame of the image sequences in Fig. 3.10.
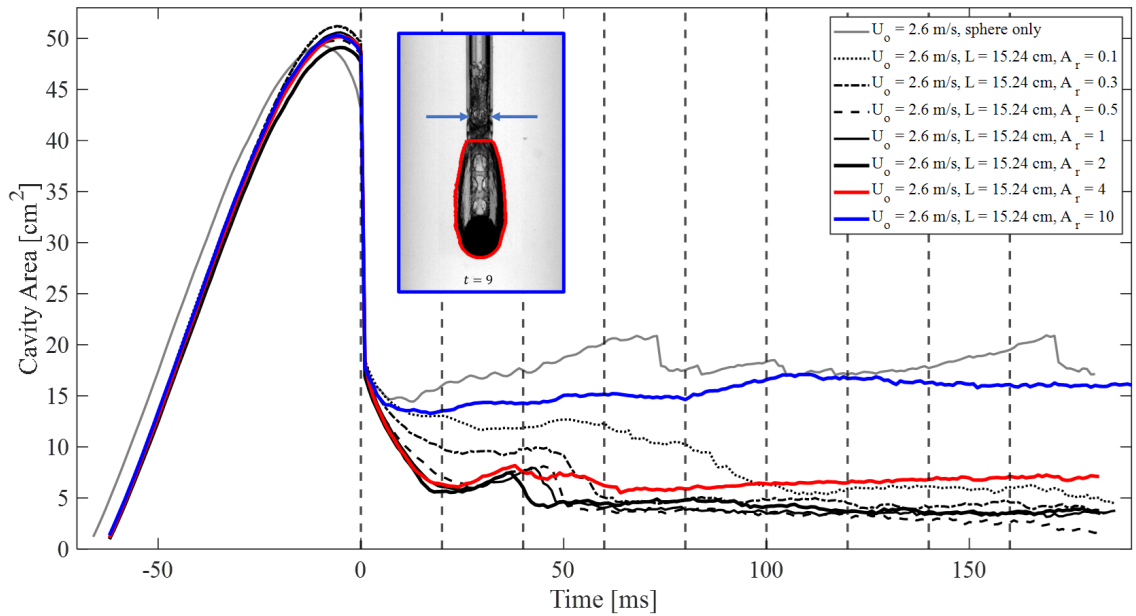
(a)
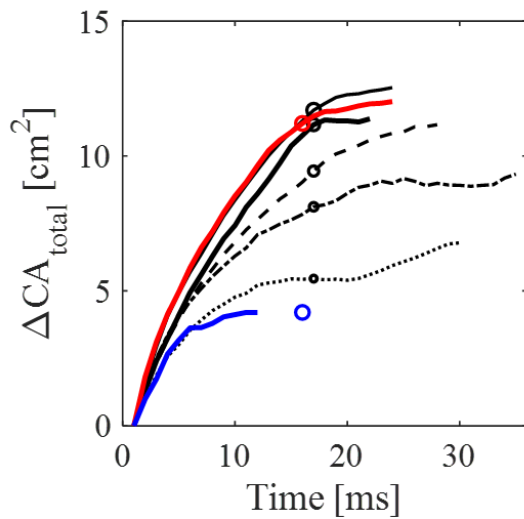
(b)
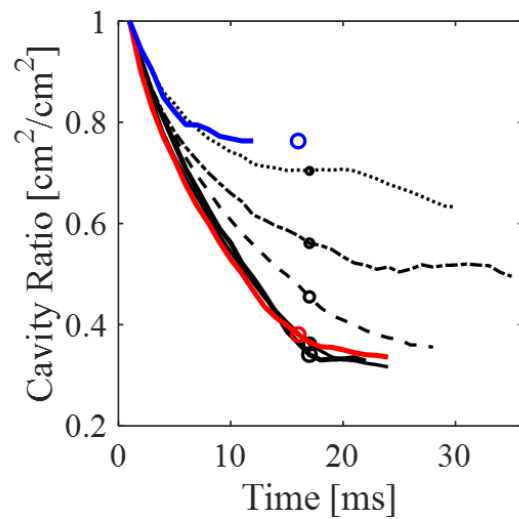
(c)

Fig. 3.12: (a) Cavity area plot comparing area ratio cases in Fig. 3.11 with the addition of $A_r = 4$ and $A_r = 10$ cases. Inset image in (a) of the $A_r = 10$ vented tube case cavity at 12 ms. (b) Total change in cavity area as function of time and (c) ratio of remaining cavity to initial lower cavity as a function of time over the deflation period for the seven vented tube cases that deflate. The upper cavity seal time is marked in (b) and (c) by 'o'. For all cases the impact velocity is $U_o = 2.6$ m/s, the sphere diameter is $D = 2.54$ cm, and the contact angle is $\theta = 117°$. For all vented tube cases the vented tube diameter is $d = 1.27$ cm and the vented tube length is $L = 15.24$ cm. The vertical dashed lines correspond with each frame of the image sequences in Fig. 3.10.

the results the limit appears to be between $A_r = 0.5$ and $A_r = 1$ for the 1.27 cm vented tube diameter. To find the exact limit, a finer range of area ratios between $A_r = 0.5$ and $A_r = 1$ needs to be tested.

Fig. 3.12 compares the cavity area for the five area ratio cases discussed above with two additional area ratio cases: $A_r = 4$ (Fig. 3.10(g)) and $A_r = 10$ (Fig. 3.10(h)). For both additional area ratio cases, the vent hole area is the same as for the $A_r = 2$ vented tube cases but there are multiple rows of radial vent holes to determine if more air can escape with multiple exit points. Fig. 3.12 shows that deflation for the $A_r = 4$ vented tube case is similar to the $A_r = 1$ and $A_r = 2$ vented tube cases both in terms of the time and amount of deflation. The $A_r = 10$ vented tube case image sequence (Fig. 3.10(h)) and Fig. 3.12 show that deflation quickly levels off for the $A_r = 10$ vented tube case, before the upper cavity seals, and only a small amount of cavity deflation occurs. The reason larger area ratio cases with multiple rows of radial vent holes do not increase the amount of deflation is explained with the image of the $A_r = 10$ vented tube case at 12 ms inset in Fig. 3.12(a). By the time the cavity reaches the second set of holes at 12 ms, water has already filled the vented tube above the cavity through the first set of holes. The water traps the remaining air in the cavity, preventing further deflation. This phenomenon explains why the amount of deflation for the $A_r = 2$ vented tube case is slightly less than for the $A_r = 1$ vented tube case (Fig. 3.12(b)-(c)). The vent holes for the $A_r = 2$ vented tube case are larger than the vent holes for the $A_r = 1$ vented tube case so the cavity reaches the vent holes faster for the $A_r = 2$ vented tube case and more of the cavity is trapped compared to the $A_r = 1$ vented tube case.

3.2.3 Vented Tube Length and Area Ratio

All five area ratios with a single row of vent holes ($A_r = 0.1$, $A_r = 0.3$, $A_r = 0.5$, $A_r = 1$, $A_r = 2$) for all four vented tube lengths ($L = 3.81$ cm, $L = 7.62$ cm, $L = 11.43$ cm, $L = 15.24$ cm) are compared in the cavity area and deflation plots in Fig. 3.13. For all cases the impact velocity is $U_o = 2.6$ m/s and for all vented tube cases the vented tube diameter is $d = 1.27$ cm. Fig. 3.13 highlights the combined effects of vented tube length
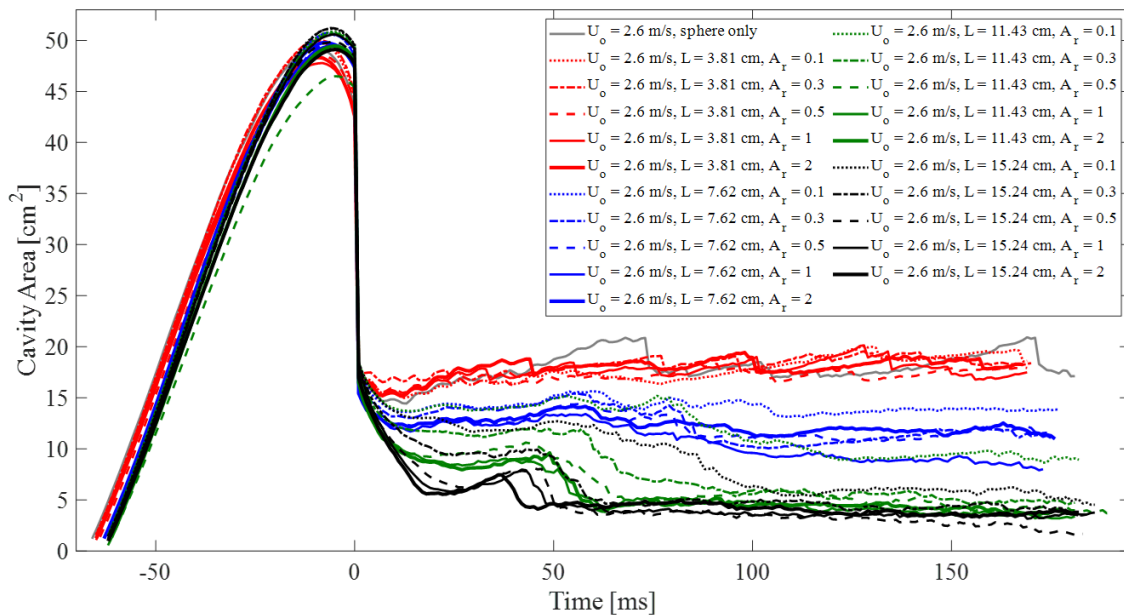
(a)
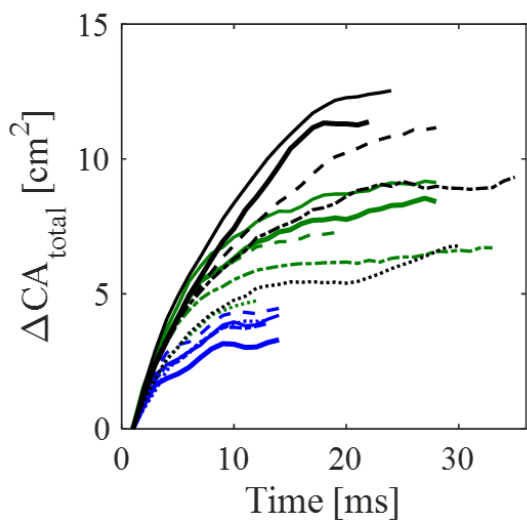
(b)
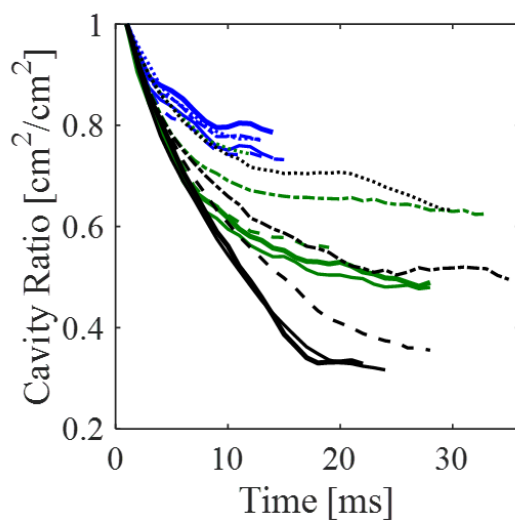
(c)

Fig. 3.13: (a) Cavity area plot comparing different vented tube lengths and area ratios for a single impact velocity: $U_o = 2.6$ m/s. (b) Total change in cavity area as function of time and (c) ratio of remaining cavity to initial lower cavity as a function of time over the deflation period for the vented tube cases that deflate. For all cases the sphere diameter is $D = 2.54$ cm, the contact angle is $\theta = 117°$, and the vented tube diameter is $d = 1.27$ cm.

and area ratio on cavity deflation. First, none of the $L = 3.81$ cm vented tube cases deflate which is expected as for all five area ratios the vented tube is fully within the cavity. Second, for all five area ratios the amount of deflation increases as the vented tube length increases. Third, as the vented tube length increases the amount of deflation between the area ratios increases, with the $L = 15.24$ cm vented tube case having the largest difference in deflation between the $A_r = 0.1$ and $A_r = 2$ area ratio cases. Fourth, for the $L = 7.62$ cm vented tube cases the time and amount of deflation is similar for all five area ratios with deflation ending abruptly when cavity ripples begin to form. Fifth, for the $L = 11.43$ cm and $L = 15.24$ cm vented tube cases the cavities deflate until they reach the vent holes ($L = 11.43$ cm, $A_r = 1$; $L = 15.24$ cm, $A_r = 2$) or begin to shed (all other cases).

3.2.4 Impact Velocity

The next set of results looks at how impact velocity affects cavity deflation. A sphere only case and vented tube case for three impact velocities ($U_o = 3.0$ m/s, $U_o = 2.6$ m/s, and $U_o = 2.6$ m/s) are compared in the image sequences in Fig. 3.14 and the cavity area and deflation plots in Fig. 3.15. For all vented tube cases the vented tube diameter is $d = 1.27$ cm, the vented tube length is $L = 15.24$ cm, and the area ratio is $A_r = 1$. For the three vented tube cases, both the second frame of the image sequences (Fig. 3.14(d)-(f)) and the cavity area profiles (Fig. 3.15(a)) after deep seal show all three cavities deflate and the size of the cavity remaining at the end of deep seal increases as impact velocity increases.

The first frame of the image sequences (Fig. 3.14) for the sphere only and vented tube cases show that as the impact velocity increases the cavity depth at deep seal increases and as the depth increases, more air is entrained in the cavity at deep seal. Both the cavity depth and cavity size at deep seal affect cavity deflation. The size of the cavity at deep seal impacts the size of the initial lower cavity and as the size of the initial lower cavity increases, the amount of air that needs to be deflated increases (as seen the second frame of the image sequences (Fig. 3.14(d)-(f)) and the cavity area profiles (Fig. 3.15(a)) after deep seal). The cavity depth at deep seal impacts the location of vented tube deep seal which, as discussed in Section 3.2.1, impacts how much air can escape to the free surface. As the
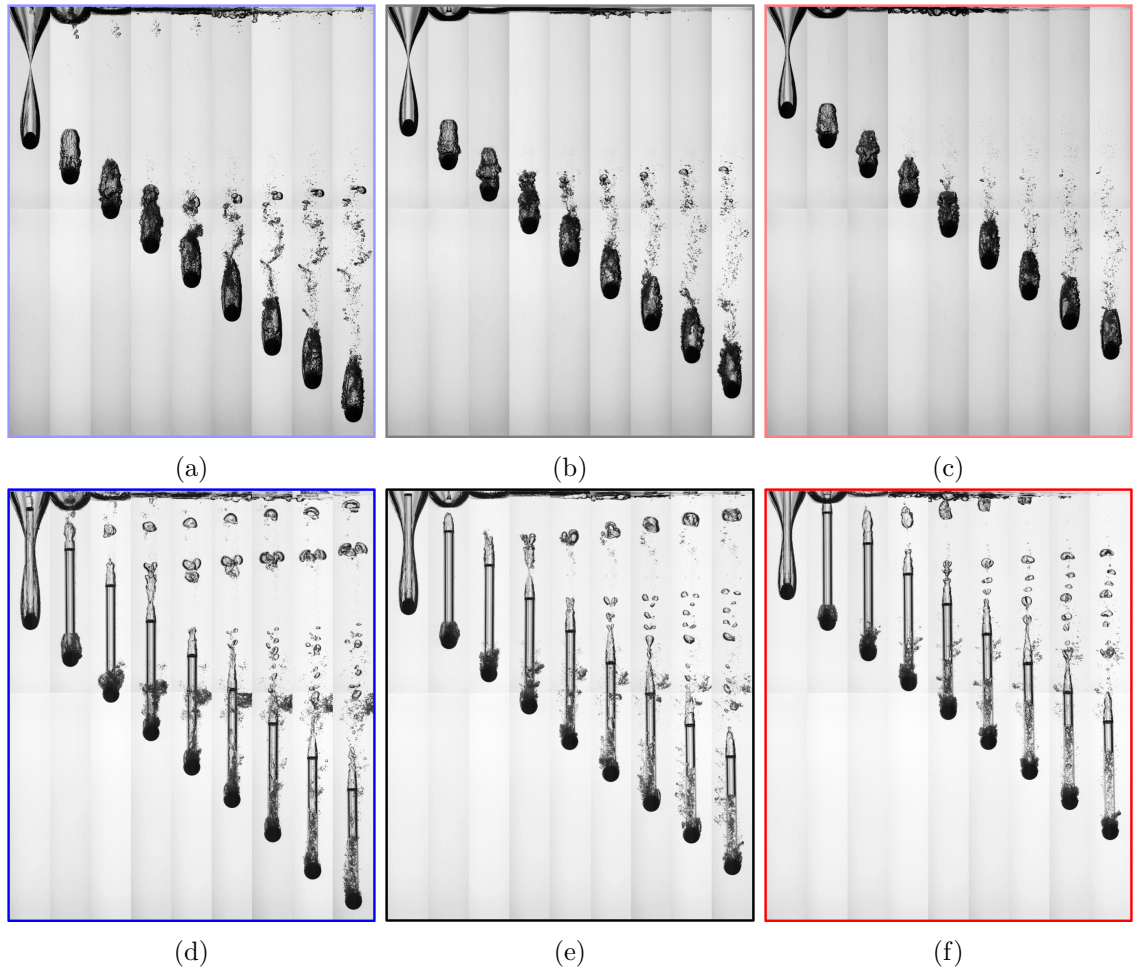
Fig. 3.14: Image sequences comparing the sphere only case and vented tube case for three impact velocities: $U_o = 3.0$ m/s, $U_o = 2.6$ m/s, and $U_o = 2.2$ m/s. (a) Sphere only, impact velocity $U_o = 3.0$. m/s. (b) sphere only, impact velocity $U_o = 2.6$ m/s. c) Sphere only, impact velocity $U_o = 2.2$ m/s. (d) Vented tube, impact velocity $U_o = 3.0$ m/s. (e) Vented tube, impact velocity $U_o = 2.6$ m/s. (f) Vented tube, impact velocity $U_o = 2.2$ m/s. For all cases the sphere diameter is $D = 2.54$ cm and the contact angle is $\theta = 117°$. For all vented tube cases the vented tube diameter is $d = 1.27$ cm, the vented tube length is $L = 15.24$ cm, and the area ratio is $A_r = 1$. For all six image sequences the time starts at deep seal and the time between frames is $\Delta t = 20$ ms.

cavity depth increases, vented tube deep seal occurs higher on the vented tube and the amount of time the vented tube is in the upper cavity decreases. The upper cavity seal times are marked in the deflation plots (Fig. 3.15(b)-(c)) and, as expected, the upper cavity seal times decrease as the impact velocity increases.
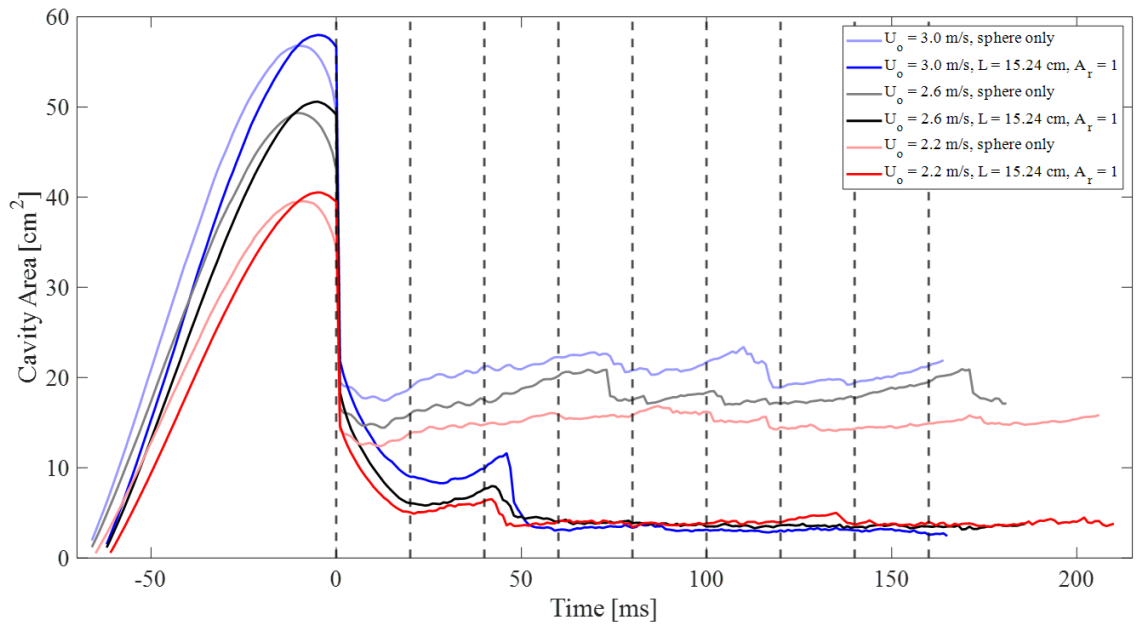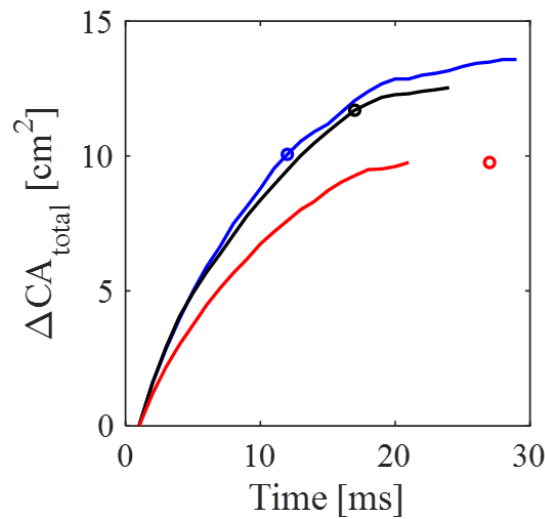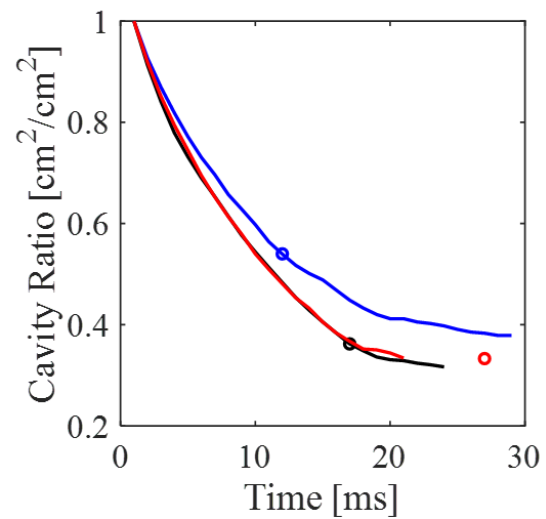
Fig. 3.15: (a) Cavity area plot comparing the sphere only case and vented tube case for three impact velocities: $U_o = 3.0$ m/s, $U_o = 2.6$ m/s, $U_o = 2.2$ m/s. (b) Total change in cavity area as function of time and (c) ratio of remaining cavity to initial lower cavity as a function of time over the deflation period for the seven vented tube cases that deflate. The upper cavity seal time is marked in (b) and (c) by 'o'. For all cases the sphere diameter is $D = 2.54$ cm and the contact angle is $\theta = 117°$. For all vented tube cases the vented tube diameter is $d = 1.27$ cm, the vented tube length is $L = 15.24$ cm, and the area ratio is $A_r = 1$. The vertical dashed lines correspond with each frame of the image sequences in Fig. 3.14.

Fig. 3.15(b)-(c) show that for the $U_o = 2.2$ m/s vented tube case, which has the smallest initial lower cavity, the cavity reaches the vent holes, at which point deflation is no longer possible, before the upper cavity seals. For the $U_o = 2.6$ m/s vented tube case the cavity has almost deflated by the time upper cavity seal occurs and continues to deflate after upper cavity seal until the cavity reaches the vent holes. For the $U_o = 3.0$ m/s vented tube case, which has the largest initial lower cavity, the cavity continues to deflate after the upper cavity seal until it begins to shed. The total change in cavity area is similar for the $U_o = 3.0$ m/s and $U_o = 2.6$ m/s vented tube cases and decreases for the $U_o = 2.2$ m/s vented tube case. Relative to the size of the initial lower cavity though, the amount of deflation is similar for $U_o = 2.6$ m/s and $U_o = 2.2$ m/s vented tube cases and both have a similar ratio of cavity remaining at the end of deflation. The $U_o = 3.0$ m/s vented tube case loses a similar amount of air as the $U_o = 2.6$ m/s vented tube case but the size of the initial lower cavity is larger, so the amount of deflation relative to the initial lower cavity is less. The $U_o = 3.0$ m/s vented tube case has a higher ratio of cavity remaining at the end of deflation compared to the other two vented tube cases.

3.2.5 Impact Velocity and Area Ratio

All five area ratios with a single row of vent holes ($A_r = 0.1$, $A_r = 0.3$, $A_r = 0.5$, $A_r = 1$, $A_r = 2$) for all three impact velocities ($U_o = 3.0$ m/s, $U_o = 2.6$ m/s, $U_o = 2.2$ m/s) are compared in the cavity area and deflation plots in Fig. 3.16. For all vented tube cases the vented tube diameter is $d = 1.27$ cm and the vented tube length is $L = 15.24$ cm. Fig. 3.16 highlights the combined effects of impact velocity and area ratio on cavity deflation. First, for all five area ratios the size of the initial lower cavity and the size of the cavity remaining at the end of deflation increase as impact velocity increases. Second, for all three impact velocities the amount deflation, both the total change in area and the ratio of the remaining cavity to the initial lower cavity, increases as the area ratio increases. Third, in general, for each area ratio the $U_o = 3.0$ m/s cases have the most deflation in terms of the total change in area, but relative to the initial lower cavity the cavities have deflated the least. Fourth, for all area ratios, except for the $A_r = 0.3$ vented tube cases, the
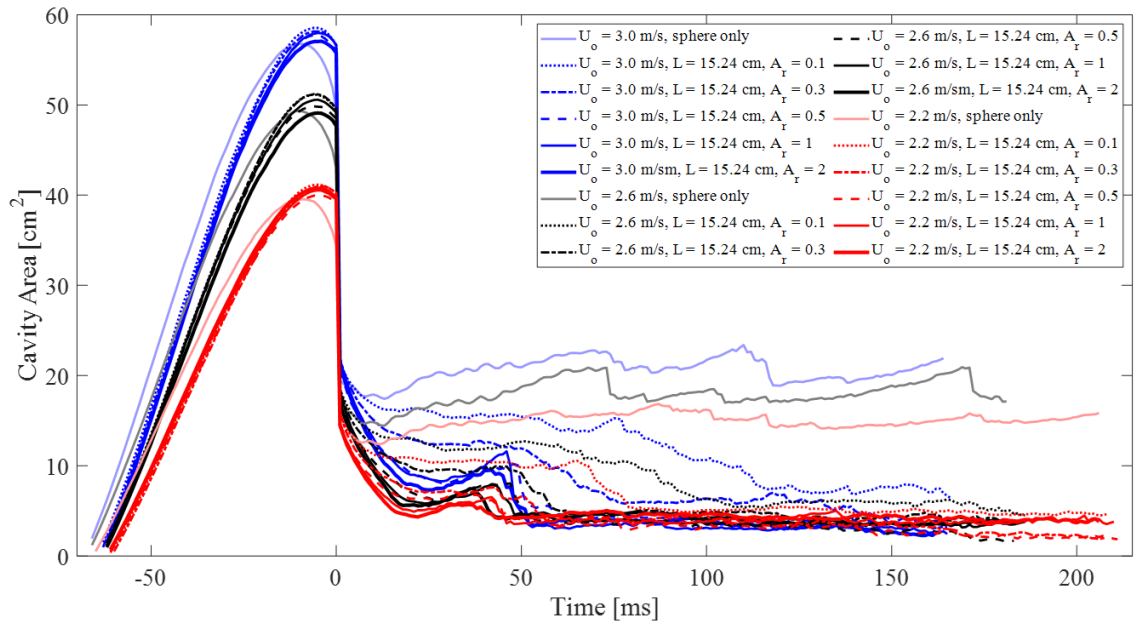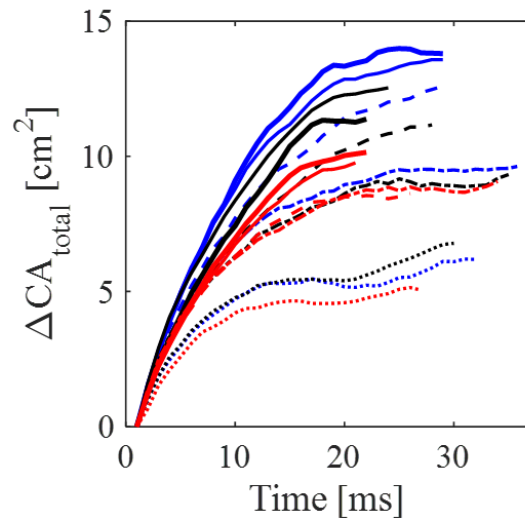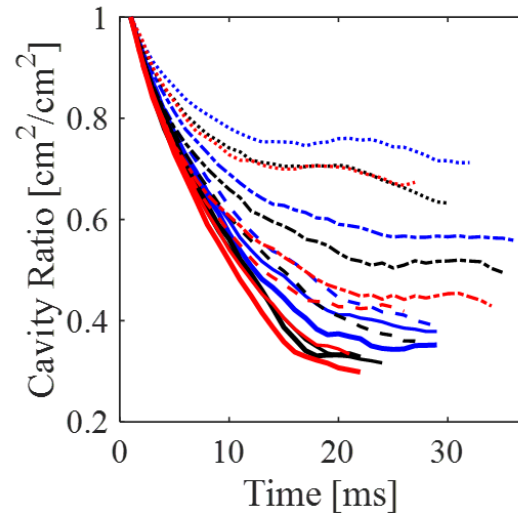
Fig. 3.16: (a) Cavity area plot comparing different impact velocities and area ratios for a single vented tube length: $L = 15.24$ cm. (b) Total change in cavity area as function of time and (c) ratio of remaining cavity to initial lower cavity as a function of time over the deflation period for the seven vented tube cases that deflate. For all cases the sphere diameter is $D = 2.54$ cm, the contact angle is $\theta = 117°$, and the vented tube diameter is $d = 1.27$ cm.

$U_o = 2.6$ m/s and $U_o = 2.2$ m/s cases deflate a similar amount relative to the initial lower cavity. Fifth, all of the cavities deflate until they reach the vent holes ($U_o = 2.6$ m/s, $A_r = 1$; $U_o = 2.6$ m/s, $A_r = 2$; $U_o = 2.2$ m/s, $A_r = 1$; $U_o = 2.2$ m/s, $A_r = 2$) or begin to shed (all other cases).

3.2.6 Impact Velocity and Vented Tube Length

All four vented tube lengths ($L = 3.81$ cm, $L = 7.62$ cm, $L = 11.43$ cm, $L = 15.24$ cm) for all three impact velocities ($U_o = 3.0$ m/s, $U_o = 2.6$ m/s, $U_o = 2.2$ m/s) are compared in the cavity area and deflation plots in Fig. 3.17. For all vented tube cases the vented tube diameter is $d = 1.27$ cm and the area ratio is $A_r = 1$. Fig. 3.17 highlights the combined effects of impact velocity and vented tube length on cavity deflation. First, none of the $L = 3.81$ cm vented tube cases deflate which is expected as for all four vented tube lengths the vented tube is fully within the cavity. Second, for all three vented tube length cases that deflate the size of the initial lower cavity after deep seal and the size of the cavity remaining at the end of deflation increase as the impact velocity increases. Third, the upper cavity seal time increases as the vented tube length increases and as the impact velocity decreases. Fourth, for all three impact velocities the amount deflation, both the total change in area and the ratio of the remaining cavity to the initial lower cavity, increases as the vented tube length increases. Fifth, the difference in the total change in area between the vented tube lengths decreases as the impact velocity decreases. Sixth, for all three vented tube length cases that deflate, the highest impact velocity has the least amount of deflation relative to initial lower cavity while lowest impact has most amount deflation relative to the initial lower cavity, except for $L = 15.24$ cm where the $U_o = 2.2$ m/s and $U_o = 2.6$ m/s cases have a similar amount of deflation relative to the initial lower cavity. Seventh, for the $L = 7.62$ cm vented tube cases the deflation time is similar for all three impact velocities with deflation ending abruptly when cavity ripples begin to form. Eighth, for the $L = 11.43$ cm and $L = 15.24$ cm vented tube cases the cavities deflate until they reach the vent holes ($U_o = 2.6$ m/s, $L = 15.24$ cm; $U_o = 2.2$ m/s, $L = 15.24$ cm) or begin to shed (all other cases).
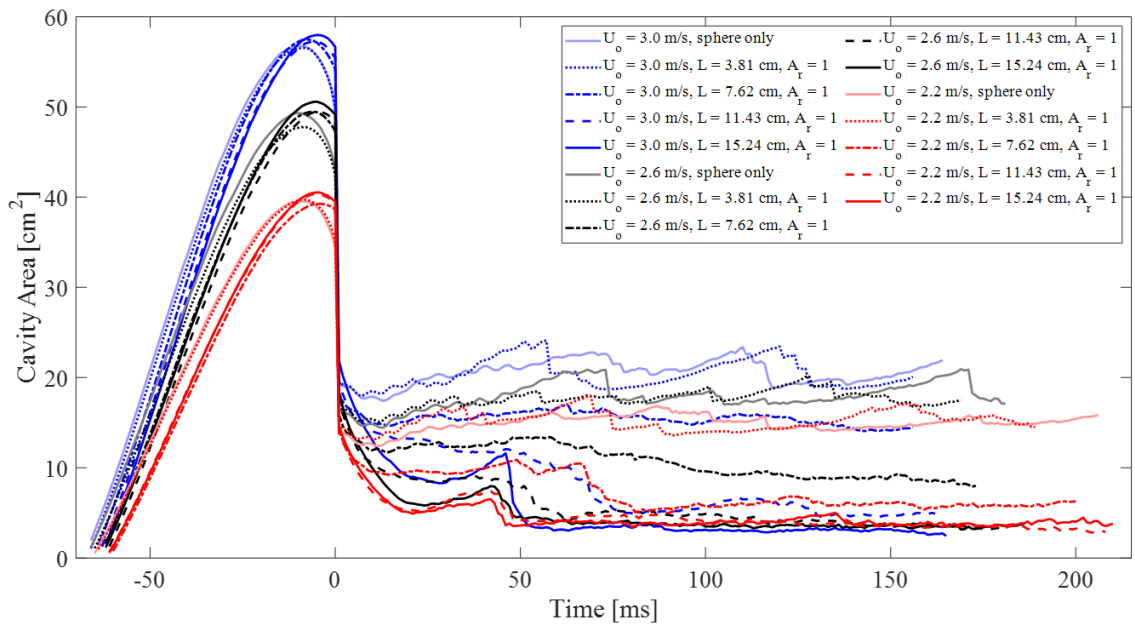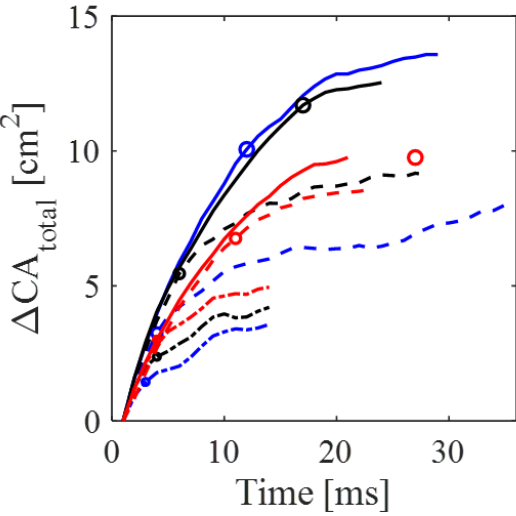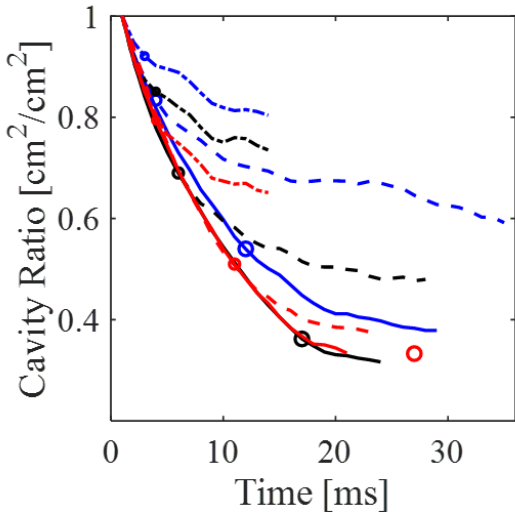
Fig. 3.17: (a) Cavity area plot comparing different impact velocities and vented tube lengths for a single area ratio: $A_r = 1$. (b) Total change in cavity area as function of time and (c) ratio of remaining cavity to initial lower cavity as a function of time over the deflation period for the seven vented tube cases that deflate. The upper cavity seal time is marked in (b) and (c) by 'o'. For all cases the sphere diameter is $D = 2.54$ cm, the contact angle is $\theta = 117°$, and the vented tube diameter is $d = 1.27$ cm.

3.2.7 Deflation Summary

The effects of vented tube length, area ratio, and impact velocity on cavity deflation are summarized in Fig. 3.18 which presents the deflation time, the change in cavity area over the deflation period, and the ratio of the remaining cavity at the end of deflation to the initial lower cavity for the deflation cases tested in this study. Fig. 3.18(b)-(c) show that vented tube length has the greatest effect on cavity deflation for the parameter ranges tested with a definite increase in deflation as the vented tube length increases, particularly at larger area ratios. For the $L = 7.62$ cm vented tube cases, the amount of deflation is similar across all five area ratios. For the $L = 11.43$ cm and $L = 15.24$ cm vented tube cases, the amount of deflation increases as the area ratio increases up until $A_r = 1$ and then $A_r = 1$ and $A_r = 2$ vented tube cases have a similar amount of deflation which indicates there is a limit between $A_r = 0.5$ and $A_r = 1$ for the impact of increasing area ratio.

The effect of impact velocity on cavity deflation for the parameter ranges tested depends on the vented tube length and the deflation comparison. In general, the change in cavity area over the deflation period (Fig. 3.18(b)) increases as the impact velocity decreases for the $L = 7.62$ cm and $L = 11.43$ cm vented tube cases and increases as the impact velocity increases for the $L = 15.24$ cm vented tube cases. When comparing the ratio of the remaining cavity after deflation to the initial lower cavity after deep seal (Fig. 3.18(c)), the amount of deflation relative to the initial lower cavity increases as the impact velocity decreases for all three vented tube lengths. Fig. 3.18(a) shows that, for the parameter ranges tested, the deflation time for the $L = 7.62$ cm vented tube cases is similar for all cases while the deflation time for the $L = 11.43$ cm and $L = 15.24$ cm vented tube cases vary with area ratio. In general, for the $L = 11.43$ cm and $L = 15.24$ cm vented tube cases, higher impact velocities have longer deflation times.

3.2.8 Post-Deflation

There are two observation of note regarding the cavities after deflation. The first observation is that how the cavities shed after deflation varies with vented tube length, area ratio, and impact velocity. Shortly after deflation, all $L = 15.24$ cm vented tube cases
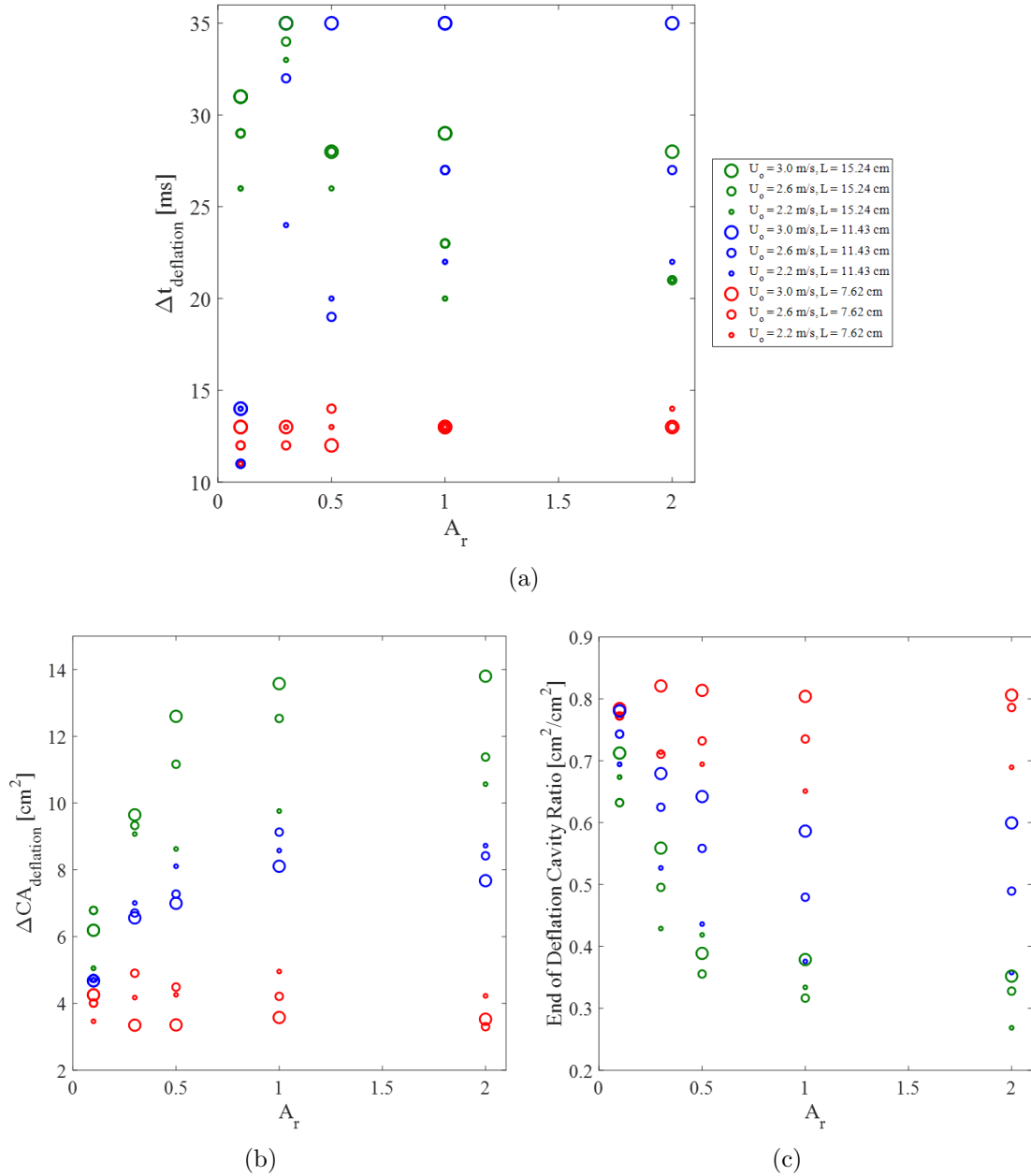
Fig. 3.18: (a) Comparison of deflation time, (b) change in cavity area over the deflation period, and (c) ratio of remaining cavity at the end of deflation to initial lower cavity. For all cases the sphere diameter is $D = 2.54$ cm, the contact angle is $\theta = 117°$, and the vented tube diameter is $d = 1.27$ cm.

tested (Fig. 3.16(a)) shed a significant portion of the remaining cavity. As the size of the cavity remaining after deflation increases (which occurs as area ratio decreases and as

impact velocity increases) the volume of the air bubble shed increases so that the amount of cavity remaining after deflation is similar for all $L = 15.24$ cm vented tube cases, between 2 and 5 cm^2. Additionally, as the volume of the bubble increases, the time it takes the cavity to shed the bubble increases. For the $L = 11.43$ cm vented tube cases that are plotted (Fig. 3.13(a), Fig. 3.17(a)), the shedding trend after deflation is similar to the trend seen for $L = 15.24$ cm, with all cases reaching a cavity area between 2 and 5 cm^2 except the $U_o = 2.6$ m/s, $A_r = 0.1$ case which steadily sheds smaller air bubbles and only reaches a cavity area of 9 cm^2. For a given area ratio or impact velocity, the air bubble volume and time it takes the air bubble to shed increases for the 11.43 cm vented tube case compared to the 15.24 cm vented tube case as the cavity after deflation is larger.

For the $L = 7.62$ cm vented tube cases that are plotted (Fig. 3.13(a), Fig. 3.17(a)), the amount of shedding varies based on the impact velocity. For $U_o = 2.2$ m/s, the cavity sheds a significant portion of the remaining cavity shortly after deflation, reaching a cavity area around 6 cm^2. For $U_o = 2.6$ m/s, the cavities steadily shed small air bubbles and reach a cavity area around 11 cm^2. For $U_o = 3.0$ m/s, the cavity area profile after deflation is similar to the sphere only case and $L = 3.81$ cm vented tube case cavity area profiles, indicating that the cavity is periodically releasing small bubbles. In the image sequences for the $A_r = 4$ and $A_r = 10$ vented tube cases (Fig. 3.10(g)-(h)), shedding around the vented tubes is not observed but looking at the vented tubes, the top of the cavity is releasing air bubbles inside of the vented tube.

The second observation is that for cases where the cavity reaches the vent holes, by deflation or by shedding, the vented tube subsequently begins to fill with water that mixes with the air in the vented tube.

3.2.9   Vented Tube Diameter

The results presented in this section look at how vented tube diameter impacts cavity deflation. Two vented tube diameters ($d = 0.635$ cm, $d = 1.27$ cm) for three area ratios ($A_r = 0.5$, $A_r = 1$, $A_r = 2$) are compared in the image sequences in Fig. 3.19 and the cavity area and deflation plots in Fig. 3.20. For all cases the impact velocity is $U_o = 2.6$ m/s and
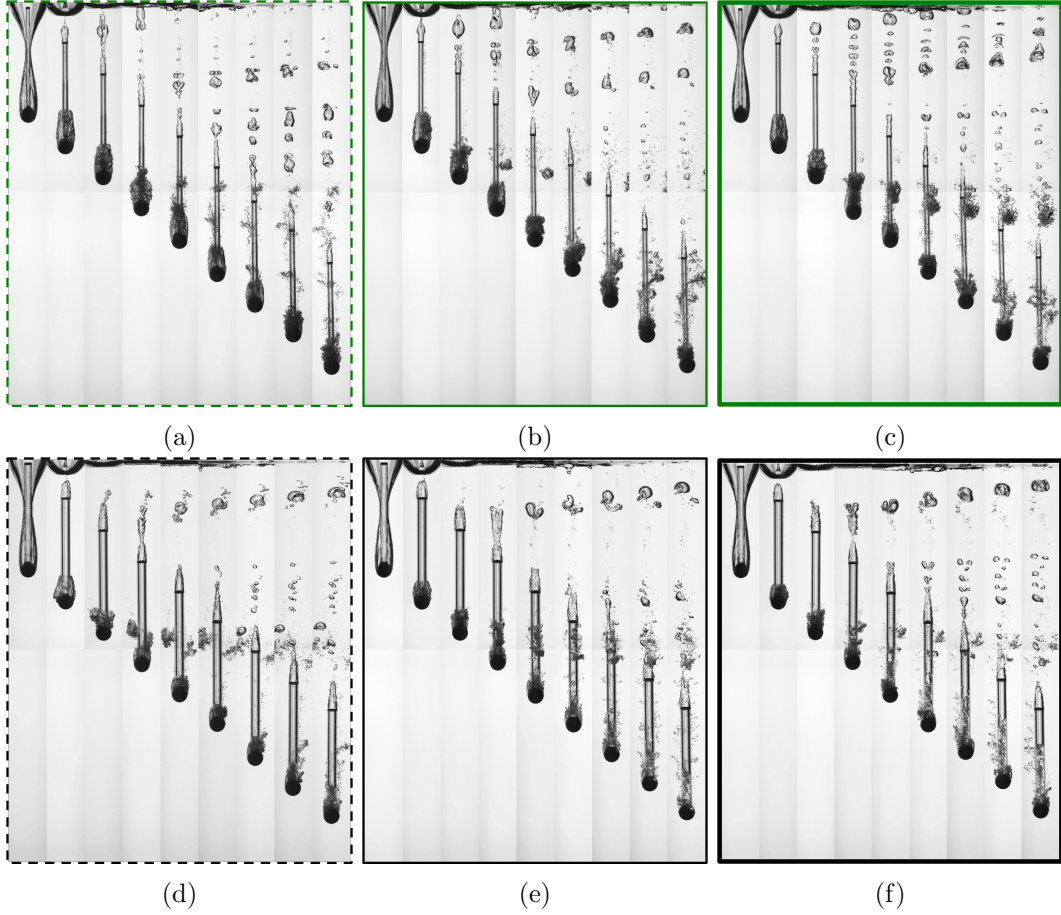
Fig. 3.19: Image sequences comparing two vented tube diameters for three area ratios: (a) vented tube diameter $d = 0.635$ cm, area ratio $A_r = 0.5$; (b) vented tube diameter $d = 0.635$ cm, area ratio $A_r = 1$; (c) vented tube diameter $d = 0.635$ cm, area ratio $A_r = 2$; (d) vented tube diameter $d = 1.27$ cm, area ratio $A_r = 0.5$; (e) vented tube diameter $d = 1.27$ cm, area ratio $A_r = 1$; f) vented tube diameter $d = 1.27$ cm, area ratio $A_r = 2$. For all cases the impact velocity is $U_o = 2.6$ m/s, the sphere diameter is $D = 2.54$, the contact angle is $\theta = 117°$, and the vented tube length is $L = 15.24$. For all six image sequences the time starts at deep seal and the time between frames is $\Delta t = 20$ ms.

for all vented tube cases the vented tube length is $L = 15.24$ cm. For the six vented tube cases, the second frame of the image sequences (Fig. 3.19) and the cavity area profiles (Fig. 3.20(a)) after deep seal show all six cavities deflate but the amount of deflation for the three $d = 0.635$ cm vented tube cases is significantly less compared to the three $d = 1.27$ cm vented tube cases. Two aspects of the vented tube diameter impact the amount of deflation. First, a change in diameter changes the volume of the vented tube and second, for a given
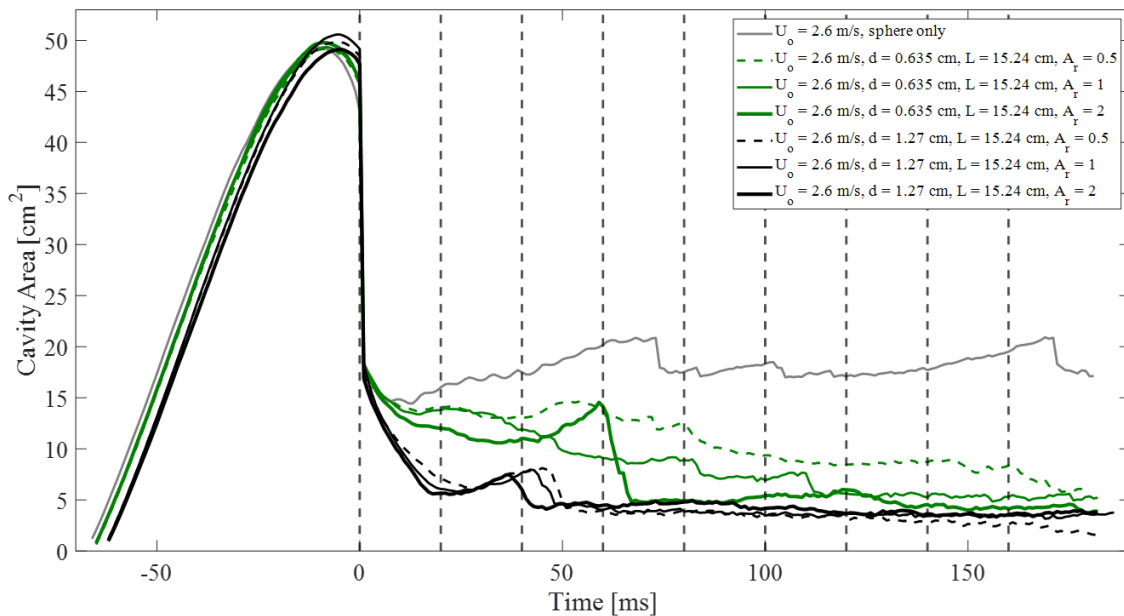
(a)
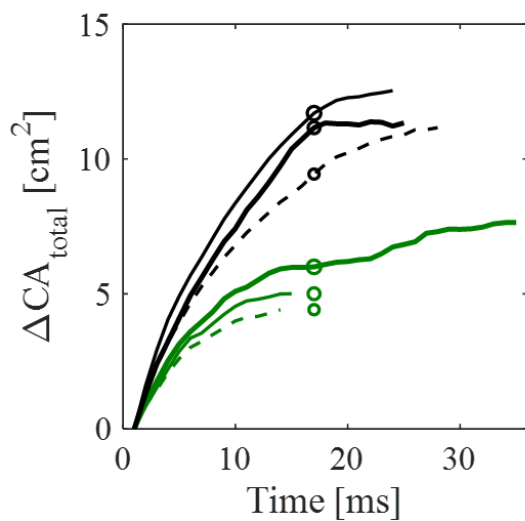
(b)
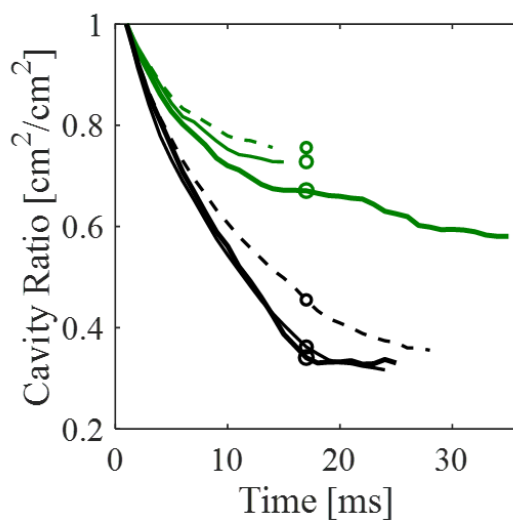
(c)

Fig. 3.20: (a) Cavity area plot comparing two vented tube diameters ($d = 0.635$, $d = 1.27$) for three area ratios ($A_r = 0.5$, $A_r = 1$, $A_r = 2$). (b) Total change in cavity area as function of time and (c) ratio of remaining cavity to initial lower cavity as a function of time over the deflation period for the seven vented tube cases that deflate. For all cases the impact velocity is $U_o = 2.6$ m/s, the sphere diameter is $D = 2.54$, the contact angle is $\theta = 117°$, and the vented tube length is $L = 15.24$. The vertical dashed lines correspond with each frame of the image sequences in Fig. 3.19.

area ratio a change in diameter changes the area of the vented tube opening and therefore the vent hole area.

As the diameter of the $d = 0.635$ cm vented tube is half the diameter of the $d = 1.27$ cm vented tube, the vent hole area for the $d = 0.635$ cm vented tube is half the vent hole area for the $d = 1.27$ cm vented tube which reduces the amount of air that can enter the vented tube at a given time. The vent hole areas for the $d = 0.635$, $A_r = 2$ vented tube case and $d = 1.27$, $A_r = 0.5$ vented tube case are the same, but as the diameter decreases the volume decreases which also reduces the amount air that can enter the vented tube at a given time. The difference in the amount of air that is able to enter the vented tube and escape to the free surface at a given time for the two vented tube diameters is observed in the cavity deflation rates before upper cavity seal (Fig. 3.20(b)-(c)). After upper cavity seal the $d = 1.27$ cm, $A_r = 1$ and $d = 1.27$ cm, $A_r = 2$ vented tube cases continue to deflate until the cavity reaches the vent holes holes and the $d = 1.27$ cm, $A_r = 0.5$ and $d = 0.635$ cm, $A_r = 2$ vented tube cases continue to deflate until the cavity begins to shed. The $d = 0.635$ cm, $A_r = 0.5$ and $d = 0.635$ cm, $A_r = 1$ vented tube cases though, stop deflating before the upper cavity seals, when cavity ripples form, suppressing deflation similar to the $L = 7.62$ cm vented tube cases presented in earlier sections.

3.2.10   Surface Seal

The results presented in this section look at how surface seal affects cavity deflation. A sphere only case and three area ratio cases ($A_r = 0.5$, $A_r = 1$, $A_r = 2$) are compared in the image sequences in Fig. 3.21 and the cavity area plot in Fig. 3.22. For all cases, the impact velocity is $U_o = 5.9$ m/s. For all vented tube cases the vented tube diameter is $d = 1.27$ cm and the vented tube length is $L = 22.86$ cm. A longer vented tube was manufactured for the surface seal vented tube cases so that the vented tube would be outside of the surface seal cavity after the first deep pinch-off. For the surface seal cavity plot (Fig. 3.22), surface seal does not occur at $t = 0$ ms but rather the first deep pinch-off occurs at $t = 0$ ms as that is when the vented tube is outside of the cavity and deflation begins. The time surface seal occurs is labeled on the first frame of the image sequences (Fig. 3.21). The second frame

$t = -21$

(a)

$t = -17$

(b)

$t = -12$

(c)

$t = -11$

(d)
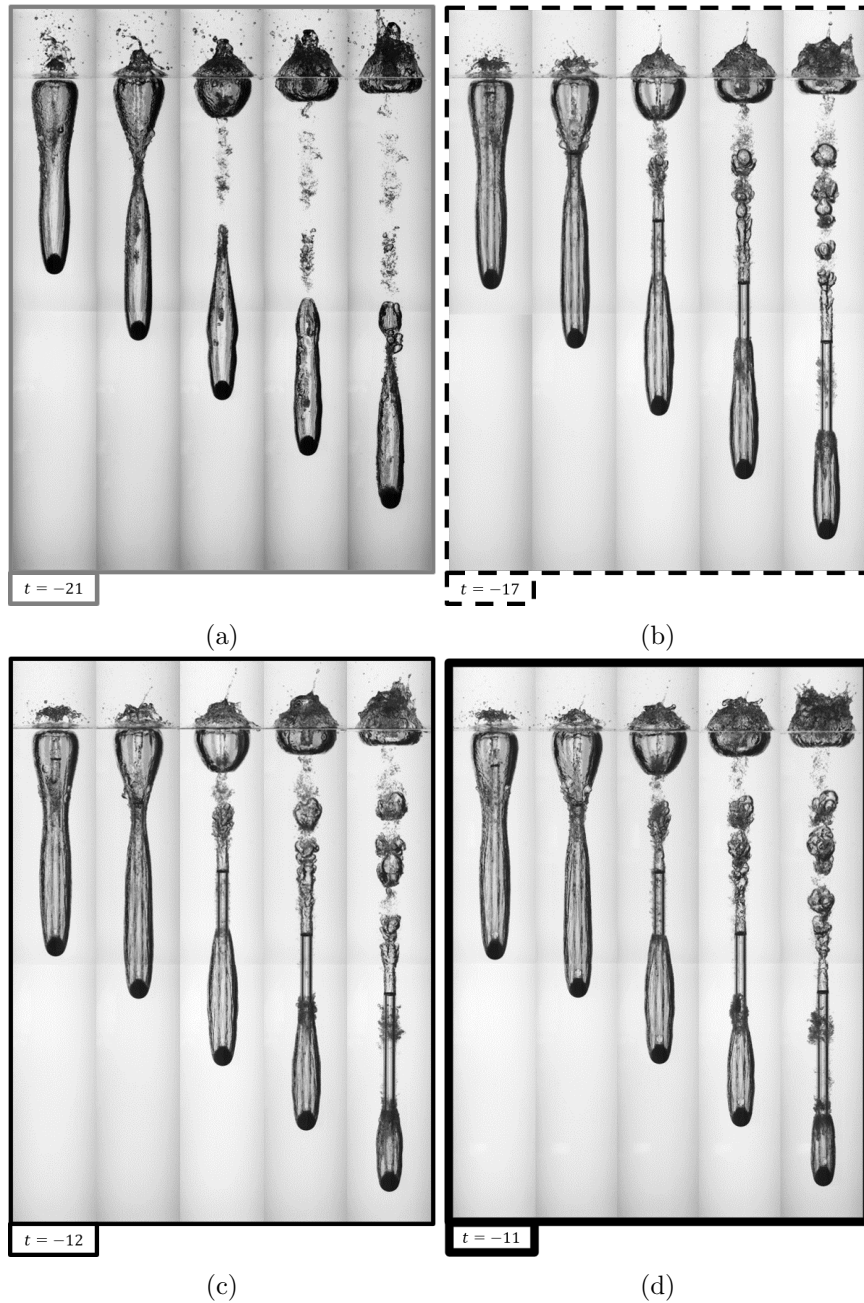
Fig. 3.21: Image sequences comparing surface seal for (a) sphere only case and three area ratio cases: (b) $A_r = 0.5$, (c) $A_r = 1$, and (d) $A_r = 2$. For all cases the impact velocity is $U_o = 5.9$ m/s, the sphere diameter is $D = 2.54$ cm, and the contact angle is $\theta = 117°$. For all vented tube cases the vented tube diameter is $d = 1.27$ cm and the vented tube length is $L = 22.86$ cm. For all four image sequences the first frame is surface seal and the time is marked below the frame. The second frame is when the first deep pinch-off occurs ($t = 0$ ms) and the time between the remaining frames is $\Delta t = 20$ ms.

of the image sequences (Fig. 3.21) is the first deep pinch-off ($t = 0$ ms) and the time between the remaining frames is 20 ms.

The image sequence (Fig. 3.21(a)) and cavity area profile (Fig. 3.22) after deep pinch-off for the surface seal sphere only case show that the cavity remains relatively constant except for the release of air bubbles, as expected. The image sequences (Fig. 3.21(b)-(d)) and cavity area profiles (Fig. 3.22) after deep pinch-off for the surface seal vented tube cases show that the cavities do deflate and are reduced compared to the surface seal sphere only case. As seen for deep seal cases, the amount of deflation increases as the area ratio increases. As surface seal occurs at higher impact velocities the cavities descend faster compared to the deep seal cavities and are out of frame before deflation ends. A deeper tank would be required for an in-depth comparison of surface seal cavity deflation.
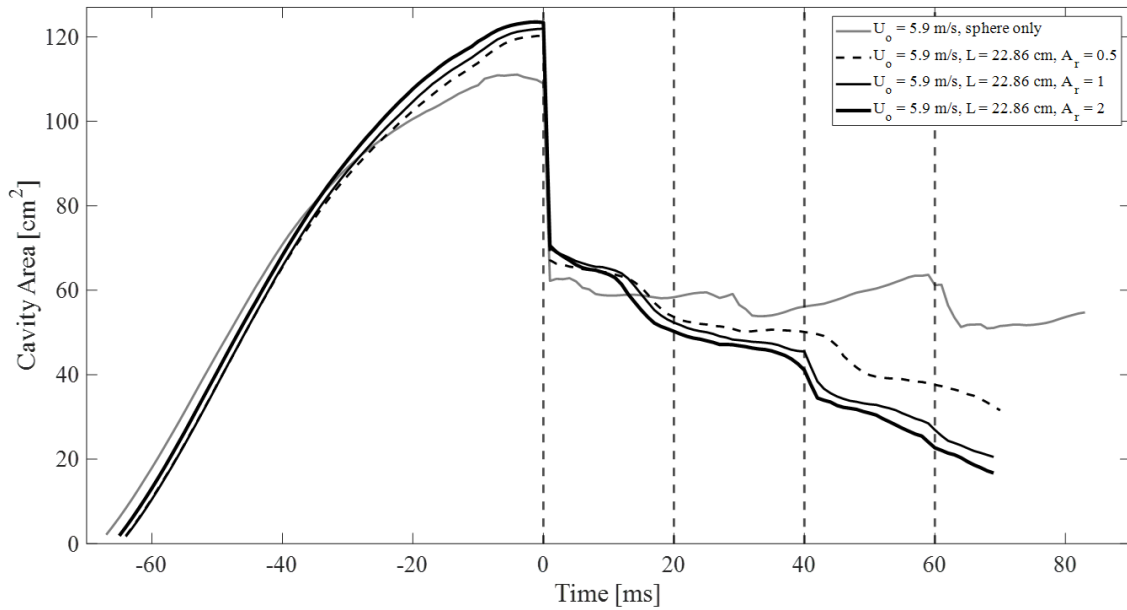
Fig. 3.22: Cavity area plot comparing surface seal for sphere only case and three area ratio cases: $A_r = 0.5$, $A_r = 1$, and $A_r = 2$. For all cases the impact velocity is $U_o = 5.9$ m/s, the sphere diameter is $D = 2.54$ cm, and the contact angle is $\theta = 117°$. For all vented tube cases the vented tube diameter is $d = 1.27$ cm and the vented tube length is $L = 22.86$ cm. The cavity area profiles are aligned so that first deep pinch-off after surface seal is at $t = 0$. Surface seal is not marked on the plots but the times are marked in Fig. 3.21. The vertical dashed lines correspond with frames 2-5 of the image sequences in Fig. 3.21.

3.2.11 Critical Vented Tube Length

The results presented in Section 3.2.1-3.2.6 and Section 3.2.9 show that deflation occurs if the vented tube is outside of the lower cavity at deep seal which allows the air to escape from the cavity to the free surface through the vented tube. The vented tube is outside of the cavity if deep seal occurs on the vented tube and the results show that impact velocity affects the deep seal depth. To determine the vented tube length required for deflation to occur, the length of the lower cavity at deep seal as a function of impact velocity is needed. Duclaux, et al. [3] developed an analytic solution to model the evolution of a cavity and found that the deep seal depth (H_p) is half the cavity depth (H) and that the cavity depth at deep seal is a function of Froude number. The deep seal depth and cavity depth at deep seal are labeled in Fig. 3.23(a) along with the sphere radius (R) and cavity opening diameter ($2R_c$).

If the deep seal depth is half the cavity depth at deep seal then the lower cavity length at deep seal is equal to the seal depth. Vented tube deep seal occurs a few milliseconds before natural deep seal but the difference in depth is small and pinch-off still occurs at roughly half the cavity depth. For the vented tube to be outside of the cavity, the vented tube length plus the radius of the vented tube must be greater than the seal depth.

$$L + R > H_p \tag{3.1}$$

The inequality in (3.1) is solved to find an equation for the critical vented tube length for which deflation will occur.

$$L_{critical} = H_p - R \tag{3.2}$$

The equations for deep seal depth and cavity depth at deep seal are presented in (3.3) and (3.4), respectively.

$$H_p = \frac{1}{2}H \tag{3.3}$$

(a)   (b)
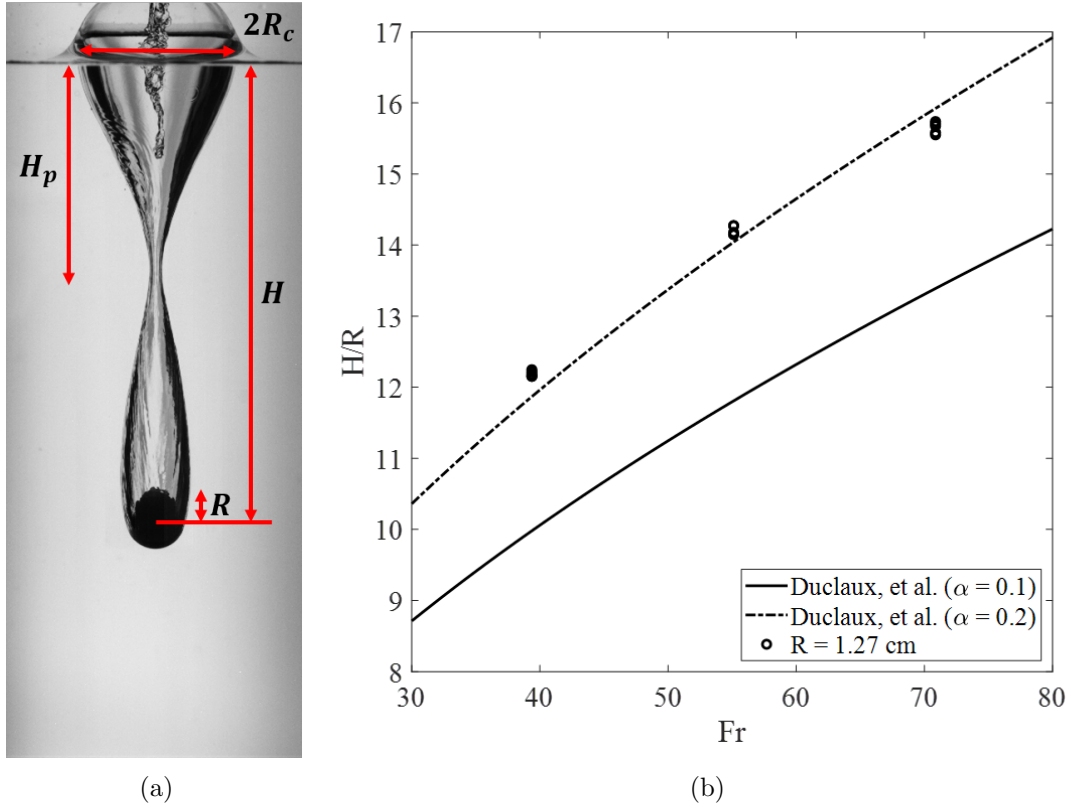
Fig. 3.23: (a) Parameters used to formulate critical vented tube length. (b) Cavity depth at deep seal as a function of Froude number for the three sphere only cases used in the cavity area study. Five trials are plotted for each cases. Theoretical cavity depth developed by Duclaux [3], $H/R = \sqrt{8\sqrt{\alpha}Fr}$, is plotted for $alpha = 0.1$ (solid line) and $alpha = 0.2$ (dashed line). For all cases the sphere diameter is $D = 2.54$ cm and the contact angle is $\theta = 117°$.

$$\frac{H}{R} = \sqrt{8\sqrt{\alpha}Fr} \tag{3.4}$$

Ducalux, et al. [3] selected $\alpha = 0.1$ for which the theoretical cavity depth was in good agreement with their experimental data. The experimental cavity depth for the sphere only cases presented in the cavity area study are plotted as a function of Froude number in Fig. 3.23(b) along with the theoretical cavity depth for $\alpha = 0.1$ (solid line) and $\alpha = 0.2$ (dashed line). For this set of data, the selection of $\alpha = 0.1$ underpredicts the cavity depth, but for $\alpha = 0.2$ the theoretical cavity depth is in good agreement with the experimental

data. Substituting (3.3) and (3.4) into (3.2) with $\alpha = 0.2$, the theoretical critical vented tube length as function of impact velocity and sphere radius is

$$\frac{L_{critical}}{R} = 0.946\sqrt{Fr} - 1 \tag{3.5}$$

The theoretical critical vented tube length as a function of Froude number is presented in Fig. 3.24 along with the vented tube lengths used in the cavity area study and whether the vented tube is outside of the lower cavity (open symbols) or inside the lower cavity (closed symbol) at deep seal for each impact velocity. As seen in Section 3.2.1-3.2.6 and Section 3.2.9, for all cases where the vented tube is outside of the lower cavity at deep seal, some amount of deflation occurs and for all cases where the vented tube is inside of the lower cavity at deep seal no deflation occurs. Fig. 3.24 shows that the theoretical critical vented tube length accurately predicts that the $L = 3.81$ cm vented tube is inside of the cavity and that the $L = 11.43$ cm and $L = 15.24$ cm vented tubes are outside of the cavities for all three impact velocities tested. There is a discrepancy though for the $L = 7.62$ cm vented tube. Based on the theoretical critical vented tube length, the vented tube should be inside the cavity at the highest impact velocity and therefore no deflation should occur but the cavity area results showed that these cases did deflate. The discrepancy is explained by the image sequences presented in Fig. 3.25 of the $L = 7.62$ cm, $A_r = 1$ vented tube case for the three impact velocities tested. The first frame of the image sequences occurs at deep seal and the second frame occurs 1 ms after deep seal. For $U_o = 2.2$ m/s (Fig. 3.25(a)), deep seal occurs on the vented tube, just below the top of the vented tube, and the vented tube is outside of the cavity as expected based on the cavity area results and as predicted in Fig. 3.24. For $U_o = 2.6$ m/s (Fig. 3.25(b)) and $U_o = 3.0$ m/s (Fig. 3.25(c)), deep seal should occur at the top of the vented tube and above the vented tube, respectively, but because the cavity is tapered, and the diameter of the vented tube is wider than the taper, the vented tube punctures the walls of the cavity, creating an early secondary pinch-off. For vented tube lengths near the deep seal depth, the diameter of the vented tube needs to be considered to accurately predict if the vented tube will be outside of cavity or not.
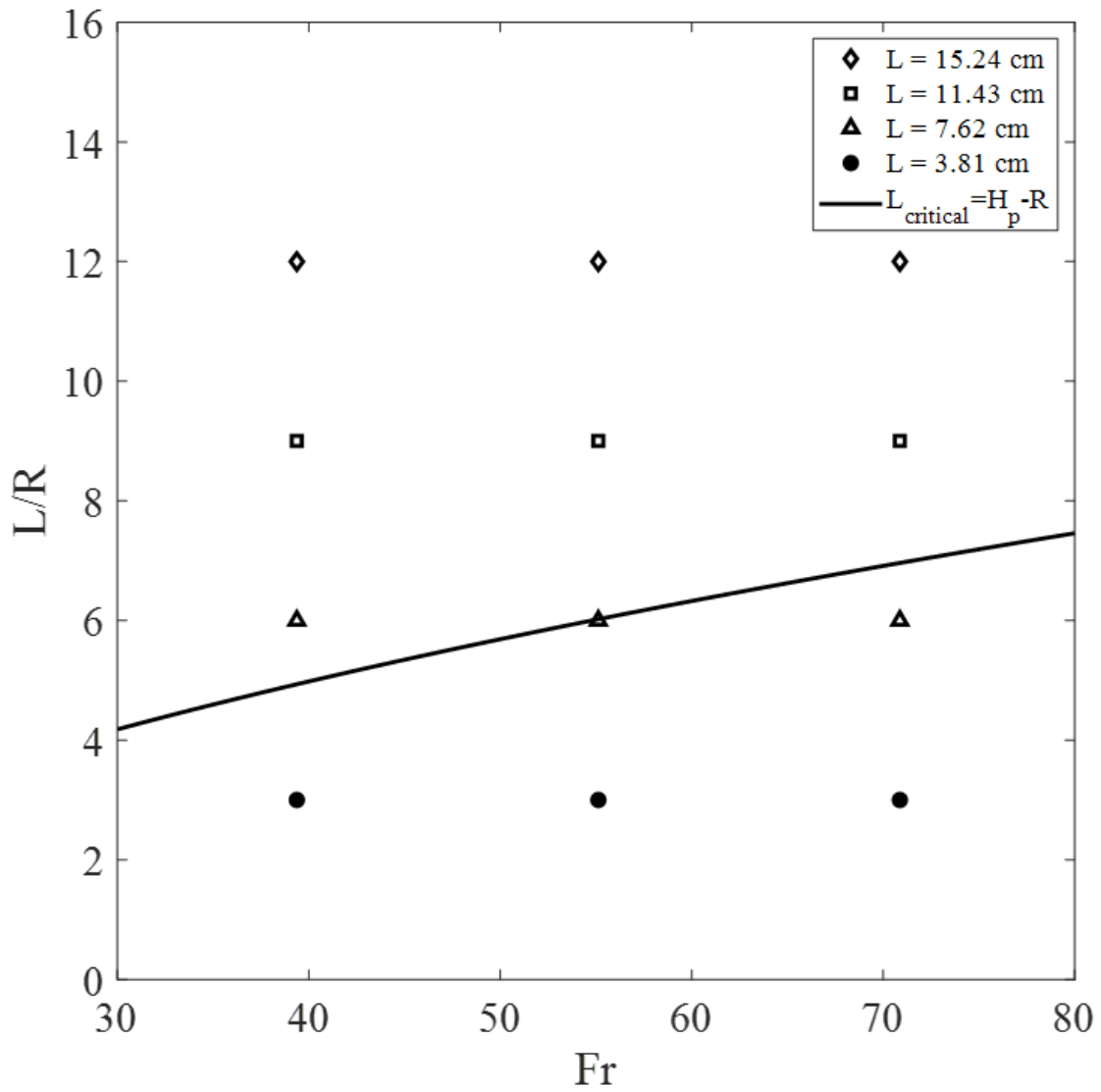
Fig. 3.24: Theoretical critical vented tube length as a function of Froude number, $L_{critical} = H_P - R$, and vented tube lengths used in the cavity area study. An open symbol designates the vented tube is outside of the lower cavity at deep seal and a closed mark designates the vented tube is inside the lower cavity at deep seal. For each vented tube length at each impact velocity, 25 trials were tested (five area ratios, five trials per area ratio). All of the vented tubes for each set of 25 trials were either all outside or all inside of the cavity.
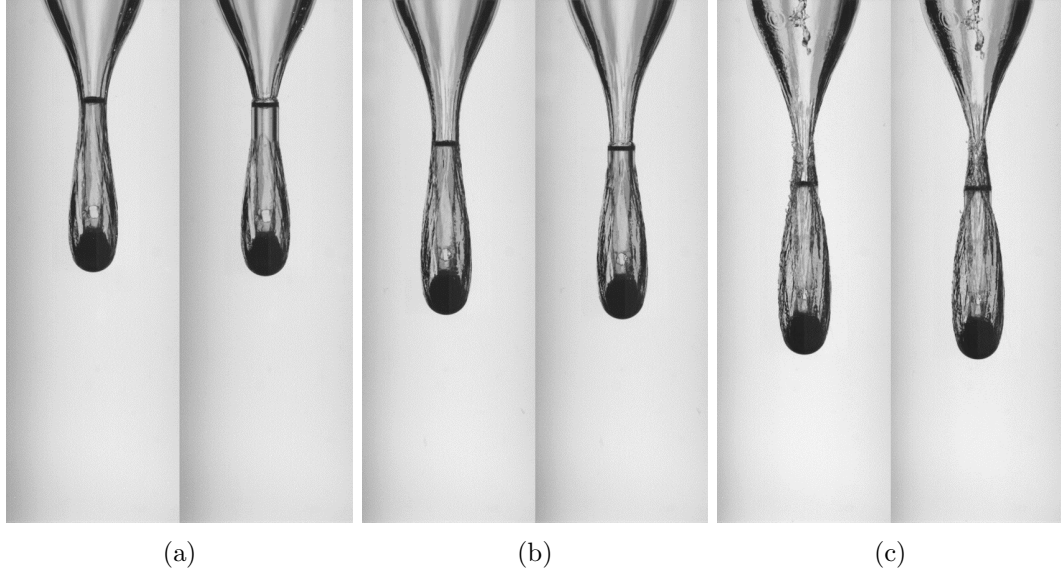
Fig. 3.25: Image sequences of $L = 7.62$ cm, $A_r = 1$ vented tube case for (a) $U_o = 2.2$ m/s, (b) $U_o = 2.6$ m/s, and (c) $U_o = 3.0$ m/s. For all three image sequences the first frame occurs at deep seal and the second frame occurs 1 ms after deep seal.

To account for the vented tube diameter in the critical vented tube length equation, similar triangles, seen in Fig. 3.26(a), are used to find where the secondary pinch-off due to the vented tube diameter occurs, and the taper length (l_t) above this point that needs to be subtracted from the lower cavity length. As the triangles are similar right triangles the ratio of the bases is equal to the ratio of the heights.

$$\frac{A0}{AF} = \frac{DE}{BC} \tag{3.6}$$

The height of the large triangle (AF) is the lower cavity length (H_p) and the height of the small triangle (AO) is the taper length (l_t) from the top of the lower cavity to where secondary pinch-off occurs. Points D and E are the location on the cavity wall where the secondary pinch-off occurs and the base of the small triangle (DE) is the vented tube diameter (d). For the taper length to be as accurate as possible, points D and E need to be located on the edge of the cavity which means that the taper of the triangle needs to follow the taper of the lower cavity as close as possible. The taper of the lower cavity is similar to
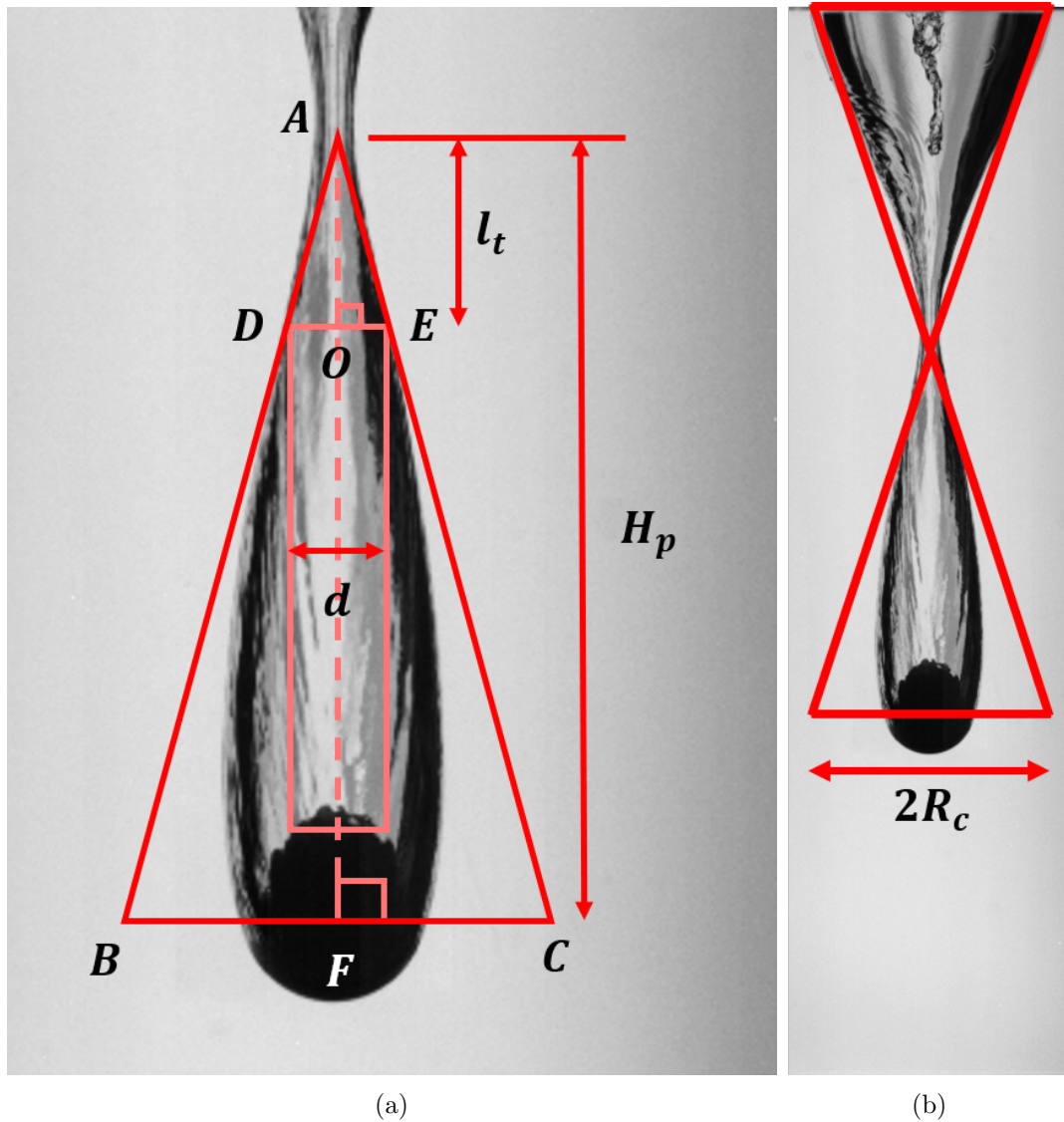
Fig. 3.26: (a) Similar triangles diagram used to find where the secondary pinch-off due to the vented tube diameter occurs and the taper length above this point. (b) Diagram showing upper cavity triangle that matches lower cavity triangle used to find base of triangle ABC in (a).

the taper of the upper cavity which is roughly a triangle, as seen in Fig. 3.26(b), with the same height as the lower cavity triangle as $H_p = \frac{1}{2}H$. If the upper cavity is mirrored over the deep seal point, the base of the large triangle (BC) that follows the taper of the cavity is then the cavity opening diameter ($2R_c$). Substituting the triangle heights (l_t, H_p) and triangle bases (d, $2R_c$) into (3.6) and solving for l_t yields an equation for the taper length.

$$l_t = \frac{H_p d}{2R_c} \tag{3.7}$$

Aristoff and Bush [1] further developed the Duclaux et al. cavity evolution model to account for aerodynamic pressure and surface tension and found the cavity opening radius (R_c) as a function of pinch-off time (t_p).

$$\frac{R_c}{R} = \left(\frac{U_o t_p}{R}\right)^{2/5} \tag{3.8}$$

Fig. 3.27 presents the cavity opening radius as a function of pinch-off time for five sphere diameters. The dashed line is the theoretical cavity opening developed by Aristoff and Bush, presented in (3.8). The theoretical cavity opening radius is in reasonable agreement with the experimental data. For the cavity opening radius (R_c) to be consistent with the lower cavity length (H_p), the cavity opening radius needs to be a function of Froude number. Previous studies have shown that $U_o t_p / R \approx Fr^{1/2}$ [9] [4] which, when substituted into (3.8), yields an equation for the cavity opening radius as a function of Froude number.

$$\frac{R_c}{R} = Fr^{1/5} \tag{3.9}$$

Substituting (3.9), (3.3), and (3.4) into (3.7) yields the taper length as function of Froude number and vented tube diameter.

$$\frac{l_t}{R} = \frac{0.946 d\sqrt{Fr}}{2R Fr^{1/5}} \tag{3.10}$$

Subtracting (3.10) from (3.5), the theoretical critical vented tube length as function of impact velocity, sphere radius, and vented tube diameter is

$$\frac{L_{critical}}{R} = 0.946\sqrt{Fr} - 1 - \frac{0.946 d\sqrt{Fr}}{2R Fr^{1/5}} \tag{3.11}$$
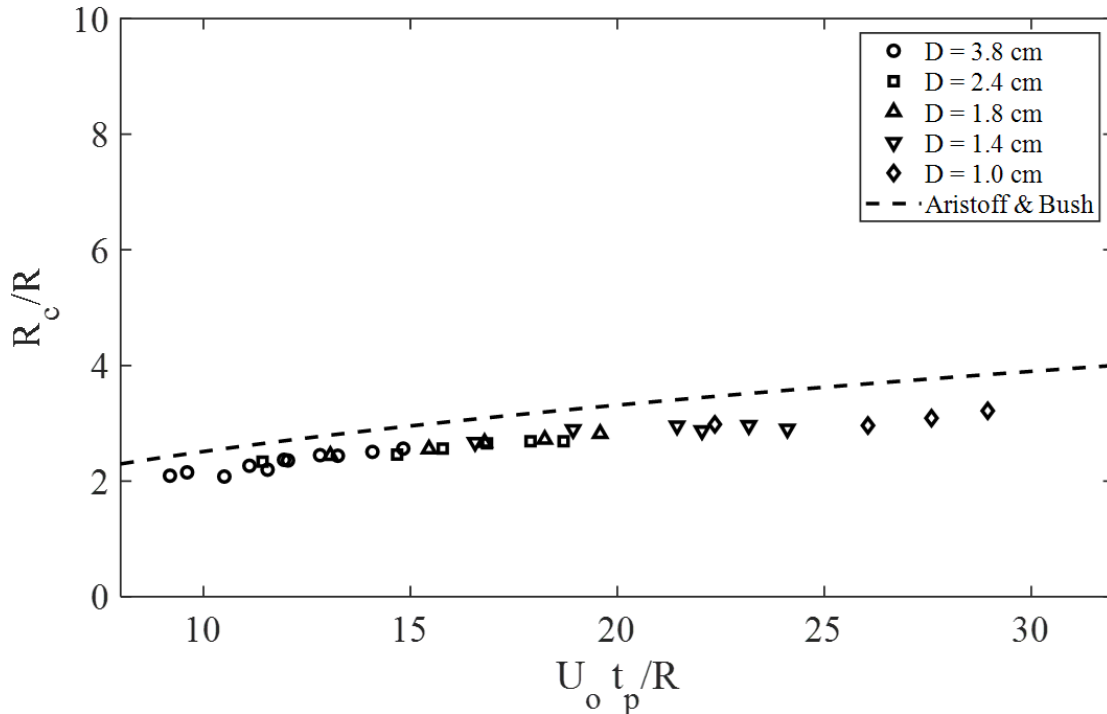
Fig. 3.27: Cavity opening radius as a function of pinch-off time for five sphere diameters. The experimental cavity opening radii are computed from raw data from Rabbi, et al. [4]. The dashed line is the theoretical cavity opening formula developed by Aristoff and Bush [1], $R_c/R = (U_o t_p/R)^{2/5}$.)

The updated theoretical critical vented tube length as a function of Froude number (red line) and original theoretical critical vented tube length as a function of Froude number (black line) are presented in Fig. 3.28 along with the vented tube lengths used in the cavity area study and whether the vented tube is outside of the lower cavity (open symbols) or inside the lower cavity (closed symbol) at deep seal for each impact velocity. The updated theoretical critical vented tube length equation now accurately predicts whether the vented tube is outside or inside of the lower cavity at deep seal for the experimental data. Additionally, the vented tube length that punctures the cavity is found from the sphere only high-speed camera images for each impact velocity tested using image processing, and these lengths match the updated theoretical critical vented tube lengths at each impact velocity. When designing a sphere-vented tube device for an application, (3.11) can be used

to determine the minimum vented tube length required for deflation to occur for a selected impact velocity, sphere radius, and vented tube diameter.
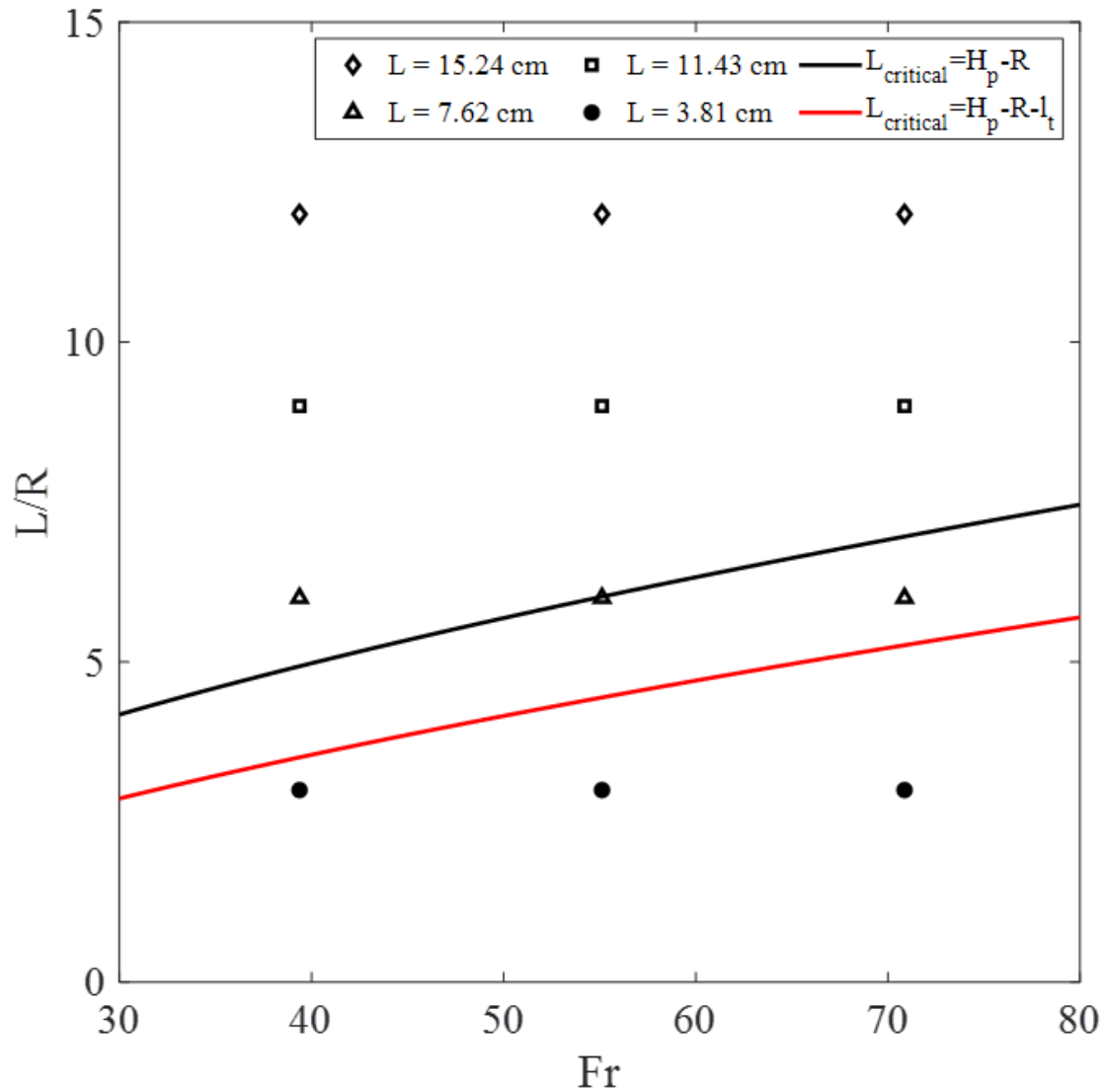
Fig. 3.28: Updated theoretical critical vented tube length as a function of Froude number (red line), $L_{critical} = H_P - R - l_t$, original theoretical critical vented tube length as a function of Froude number (black line), $L_{critical} = H_P - R$, and vented tube lengths used in the cavity area study (markers). An open symbol designates the vented tube is outside of the lower cavity at deep seal and a closed mark designates the vented tube is inside the lower cavity at deep seal. For each vented tube length at each impact velocity, 25 trials were tested (five area ratios, five trials per area ratio). All of the vented tubes for each set of 25 trials were either all outside or all inside of the cavity.

CHAPTER 4

ACOUSTIC STUDY

This chapter presents the data processing methods and results for the acoustic study. The parameters for this study are presented in table 2.1. For all cases presented in this chapter the sphere diameter is $D = 2.54$ cm, the contact angle is $\theta = 117°$, and the impact velocity is $U_o = 2.6$ m/s.

4.1   Data Processing

This section describes the signal processing methods used to process the hydrophone data. The hydrophone and camera record state data is imported to MATLAB and the time, acoustic signal, and camera record state signal are extracted from the data. To align the acoustic signal with the high-speed camera images, the acoustic and camera record state signals are first plotted together as a function of time. The acoustic signal is then cropped so that it begins immediately after the camera record state switches from low to high (0 to 5 V) and ends immediately before the camera record state switches back to low (5 to 0 V). The impact, deep seal, and final full cavity times are found from the synchronized images. The time is offset by the impact time so that impact occurs at $t = 0$ for each case. For the waveforms presented in the results, the acoustic signal is cropped from 20 ms before impact to the last frame that the cavity is fully in view and three trials are averaged together for each case. Three trials are used to ensure the results are repeatable and consistent.

For the spectrograms presented in the results, the averaged acoustic signal for each case is used and the signal is further cropped, from -10 to 240 ms, so that the number of points used in the fft is 0.25% of the sampling frequency. The spectrograms are created with the MATLAB spectrogram function. The data is sectioned using a Hanning window with a window size of 1024 samples and an overlap of 575 samples. The window size is selected to provide a balance between the frequency resolution and time resolution. The

frequency resolution and time resolution are calculated using (4.1) and (4.2), respectively, where F_s is the sampling frequency and N is the number of samples per window.

$$f_{res} = F_s/N \tag{4.1}$$

$$t_{res} = N/F_s \tag{4.2}$$

For a sampling frequency of 44100 Hz and a window size of 1024, the frequency resolution is 43.1 Hz and the time resolution is 23.2 ms. The overlap is selected to improve both the frequency and time resolution. The frequency for the spectrogram is cropped at 100 Hz as higher frequencies provide no useful information.

4.2   Results and Discussion

The purpose of the acoustic study is to compare the acoustic signals of deflating cavities to the acoustic signals of non-deflating cavities to determine if cavity deflation affects water entry acoustics. Five vented tube cases that resulted in deflation are selected for this study based on the results of the cavity area study. The five vented tube cases are: $L = 7.62$ cm, $A_r = 1$; $L = 11.43$ cm, $A_r = 1$; $L = 15.24$ cm, $A_r = 1$; $L = 15.24$ cm, $A_r = 0.5$; and $L = 15.24$, $A_r = 2$. Each vented tube case is compared against a sphere only case with the same impact velocity. The middle impact velocity of $U_o = 2.6$ m/s is selected for this study as it is the average impact velocity out of the three tested in the cavity area study. The acoustic results first compare the three vented tube length cases and then compare the three area ratio cases.

The image sequences for three vented tube length cases ($L = 7.62$ cm, $A_r = 1$; $L = 11.43$ cm, $A_r = 1$; $L = 15.24$ cm, $A_r = 1$) are seen in Fig. 4.1(a)-(c). For each case the vented tube diameter is $d = 1.27$ cm. From the image sequences (Fig. 4.1(a)-(c)) the trends described in the cavity area study for vented tube length are observed: as the vented tube length increases the amount of cavity deflation increases as seen in frame 2 of the image sequences; the $L = 7.62$ cm vented tube case has a significant cavity remaining at the end
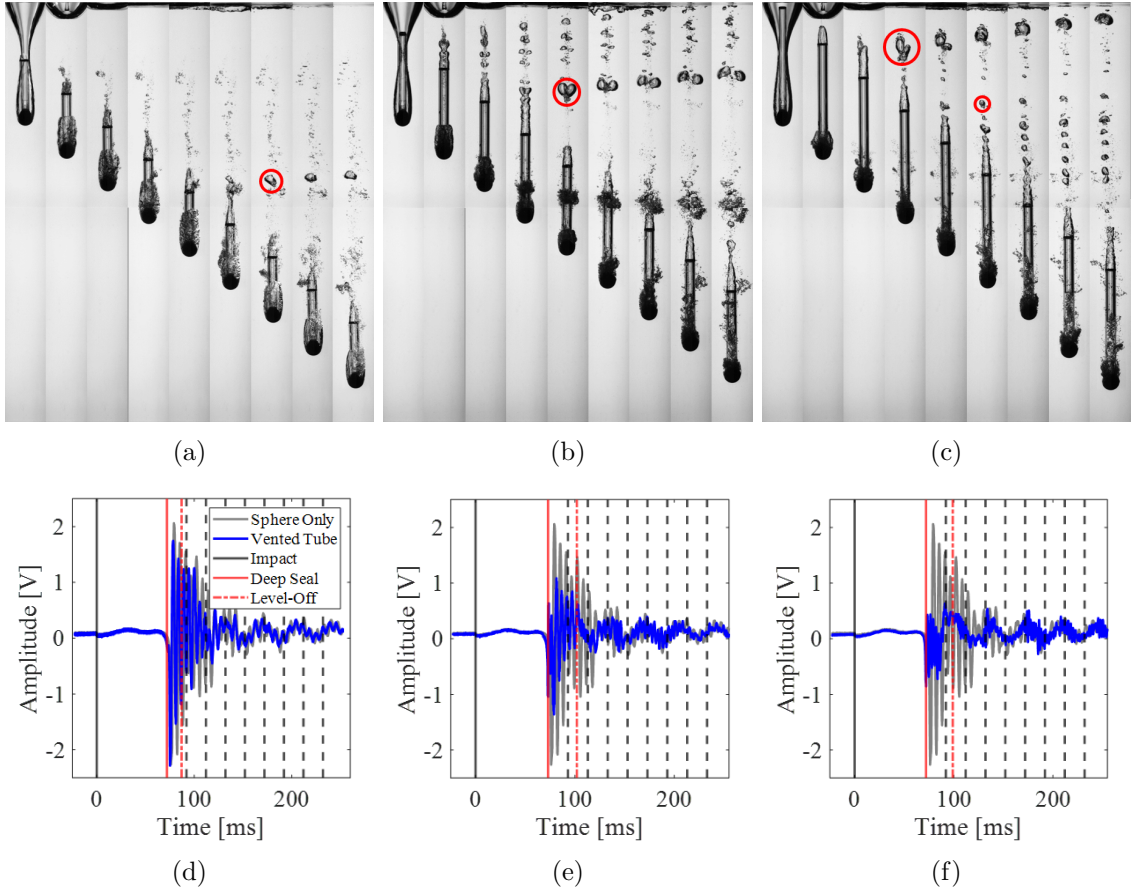
Fig. 4.1: Image sequences and acoustic waveforms for for three vented tube length cases. (a) Image sequence and (d) acoustic waveform for $L = 7.62$ cm vented tube case. (b) Image sequence and (e) acoustic waveform for $L = 11.43$ cm vented tube case. (c) Image sequence and (f) acoustic waveform for $L = 15.24$ cm vented tube case. For the waveforms, the sphere only case acoustic waveform is plotted in gray in the background. For all cases the impact velocity is $U_o = 2.6$ m/s, the sphere diameter is $D = 2.54$ cm, the contact angle is $\theta = 117°$, the vented tube diameter is $d = 1.27$ cm, and the area ratio is $A_r = 1$. For all three image sequences the time starts at deep seal and the time between frames is $\Delta t = 20$ ms. The red circles in the image sequences highlight air bubbles released from the top of the vented tubes. The solid red line in the waveforms corresponds with the first frame of the image sequences and the vertical dashed lines in the waveforms correspond with frames $2 - 9$ of the image sequences.

of the time frame while the $L = 11.43$ cm and $L = 15.24$ cm vented tube cases shed most of

the cavity remaining after deflation as seen in frames $3 - 9$ of the image sequences; once the

cavity reaches the vent holes for the $L = 11.43$ cm and $L = 15.24$ cm vented tube cases, the

vented tube begins to fill with water. The acoustic waveform for each vented tube length

case is presented in Fig. 4.1(d)-(f) with the sphere only case waveform presented in gray in the background. From the waveforms it is immediately noticeable that the sound after deep seal is reduced for the deflating vented tube cases compared to the non-deflating sphere only case and that as the amount of deflation increases, the reduction in sound increases, both in terms of amplitude and time. Two additional observations from the waveforms is that the frequency of the oscillations immediately after deep seal for the $L = 15.24$ cm vented tube case increase compared to the sphere only case and the frequency of the low amplitude oscillations for the $L = 11.43$ cm and $L = 15.24$ cm vented tube cases increase compared to the sphere only case. The amplitude of the low amplitude oscillations also increase for the $L = 11.43$ cm and $L = 15.24$ cm vented tube cases compared to the sphere only case.

The image sequences for the three area ratio cases ($L = 15.24$ cm, $A_r = 0.5$; $L = 15.24$ cm, $A_r = 1$; $L = 15.24$, $A_r = 2$) are seen in Fig. 4.2(a)-(c). For each case the vented tube diameter is $d = 1.27$ cm. From the image sequences (Fig. 4.2(a)-(c)) the trends described in the cavity area study for different area ratios are observed: the amount of cavity deflation for the $A_r = 1$ and $A_r = 2$ vented tube cases is similar while the amount of deflation for the $A_r = 0.5$ vented tube case is slightly less; all three area ratio cases shed most of the remaining cavity after deflation; the cavity reaches the vent holes for all three area ratio cases, first for the $A_r = 2$ vented tube case and last for the $A_r = 0.5$ vented tube case; all three vented tubes subsequently fill with water. The acoustic waveforms for each area ratio are presented in Fig. 4.2(d)-(f) with the sphere only waveform presented in gray in the background. The waveforms show that for all three deflating area ratio cases the sound is dramatically reduced compared to the non-deflating sphere only case, in terms of both amplitude and time. The frequencies of the oscillations immediately after deep seal and the low amplitude oscillations for all three area ratio cases are higher compared to the sphere only case. The frequency and amplitude of the low amplitude oscillations increase as the area ratio increases.

More detailed frequency information is presented in the spectrograms in Fig. 4.3 for the sphere only case (Fig. 4.3(b)), the vented tube length cases (Fig. 4.3(c)-(e)), and the
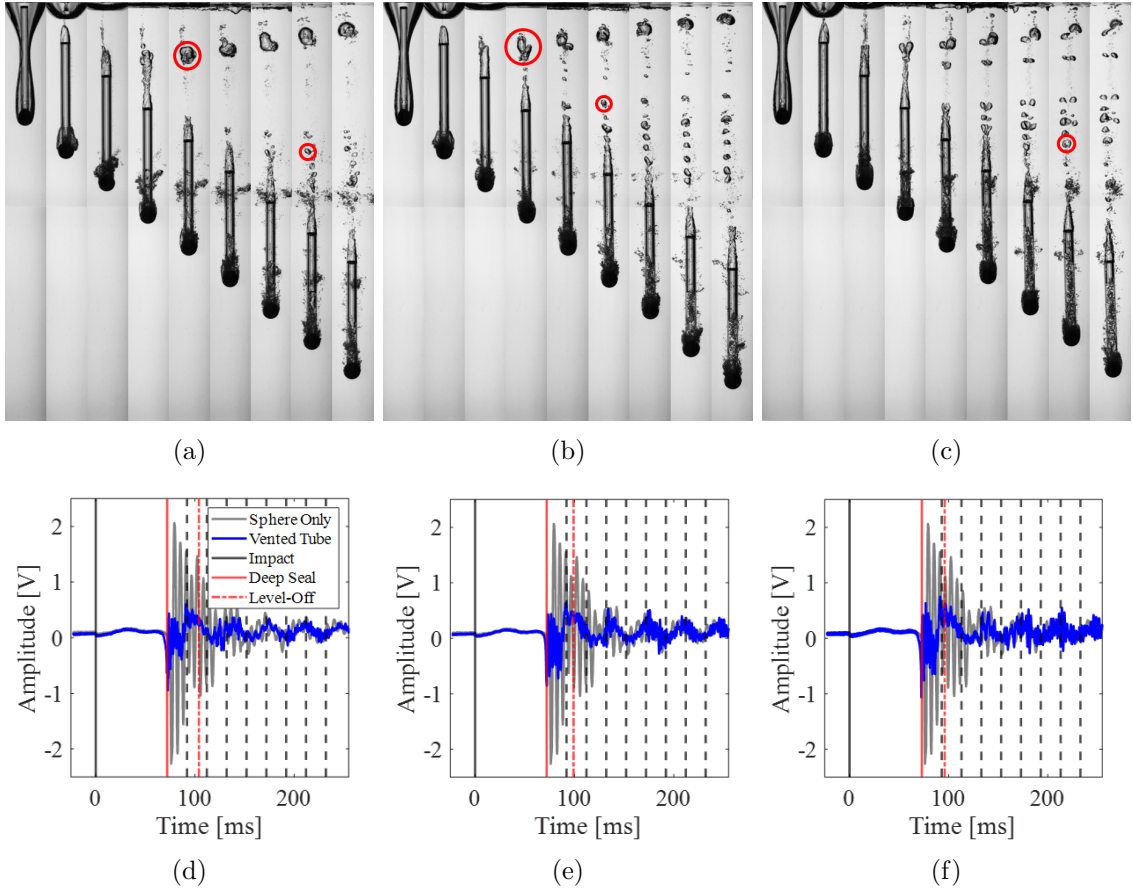
Fig. 4.2: Image sequences and acoustic waveforms for three area ratio cases. (a) Image sequence and (d) acoustic waveform for $A_r = 0.5$ cm vented tube case. (b) Image sequence and (e) acoustic waveform for $A_r = 1$ cm vented tube case. (c) Image sequence and (f) acoustic waveform for $A_r = 2$ cm vented tube case. For the waveforms, the sphere only case acoustic waveform is plotted in gray in the background. For all cases the impact velocity is $U_o = 2.6$ m/s, the sphere diameter is $D = 2.54$ cm, the contact angle is $\theta = 117°$, the vented tube diameter is $d = 1.27$ cm, and the vented tube length is $L = 15.24$ cm. For all three image sequences the time starts at deep seal and the time between frames is $\Delta t = 20$ ms. The red circles in the image sequences highlight air bubbles released from the top of the vented tubes. The solid red line in the waveforms corresponds with the first frame of the image sequences and the vertical dashed lines in the waveforms correspond with frames $2 - 9$ of the image sequences.

area ratio cases (Fig. 4.3(f)-(h)). For the sphere only case (Fig. 4.3(b)) the dominate frequencies, including the Minnaert frequency of 172 Hz found in Section 2.4.1, are between 100 Hz and 200 Hz and the intensity is strongest for the first 50 ms after deep seal. For the vented tube length cases (Fig. 4.3(c)-(e)), both the magnitude and period of intensity after

(a)

(b) Sphere Only

(c) Tube Length: $L = 7.62$ cm (d) Tube Length: $L = 11.43$ cm (e) Tube Length: $L = 15.24$ cm

(f) Area Ratio: $A_r = 0.5$ (g) Area Ratio: $A_r = 1$ (h) Area Ratio: $A_r = 2$
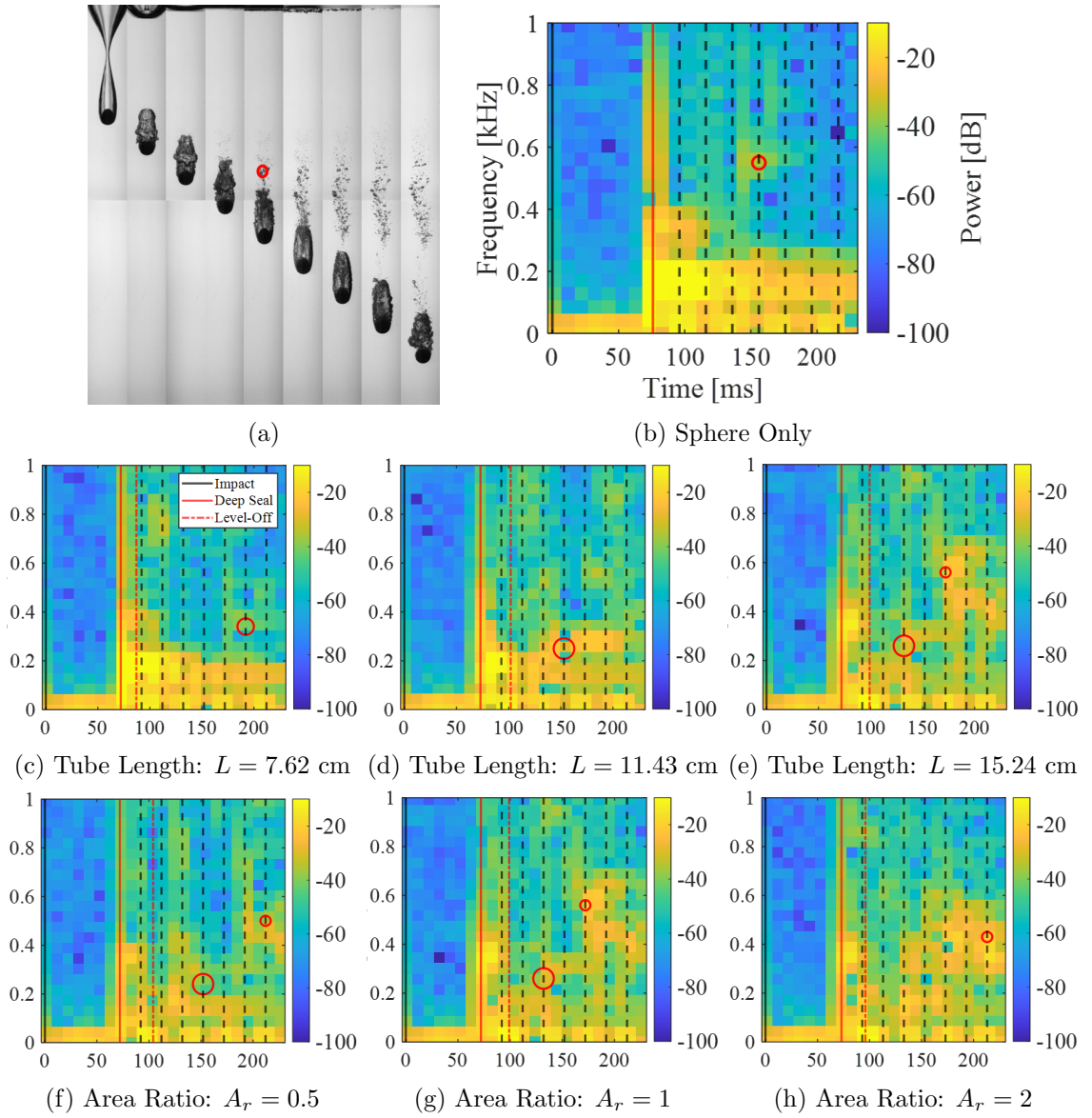
Fig. 4.3: (a) sphere only case image sequence and spectrograms for (b) sphere only case, three vented tube length cases: (c) $L = 7.62$ cm, (d) $L = 11.43$ cm, (e) $L = 15.24$ cm, and three area ratio cases: (f) $A_r = 0.5$, (g) $A_r = 1$, (h) $A_r = 2$. For all cases the impact velocity is $U_o = 2.6$ m/s, the sphere diameter is $D = 2.54$ cm, the contact angle is $\theta = 117°$. For all vented tube length cases the the vented tube diameter is $d = 1.27$ cm and the area ratio is $A_r = 1$. For all area ratio cases the the vented tube diameter is $d = 1.27$ cm and the vented tube length is $L = 15.24$ cm. For the image sequence the time starts at deep seal and the time between frames is $\Delta t = 20$ ms. The red circle in the sphere only case image sequence highlights an air bubble released from the cavity. The solid red line in the spectrograms corresponds with the first frame of the image sequences and the vertical dashed lines in the spectrograms correspond with frames $2 - 9$ of the image sequences in (a), Fig. 4.1(a)-(c), and Fig. 4.2(a)-(c).

deep seal at low frequencies decrease as the amount of deflation increases and compared to the sphere only case which is consistent with the vented tube length waveform observations. For all three area ratio cases (Fig. 4.3(f)-(h)), the magnitude and time period of the intensity after deep seal at low frequencies are greatly reduced compared to the sphere only case which is consistent with the area ratio waveform observations. As the projectiles continue to descend, the magnitude at higher frequencies, between 200 Hz and 800 Hz, increases compared to the sphere only case both as the vented tube length increases and as the area ratio increases. This increase in noise at higher frequencies corresponds with the time period of the low amplitude oscillations in both the vented tube length and area ratio waveforms.

The increase in magnitude, or sound, at higher frequencies is caused by the release of air bubbles from the top of the vented tube. One or two air bubbles are selected for each of the cases, highlighted by a red circle in the image sequences (Fig. 4.1(a)-(c), Fig. 4.2(a)-(c), Fig. 4.3(a)), and the volume is estimated in MATLAB image processing and used to estimate the air bubble radius assuming the volume is a sphere. The estimated air bubble radius is then used to calculate the Minnaert frequency for the bubble using equation 2.1. The Minnaert frequency for each bubble is marked with a red circle in the spectrograms (Fig. 4.3(b)-(h)), on the dashed line of the corresponding image frame. The red circles show that the times and frequencies of the air bubbles correspond to an increase in sound. The difference in the sound at higher frequencies is due to a difference in the release of air bubbles between cases as observed in the image sequences. For all of the vented tube cases (Fig. 4.1(a)-(c), Fig. 4.2(a)-(c)), a large air bubble is released followed by consecutive smaller bubbles, similar to the air-bubble shedding described by Zhang, et al. [14]. The time that the larger bubble is released and the size and number of consecutive smaller bubbles increases as the vented tube length increases (Fig. 4.1(a)-(c)). The number and size of the consecutive smaller bubbles also increases as the area ratio increases for the $L = 15.24$ cm vented tube length (Fig. 4.2(a)-(c)). For the sphere only case, there is no vented tube to release bubbles but the cavity releases a cloud of small air bubbles between 60 ms and 100 ms after deep seal, as it sheds. Most of the air bubbles are small enough that the

frequency is above 1 kHz but there are a few with frequencies below 1 kHz that show up in the spectrogram.

The difference between the sphere only case and the five vented tube cases are highlighted in the spectrograms in Fig. 4.4. For each vented tube case, the spectrogram is subtracted from the sphere only case spectrogram. The more teal there is, which represents 0 dB change, the more similar the vented tube case and sphere only case acoustic signals are. Power above 0 dB means that the sound is reduced for the vented tube case while power below 0 dB means that the sound is stronger for the vented tube case. The $L = 7.62$ cm, $A_r = 1$ vented tube case acoustic signal (Fig. 4.4(a)) is most similar to the sphere only acoustic signal which is expected as there is minimal deflation and a majority of the cavity persists as the sphere descends, similar to the sphere only case. As the vented tube length increases the sound after deep seal is reduced for the vented tube cases at frequencies below 200 Hz. A change in area ratio between $A_r = 0.5$ and $A_r = 2$ does not have a significant impact on the sounds at low frequencies. From frame 2 of the vented tube image sequences (Fig. 4.1(a)-(c), Fig. 4.2(a)-(c)) it is observed that there is a definite increase in deflation as the vented tube length increases but as the area ratio increases the cavity deflation is relatively similar which indicates that deflation affects the sound produced at low frequencies and as deflation increases the sound decreases. When the vented tubes release air bubbles, starting around 50 ms after deep seal, the sound increases at frequencies above 200 Hz and as the size and number of air bubbles released increase, the stronger the sound becomes.

For applications where noise reduction is important to remain undetected, low frequency sounds are more of a concern than high frequency sounds. High frequency sounds have greater attenuation than low frequency sounds and dampen out sooner to background noise, while low frequency sounds persist longer. Therefore, for objects that need to remain undetected after water entry, it is necessary to reduce low frequency sounds. The results of this acoustic study show that the deflation of air cavities that form around objects entering water dramatically reduces the magnitude of low frequency sounds after deep seal compared to a non-deflating cavity. Based on these results, cavity deflation facilitated by a vented
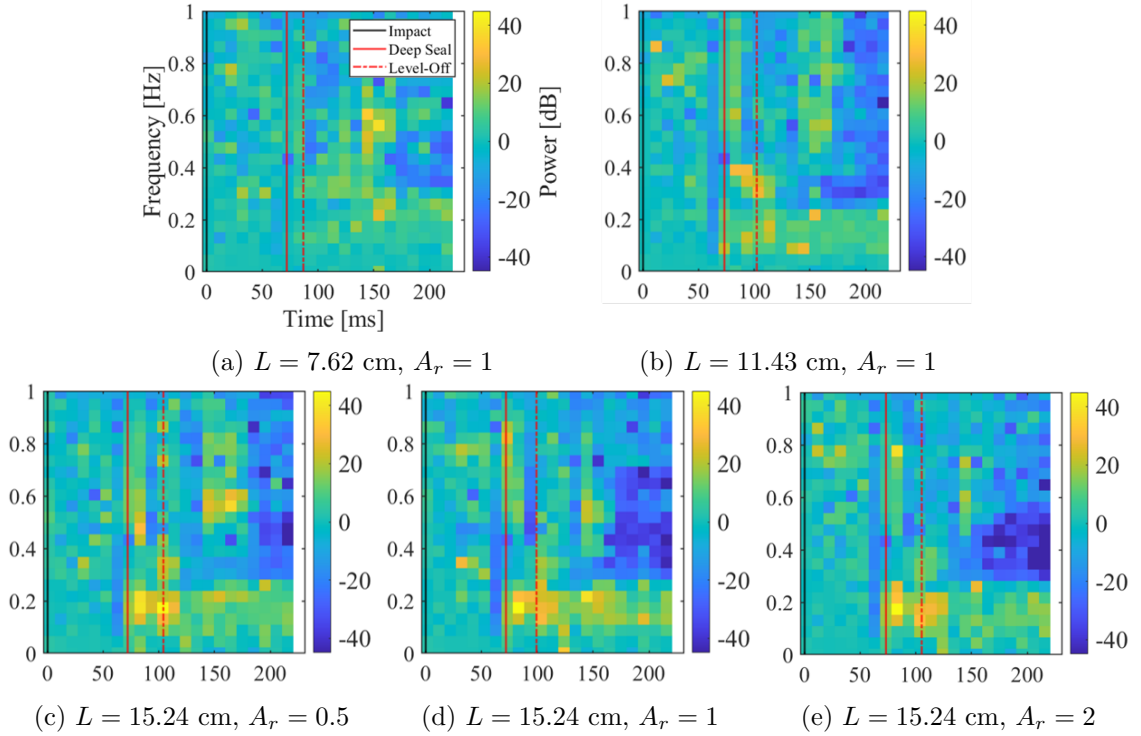
Fig. 4.4: Vented tube case spectrogram subtracted from sphere only case spectrogram for five vented tube cases. For all cases the impact velocity is $U_o = 2.6$ m/s, the sphere diameter is $D = 2.54$ cm, and the contact angle is $\theta = 117°$. For all vented tube cases the vented tube diameter is $d = 1.27$ cm.

system is a viable option for cavity noise reduction and could have practical applications for quieting objects such as UAVs and high-speed torpedoes after water entry.

The acoustic trends discussed above are summarized in Fig. 4.5 which presents the root mean square of the normalized amplitude (from -1 to 1) for the sphere only case and all five vented tube cases. The sound after deep seal is reduced for the deflating vented tube cases compared to the non-deflating sphere only case and, in general, as deflation increases sound is further reduced. At higher area ratios the overall sound starts to increase slightly which is due to an increase in sound at higher frequencies caused by air bubbles released from the top of the vented tube. The increase in sound caused by the release of air bubbles is small compared to the decrease in sound due to deflation but for cases where the signal amplitude is greatly reduced after deep seal, small changes later in the signal have a greater

effect on the overall signal. The reduction in sound for deflating cavities, particularly at low frequencies, highlights a potential application for a vented system to deflate cavities.
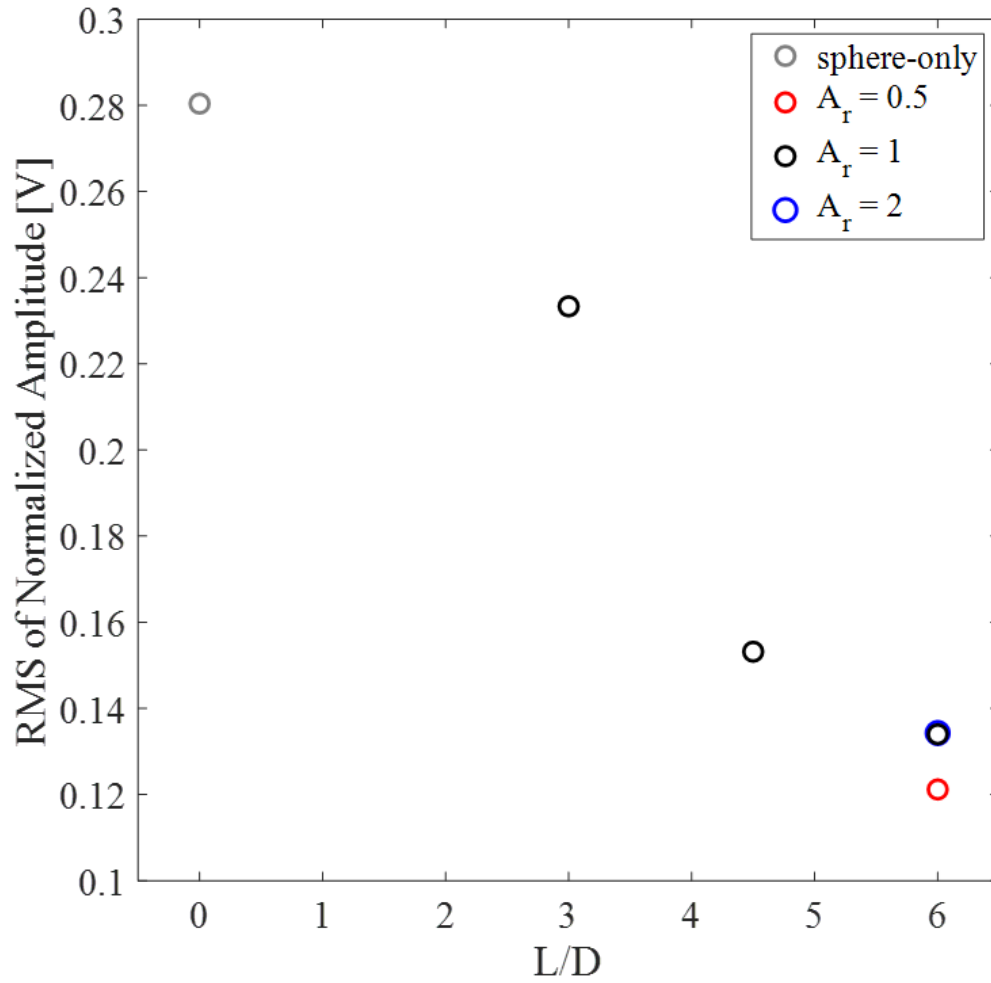
Fig. 4.5: RMS value of normalized acoustic signal amplitude for the six acoustic cases tested. For all cases the impact velocity is $U_o = 2.6$ m/s, the sphere diameter is $D = 2.54$ cm, and the contact angle is $\theta = 117°$. For all vented tube cases the vented tube diameter is $d = 1.27$ cm.

CHAPTER 5

ACCELERATION STUDY

This chapter presents the data processing methods and results for the acceleration study. The parameters for this study are presented in table 2.1. For all cases presented in this chapter the sphere diameter is $D = 5$ cm, the contact angle is $\theta = 141°$ and the impact velocity is $U_o = 2.6$ m/s.

5.1 Data Processing

This section describes the methods used to process the accelerometer data. The accelerometer data is imported into MATLAB and the time and x-, y-, and z- axis acceleration are extracted from the data. The total acceleration is calculated by taking the root sum of the squared acceleration values in each direction for each time step. The sign of the total acceleration is determined by multiplying the total acceleration by the sign of the z-axis acceleration value. To compare the acceleration data between cases it is necessary to offset the time so that impact occurs at $t = 0$ ms and remove the zero-offset bias so that the acceleration during free fall is 0 g. The total acceleration is plotted as a function of time and the plot is used to manually find the free fall and impact times. Free fall starts when the acceleration suddenly switches from 1 g to 0 g and continues until impact when the acceleration suddenly increases from 0 g. To offset the time so impact occurs at $t = 0$ ms, impact is subtracted from the time. To remove the zero-offset bias, the acceleration during free fall is averaged and subtracted from the total acceleration.

Three trials were conducted for each case and a plot of three trials for a sphere only case and a plot of three trials for a vented tube case are seen in Fig. 5.1(a) and Fig. 5.1(b), respectively. For the vented tube case the vented tube diameter is $d = 1.27$ cm, the vented tube length is $L = 15.24$ cm, and the area ratio is $A_r = 1$. Fig. 5.1 shows that the acceleration data is fairly consistent and repeatable between the trials for both the sphere
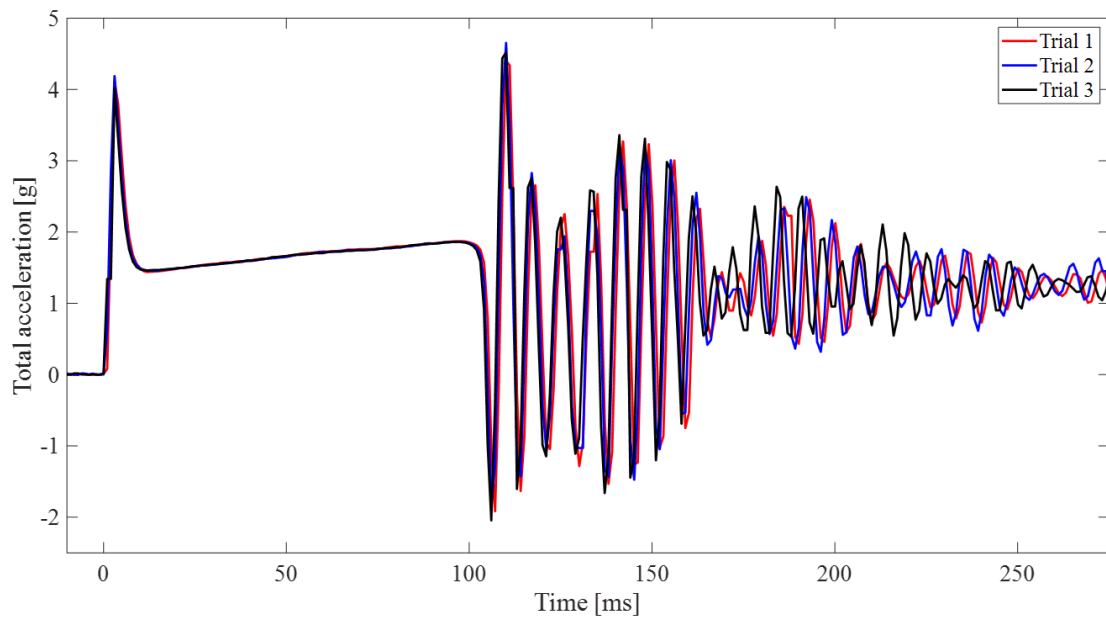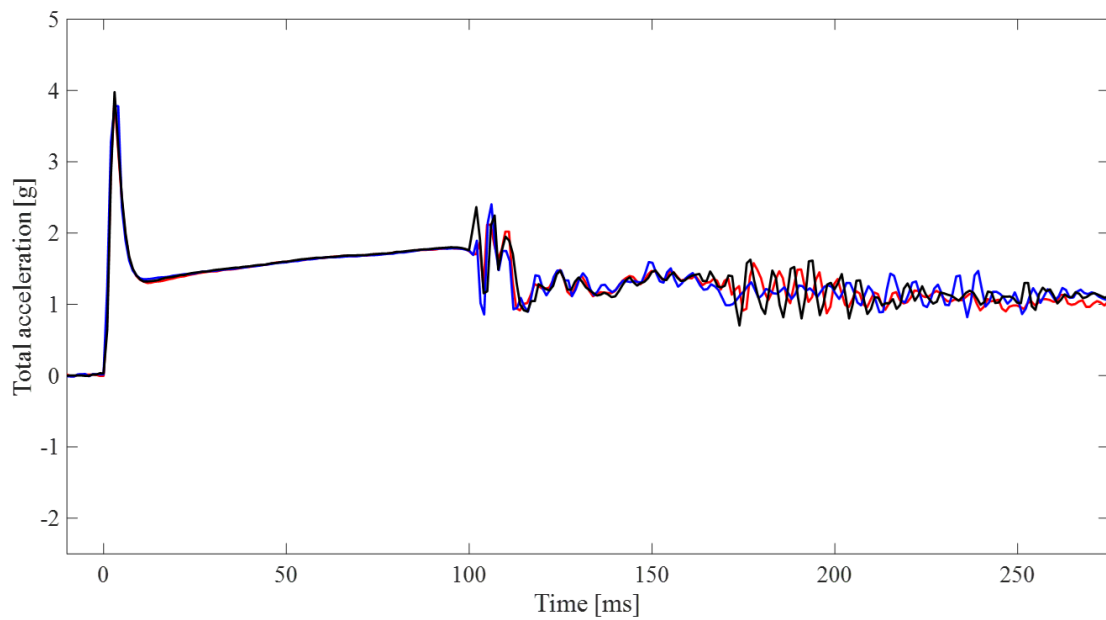
Fig. 5.1: Acceleration plots highlighting the repeatably for three trials for (a) a single sphere only case and (b) a single vented tube case. For both cases the impact velocity is $U_o = 2.6$ m/s, the sphere diameter is $D = 5$ cm, and the contact angle is $\theta = 141°$. For the vented tube case the vented tube diameter is $d = 1.27$ cm, the vented tube length is $L = 15.24$ cm, and the area ratio is $A_r = 1$.

only and vented tube cases. While the trials are consistent and repeatable, only one trial is presented in the results to avoid averaging out any important acceleration peaks.

5.2   Results and Discussion

The purpose of the acceleration study is to compare the acceleration profiles of deflating cavities to the acceleration profiles of non-deflating cavities to determine if cavity deflation can be detected in acceleration data. The same five vented tube cases ($L = 7.62$ cm, $A_r = 1$; $L = 11.43$ cm, $A_r = 1$; $L = 15.24$ cm, $A_r = 1$; $L = 15.24$ cm, $A_r = 0.5$; and $L = 15.24$, $A_r = 2$) and impact velocity ($U_o = 2.6$ m/s) selected for the acoustic study are used for the acceleration study. A $L = 15.24$ cm non-vented tube (tube with no radial holes), is also tested to see how the presence of a tube impacts acceleration.

Fig. 5.2 presents the image sequences for the sphere only case (Fig. 5.2(a)), the $L = 15.24$ cm non-vented tube case (Fig. 5.2(b)), and the $L = 15.24$ cm, $A_r = 1$ vented tube case (Fig. 5.2(c)). Fig. 5.3 presents the corresponding cavity area and acceleration plots. The cavities formed for the $D = 5$ cm sphere diameter cases are almost twice the size of the cavities formed for the $D = 2.54$ cm sphere diameter cases, but as the vented tube parameters are the same, the amount of deflation is similar. The larger size of the cavities make it difficult to detect deflation in the image sequences (Fig. 5.2) but the cavity area plot (Fig. 5.3(a)) shows that the $L = 15.24$ cm, $A_r = 1$ vented tube case cavity does deflate. The cavities for the sphere only and non-vented tube cases do not deflate as expected as neither provides the air in the cavity a means to escape. The acceleration plot (Fig. 5.3(b)) shows that for all three cases the acceleration oscillates after deep seal. Bodily, et al. [12] and Louf et al. [32] both showed that oscillations in force data after pinch-off are induced by the formation of cavity ripples caused by cavity volume pressure oscillations [11].

Fig. 5.3(b) shows that the amplitude of the sphere only case oscillations are the highest. The oscillation amplitude for the $L = 15.24$ cm non-vented tube case is somewhat reduced compared to the sphere only case which indicates that the presence of the tube impacts the cavity volume oscillations, potentially acting as a fence to reduce the pressure perturbations. The oscillation amplitude is further, and dramatically, reduced for the $L = 15.24$ cm, $A_r = 1$
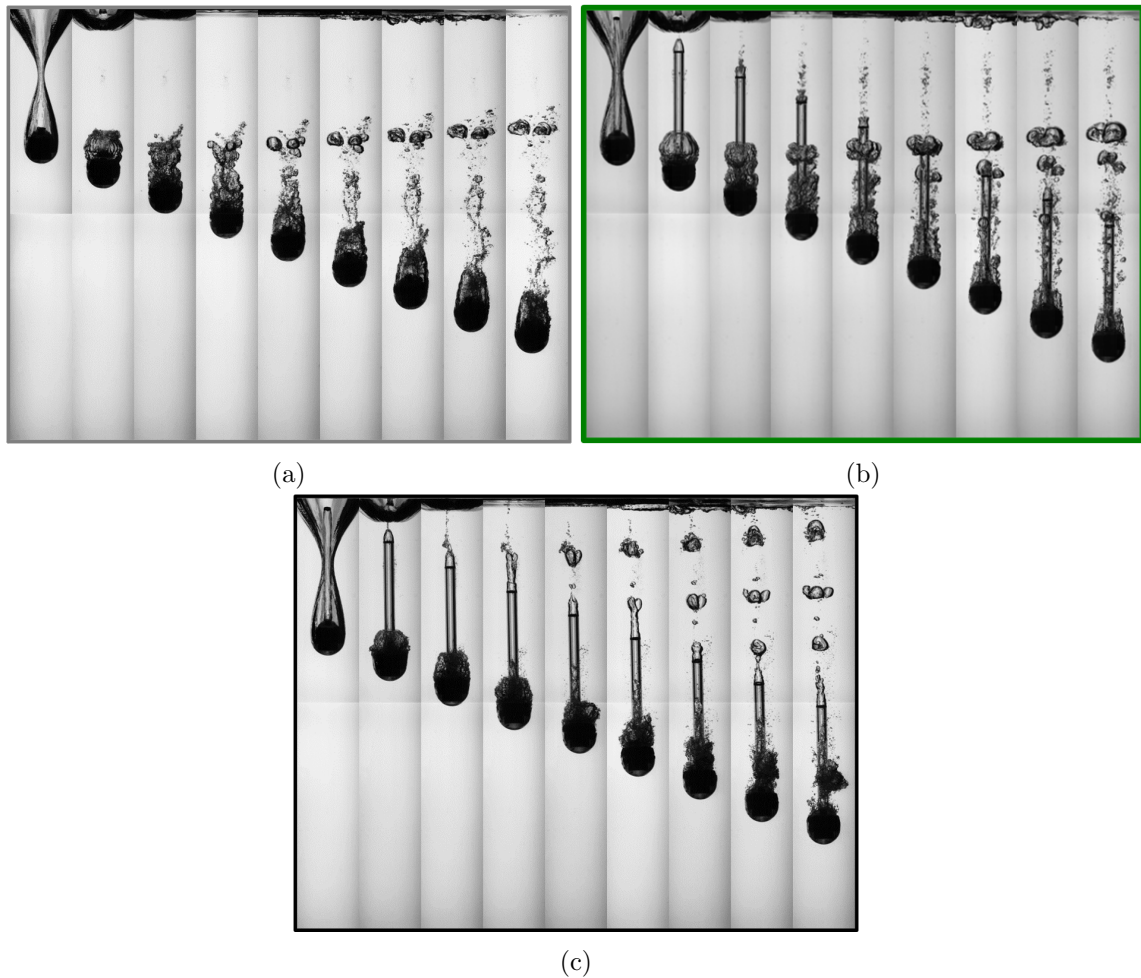
Fig. 5.2: Image sequences for acceleration cases comparing (a) sphere only case, (b) $L = 15.24$ cm non-vented tube case, and (c) $L = 15.24$ cm, $A_r = 1$ vented tube case. For all cases the impact velocity is $U_o = 2.6$ m/s, the sphere diameter is $D = 5$ cm, and the contact angle is $\theta = 141°$. For all tube cases the tube diameter is $d = 1.27$ cm. For all four image sequences the time starts at deep seal and the time between frames is $\Delta t = 20$ ms.

vented tube case. It is seen in frames 2 and 3 of the image sequences that the cavity ripples for the $L = 15.24$ cm, $A_r = 1$ vented tube case (Fig. 5.2(a)) are much smaller than ripples for the sphere only case (Fig. 5.2(b)) and the $L = 15.24$ cm non-vented tube case (Fig. 5.2(c)). This indicates that deflation suppresses cavity oscillations by allowing the air to move out of the cavity instead of compressing. By allowing air to move out of the way, vortex shedding, which induces drag [29], is likely also reduced. Particle image velocimetry (PIV) could be conducted to verify how cavity deflation impacts vortex shedding.
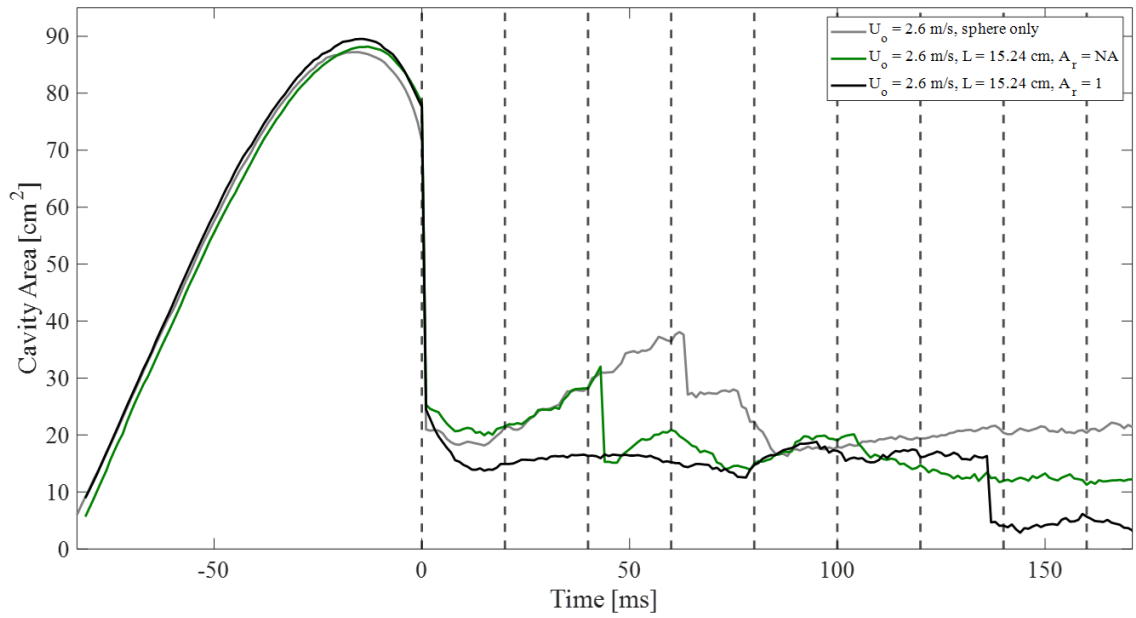
(a)
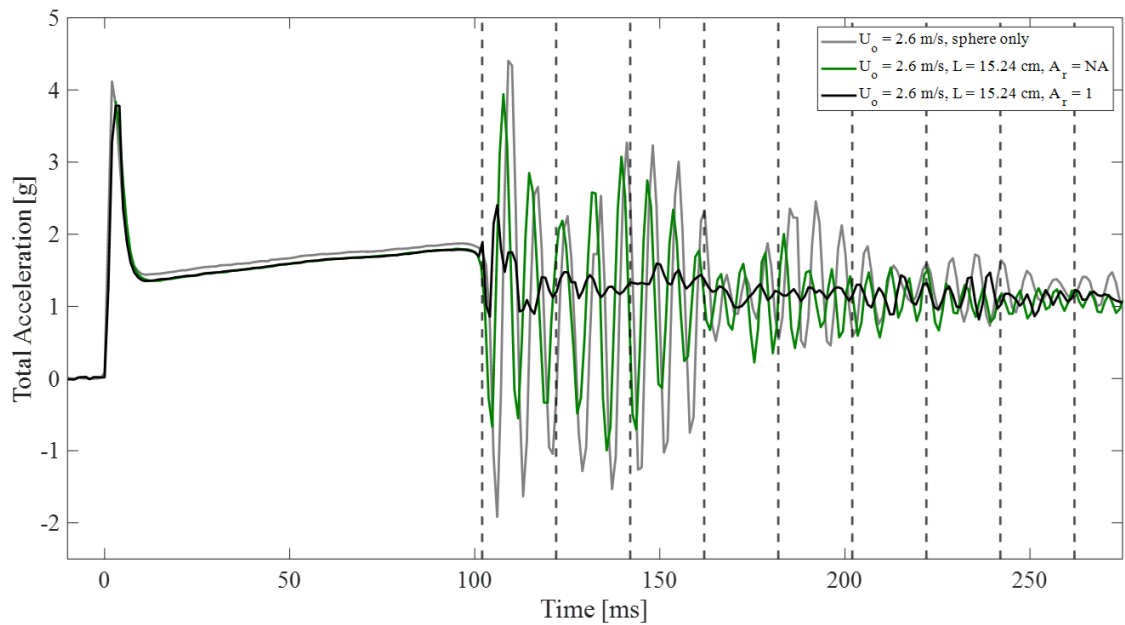
(b)

Fig. 5.3: (a) Cavity area plot and (b) acceleration plot comparing sphere only case, $L = 15.24$ cm non-vented tube case, and $L = 15.24$ cm, $A_r = 1$ vented tube case. For all cases the impact velocity is $U_o = 2.6$ m/s, the sphere diameter is $D = 5$ cm, and the contact angle is $\theta = 141°$. For all tube cases the tube diameter is $d = 1.27$ cm. The vertical dashed lines correspond with each frame of the image sequences in Fig. 5.2

Image sequences, cavity area profiles, and acceleration profiles are presented in Fig. 5.4, Fig. 5.5(a), and Fig. 5.5(b), respectively, for the sphere only case and the three vented tube length cases ($L = 7.62$ cm, $A_r = 1$; $L = 11.43$ cm, $A_r = 1$; $L = 15.24$, $A_r = 1$). The cavity area and acceleration profiles for the $L = 15.24$ cm non-vented tube case are also presented in Fig. 5.5. For all tube cases the tube diameter is $d = 1.27$ cm. The cavity area plot and inset deflation plot (Fig. 5.5(a)) show that as the vented tube length increases the amount of deflation increases with both the $L = 11.43$ cm and $L = 7.62$ cm vented tube cases deflating less than the $L = 15.24$ vented tube case. Comparing the corresponding vented tube case acceleration profiles (Fig. 5.5(b)), as the amount of deflation increases, the amplitude of the acceleration oscillations decreases. Differences in the cavity ripples are seen for the three vented tube cases, in frames 2 and 3 of the image sequences. For the $L = 7.62$ cm vented tube case (Fig. 5.4(b)), which deflates the least, large cavity ripples are seen but for the $L = 11.43$ and $L = 15.24$ vented tube cases (Fig. 5.4(c)-(d)), the ripples are much smaller

Image sequences, cavity area profiles, and acceleration profiles are presented in Fig. 5.6, Fig. 5.7(a), and Fig. 5.7(b), respectively, for the sphere only case and the three area ratio cases ($L = 15.24$ cm, $A_r = 0.5$; $L = 15.24$ cm, $A_r = 1$; $L = 15.24$, $A_r = 2$). The cavity area and acceleration profiles for the $L = 15.24$ cm non-vented tube case are also presented in Fig. 5.7. For all tube cases the tube diameter is $d = 1.27$ cm. The cavity area plot and inset deflation plot (Fig. 5.7(a)) show that all three area ratio cases deflate and the amount of deflation for the $A_r = 0.5$ and $A_r = 2$ vented tube cases is similar to and greater than the amount of deflation for the $A_r = 1$ vented tube case, respectively. The corresponding vented tube acceleration profiles (Fig. 5.7(b)) show that the amplitude of the acceleration oscillations is dramatically reduced for the all three area ratio cases. While the amount of deflation is greater for the $A_r = 2$ vented tube case compared to the other two area ratio cases, the amplitude of the acceleration oscillations for the are $A_r = 2$ case is not further reduced. The acceleration peak after deep seal for the $A_r = 2$ vented tube case corresponds to the time that the cavity reaches the vent holes as seen in the inset image in Fig. 5.7(b).
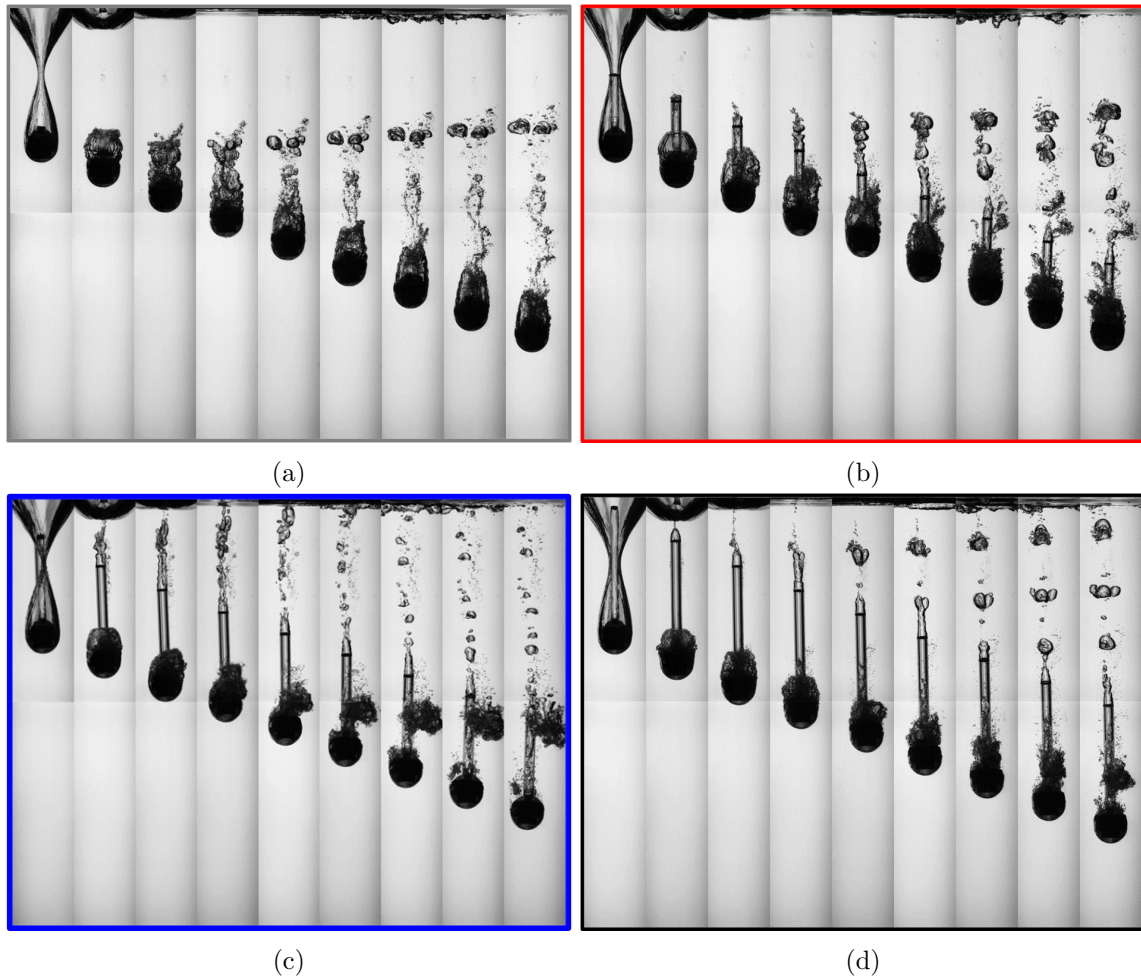
Fig. 5.4: Image sequences for acceleration cases comparing (a) sphere only case and three vented tube length cases: (b) $L = 7.62$ cm, (c) $L = 11.43$ cm, and (d) $L = 15.24$ cm. For all cases the impact velocity is $U_o = 2.6$ m/s, the sphere diameter is $D = 5$ cm, and the contact angle is $\theta = 141°$. For all vented tube cases the vented tube diameter is $d = 1.27$ cm and the area ratio is $A_r = 1$. For all four image sequences the time starts at deep seal and the time between frames is $\Delta t = 20$ ms.

The $A_r = 2$ area ratio case is the only acceleration case tested where the cavity reaches the vent holes before shedding occurs. Frames 2 and 3 of the image sequences for the three area ratio cases (Fig. 5.6(b)-(d)) show that all three cavities have reduced cavity ripples compared to the sphere only case.

The root mean square of the normalized acceleration oscillations after deep seal (from -1 to 1) for the seven acceleration cases tested are presented in Fig. 5.8 which highlights the

(a)

(b)

Fig. 5.5: (a) Cavity area plot and (b) acceleration plot comparing sphere only case, $L = 15.24$ cm non-vented tube case, and three vented tube length cases: $L = 7.62$ cm, $L = 11.43$ cm, and $L = 15.24$ cm. Inset plot in (a) shows the total change in cavity area as function of time during the deflation period for the three deflation cases. For all cases the impact velocity is $U_o = 2.6$ m/s, the sphere diameter is $D = 5$ cm, and the contact angle is $\theta = 141°$. For all tube cases the tube diameter is $d = 1.27$ cm. For all vented tube cases the area ratio is $A_r = 1$. For the acceleration plot, impact occurs at $t = 0$ ms and deep seal occurs at the first dashed line. The vertical dashed lines correspond with each frame of the image sequences in Fig. 5.4

Fig. 5.6: Image sequences for acceleration cases comparing (a) sphere only case and three area ratio cases: b) $A_r = 0.5$, c) $A_r = 1$, d) $A_r = 2$. For all cases the impact velocity is $U_o = 2.6$ m/s, the sphere diameter is $D = 5$ cm, and the contact angle is $\theta = 141°$. For all vented tube cases the vented tube diameter is $d = 1.27$ cm and the vented tube length is $L = 15.24$. For all four image sequences the time starts at deep seal and the time between frames is $\Delta t = 20$ ms.

trends discussed in the previous paragraphs. The amplitude of the acceleration oscillations after deep seal is reduced by the presence of a tube and further reduced for cavities that deflate. In general, as the amount of deflation increases the amplitude of the acceleration oscillations after deep seal decreases. The one exception is the $L = 15.24$ cm, $A_r = 2$ vented tube case which has an acceleration spike that corresponds to when the cavity reaches the vent holes at the end of deflation.
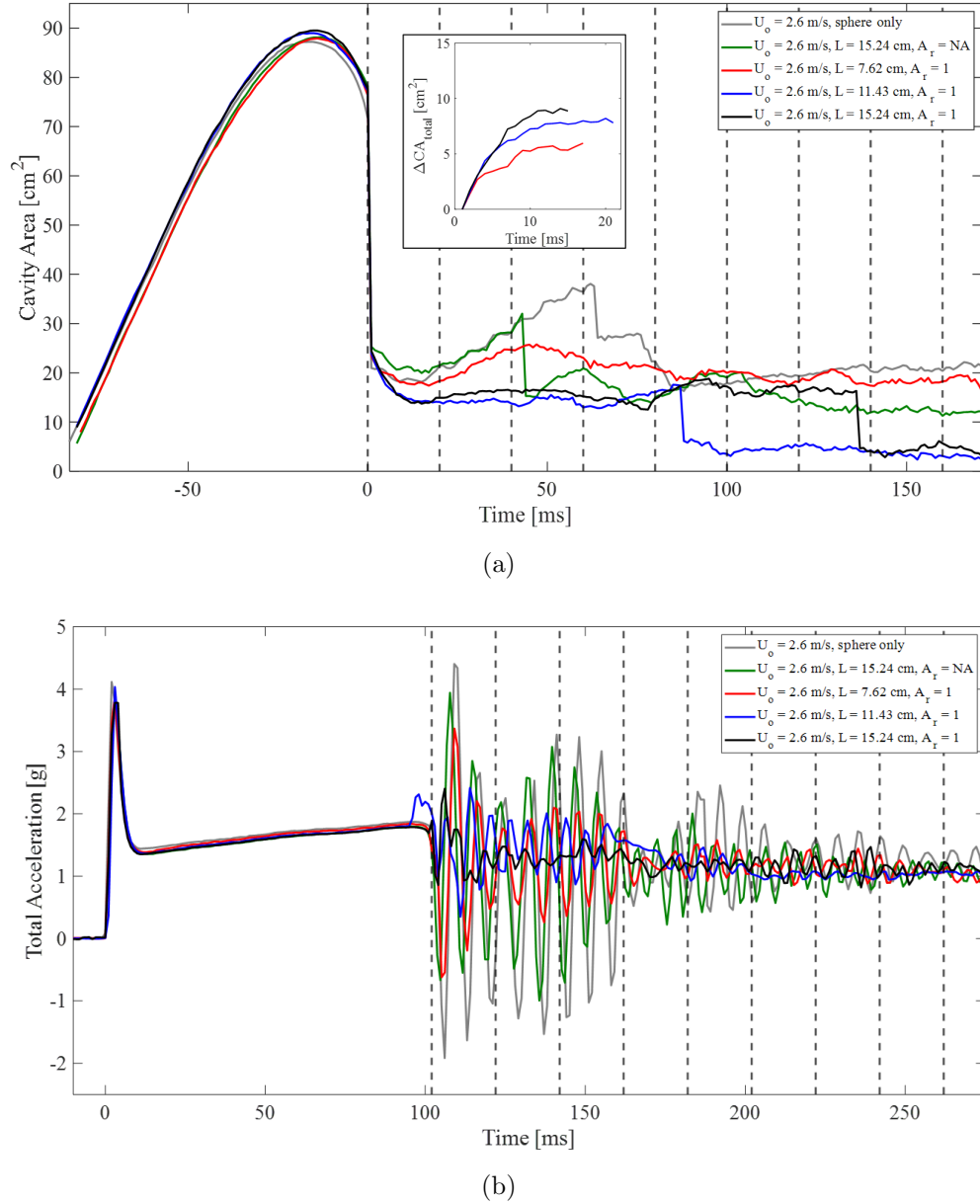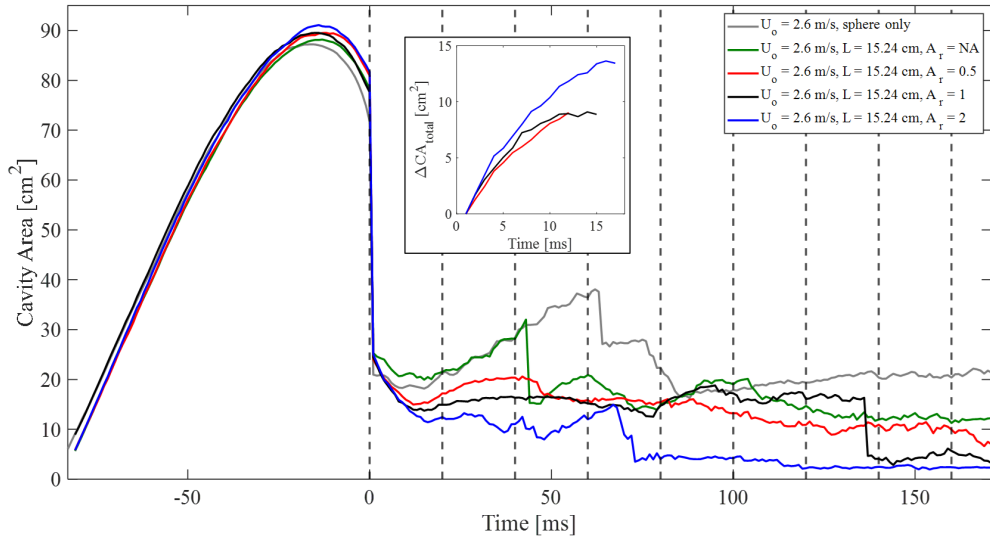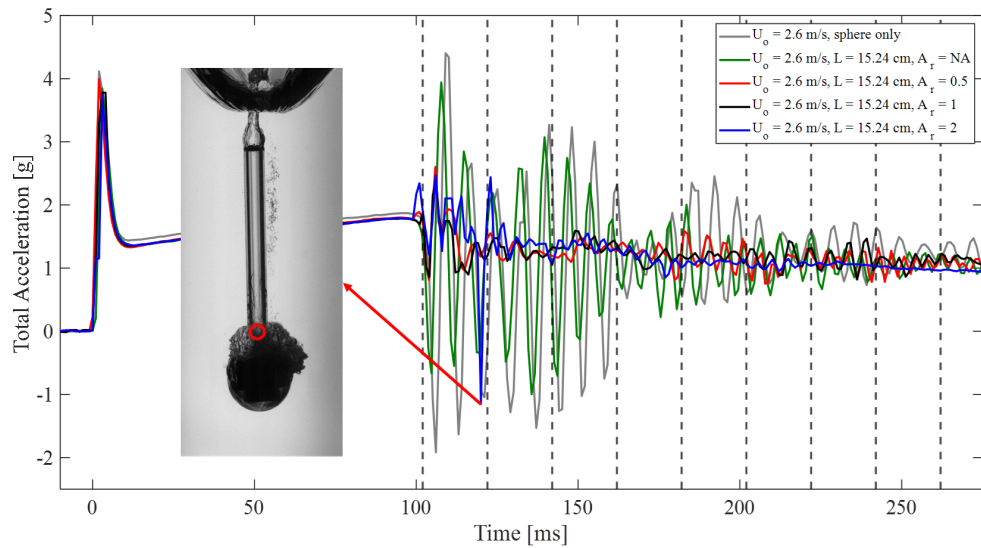
Fig. 5.7: (a) Cavity area plot and (b) acceleration plot comparing sphere only case, $L = 15.24$ cm non-vented tube case, and three area ratio cases: $A_r = 0.5$, $A_r = 1$, and $A_r = 2$. Inset plot in (a) shows the total change in cavity area as function of time during the deflation period for the three deflation cases. Inset image in (b) highlights that the cavity reaches the vent holes at the time peak in the acceleration occurs. For all cases the impact velocity is $U_o = 2.6$ m/s, the sphere diameter is $D = 5$ cm, and the contact angle is $\theta = 141°$. For all tube cases the tube diameter is $d = 1.27$ cm. For all vented tube cases the vented tube length is $L = 15.24$ cm. For the acceleration plot, impact occurs at $t = 0$ ms and deep seal occurs at the first dashed line. The vertical dashed lines correspond with each frame of the image sequences in Fig. 5.6.
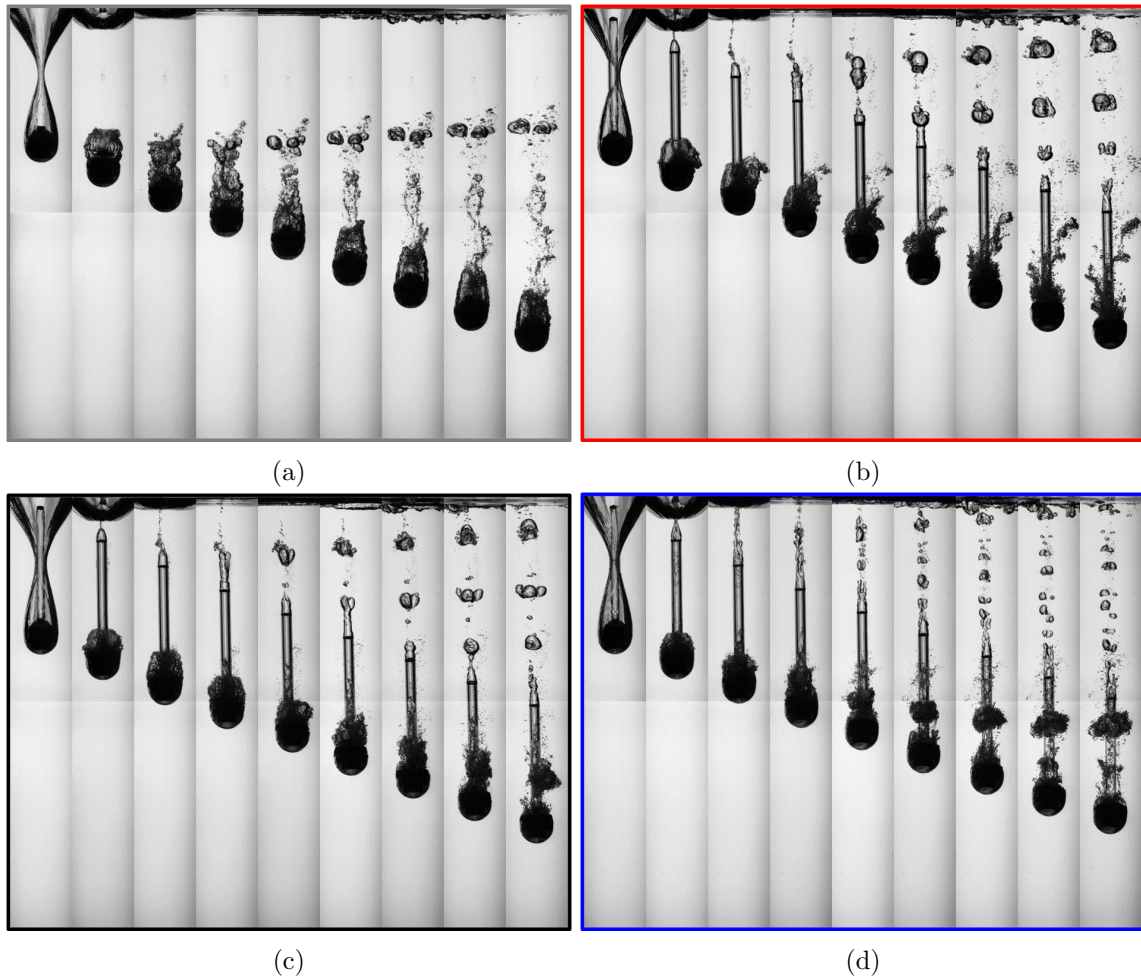
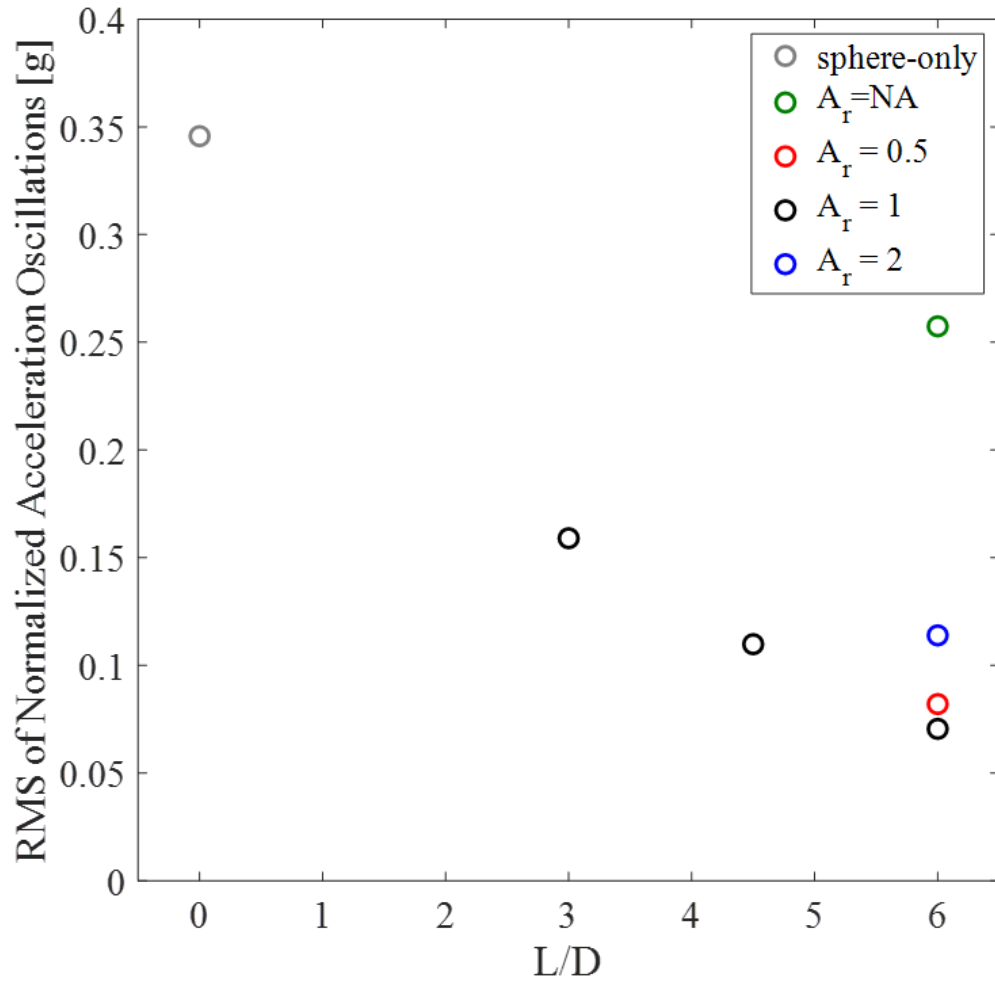Fig. 5.8: RMS value of normalized acceleration after deep seal for the seven acceleration cases tested. For all cases the impact velocity is $U_o = 2.6$ m/s, the sphere diameter is $D = 5$ cm, and the contact angle is $\theta = 141°$. For all tube cases the tube diameter is $d = 1.27$ cm.

CHAPTER 6

CONCLUSION

This thesis presented an introductory study on the dissipation of cavities by means of deflation. A tube with radial vent holes attached to a projectile was designed to facilitate deflation. The radial vent holes are located near the projectile, where the cavity forms, to provide the air in the cavity a means to escape after deep seal pinch-off. Cavities were compared for spherical projectiles without a vented tube and for spherical projectiles with varying vented tube lengths. As long as the vented tube was longer than the lower cavity at deep seal, the air was able to escape through the tube to the free surface and cavity deflation occurred.

To determine what parameters affect cavity deflation, cavity area estimated from high-speed camera images was used to compare the deflation for varying vented tube lengths, vent hole areas, and impact velocities. The amount of deflation increased as vented tube length increased and as vent hole area increased up to a limit. For large vent hole areas the vented tube filled with water before the cavity could fully deflate, trapping the remaining air inside the cavity. The effect of impact velocity on the amount of cavity deflation varied depending on the vented tube length. Deflation for two different vented tube diameters was also compared and the amount of deflation increased as vented tube diameter increased.

An equation for the critical vented tube length required for cavity deflation to occur was developed based on previous studies. The critical vented tube length is a function of impact velocity, sphere radius, and vented tube diameter. The equation can be used when designing a sphere-vented tube device for an application, to select a vented tube length that will be outside of the cavity and allow deflation to occur.

Acoustic signals for deflating and non-deflating cavities were compared. The sound after deep seal was reduced for deflating vented tube cases compared to a non-deflating sphere only case and, in general, as deflation increased the further the sound was reduced.

At higher frequencies the sound increased slightly for the deflating vented tube cases due to the sound produced by bubbles released from the top of the vented tube.

Acceleration profiles for a non-deflating sphere only case, a non-deflating non-vented tube case, and several deflating vented tube cases were compared. The amplitude of the acceleration oscillations after deep seal compared to the sphere only case was reduced by the presence of the non-vented tube and further reduced for the deflating vented tube cases. In general, the amplitude of the acceleration oscillations decreased as the amount of deflation increased.

6.1   Future Work

This study provides a starting point for future cavity deflation studies. As this was an introductory study of cavity deflation facilitated by a vented tube, only a small range of values were selected for each parameter. Future studies could expand upon this work by studying a larger range of values including a larger range of Froude numbers, varying both impact velocity and sphere radius and a larger range of vented tube diameters and area ratios to determine the area ratio limit as a function of vented tube diameter. This study briefly looked at cavity deflation for surface seal but was limited by tank size. A more in-depth surface seal study could be conducted with a deeper tank, including how surface seal cavity deflation impacts acoustics and acceleration. Another direction for future work would be to study cavity deflation for different projectile types including a slender axisymmetric projectile with radial vent holes built into the projectile. Another area of future work would be to use Bernoulli's equation to develop a mathematical approximation for the volumetric deflation rate of the cavity.

REFERENCES

[1] J. M. Aristoff and J. W. M. Bush, "Water entry of small hydrophobic spheres," *Journal of Fluid Mechanics*, vol. 619, pp. 45–78, Jan. 2009.

[2] N. B. Speirs, M. M. Mansoor, J. Belden, and T. T. Truscott, "Water entry of spheres with various contact angles," *Journal of Fluid Mechanics*, vol. 862, Jan. 2019.

[3] V. Duclaux, F. Caillé, C. Duez, C. Ybert, L. Bocquet, and C. Clanet, "Dynamics of transient cavities," *Journal of Fluid Mechanics*, vol. 591, pp. 1–19, 2007.

[4] R. Rabbi, N. B. Speirs, A. Kiyama, J. Belden, and T. T. Truscott, "Impact force reduction by consecutive water entry of spheres," *Journal of Fluid Mechanics*, vol. 915, Mar. 2021.

[5] A. May, "Water entry and the cavity-running behavior of missiles," NAVSEA Hydroballistics Advisory Committee, Tech. Rep., jan 1975.

[6] I. U. Vakarelski, A. Jetly, and S. T. Thoroddsen, "Stable-streamlined cavities following the impact of non-superhydrophobic spheres on water," *Soft Matter*, vol. 15, no. 31, pp. 6278–6287, 2019.

[7] T. T. Truscott, B. P. Epps, and J. Belden, "Water entry of projectiles," *Annual Review of Fluid Mechanics*, vol. 46, no. 1, pp. 355–378, Jan. 2014.

[8] C. Duez, C. Ybert, C. Clanet, and L. Bocquet, "Making a splash with water repellency," *Nature Physics*, vol. 3, no. 3, pp. 180–183, Feb. 2007.

[9] J. M. Aristoff, T. T. Truscott, A. H. Techet, and J. W. M. Bush, "The water entry of decelerating spheres," *Physics of Fluids*, vol. 22, no. 3, p. 032102, Mar. 2010.

[10] A. M. Worthington, *A study of splashes.* Longmans, Green, and Company, 1908. [Online]. Available: https://books.google.com/books?id=LtdUAAAAQAAJ

[11] T. Grumstrup, J. B. Keller, and A. Belmonte, "Cavity ripples observed during the impact of solid objects into liquids," *Physical Review Letters*, vol. 99, no. 11, Sep. 2007.

[12] K. G. Bodily, S. J. Carlson, and T. T. Truscott, "The water entry of slender axisymmetric bodies," *Physics of Fluids*, vol. 26, no. 7, p. 072108, Jul. 2014.

[13] M. M. Mansoor, J. O. Marston, I. U. Vakarelski, and S. T. Thoroddsen, "Water entry without surface seal: Extended cavity formation," *Journal of Fluid Mechanics*, vol. 743, pp. 295–326, Mar. 2014.

[14] Q. Zhang, Z. Zong, T. Z. Sun, Z. Y. Chen, and H. T. Li, "Experimental study of the evolution of water-entry cavity bubbles behind a hydrophobic sphere," *Physics of Fluids*, vol. 32, no. 6, p. 062109, Jun. 2020.

[15] B. D. Uber and R. J. Fegan, "Acoustic signatures accompanying low-velocity water entry," Master's thesis, Naval Postgraduate School, 1973.

[16] R. Rabbi, T. Truscott, J. S. Allen, and J. Belden, "Acoustics of water entry of hydrophobic spheres," *The Journal of the Acoustical Society of America*, vol. 146, pp. 3075–3075, 2019.

[17] M. Shiffman and D. C. Spencer, "The force of impact on a sphere striking a water surface," Courant Institution of Mathematical Sciences, New York University, NY., Tech. Rep. No. AMG-NYU-133., 1945.

[18] M. Moghisi and P. T. Squire, "An experimental investigation of the initial force of impact on a sphere striking a liquid surface," *Journal of Fluid Mechanics*, vol. 108, pp. 133–146, 1981.

[19] F. L. Thompson, "Report no. 290. water-pressure distribution on a seaplane float," National Advisory Committee for Aeronautics, Tech. Rep., 1928.

[20] T. von Von Kármán, "The impact on seaplane floats during landing," National Advisory Committee for Aeronautics, Tech. Rep., 1929. [Online]. Available: https://books.google.com/books?id=9in7nAEACAAJ

[21] J. W. Glasheen and T. A. McMahon, "Vertical water entry of disks at low froude numbers," *Physics of Fluids*, vol. 8, no. 8, pp. 2078–2083, Aug. 1996.

[22] D. Battistin and A. Iafrati, "Hydrodynamic loads during water entry of two-dimensional and axisymmetric bodies," *Journal of Fluids and Structures*, vol. 17, no. 5, pp. 643–664, Apr. 2003.

[23] T. Tveitnes, A. Fairlie-Clarke, and K. Varyani, "An experimental investigation into the constant velocity water entry of wedge-shaped sections," *Ocean Engineering*, vol. 35, no. 14-15, pp. 1463–1478, Oct. 2008.

[24] G. D. Backer, M. Vantorre, C. Beels, J. D. Pré, S. Victor, J. D. Rouck, C. Blommaert, and W. V. Paepegem, "Experimental investigation of water impact on axisymmetric bodies," *Applied Ocean Research*, vol. 31, no. 3, pp. 143–156, Jul. 2009.

[25] S. G. Lewis, D. A. Hudson, S. R. Turnock, and D. J. Taunton, "Impact of a free-falling wedge with water: Synchronized visualization, pressure and acceleration measurements," *Fluid Dynamics Research*, vol. 42, no. 3, p. 035509, Mar. 2010.

[26] M. Elhimer, N. Jacques, A. E. M. Alaoui, and C. Gabillet, "The influence of aeration and compressibility on slamming loads during cone water entry," *Journal of Fluids and Structures*, vol. 70, pp. 24–46, Apr. 2017.

[27] N. B. Speirs, J. Belden, Z. Pan, S. Holekamp, G. Badlissi, M. Jones, and T. T. Truscott, "The water entry of a sphere in a jet," *Journal of Fluid Mechanics*, vol. 863, pp. 956–968, Jan. 2019.

[28] B. Güzel and F. C. Korkmaz, "Reducing water entry impact loads on marine structures by surface modification," *Brodogradnja*, vol. 71, no. 1, pp. 1–18, Jan. 2020.

[29] T. T. Truscott, B. P. Epps, and A. H. Techet, "Unsteady forces on spheres during free-surface water entry," *Journal of Fluid Mechanics*, vol. 704, pp. 173–210, Jul. 2012.

[30] D. Li, J. Zhang, M. Zhang, B. Huang, X. Ma, and G. Wang, "Experimental study on water entry of spheres with different surface wettability," *Ocean Engineering*, vol. 187, p. 106123, Sep. 2019.

[31] T. Shepard, J. Abraham, D. Schwalbach, S. Kane, D. Siglin, and T. Harrington, "Velocity and density effect on impact force during water entry of sphere," *Journal of Geophysics & Remote Sensing*, vol. 03, no. 03, 2014.

[32] J.-F. Louf, B. Chang, J. Eshraghi, A. Mituniewicz, P. P. Vlachos, and S. Jung, "Cavity ripple dynamics after pinch-off," *Journal of Fluid Mechanics*, vol. 850, pp. 611–623, Jul. 2018.

[33] *An Assessment of undersea weapons science and technology.* Washington, DC: National Academies Press, jun 2000.

[34] R. T. Knapp, R. T. Dailey, and F. G. Hammitt, *Cavitation.* New York: McGraw-Hill, 1970.

[35] C. Brennen, *Cavitation and bubble dynamics.* New York: Oxford University Press, 1995.

[36] J. G. Waugh and G. W. Stubstad, "Hydroballistics modeling," Naval Undersea Center, Tech. Rep., Jan. 1975.

[37] V. Mathai, R. N. Govardhan, and V. H. Arakeri, "On the impact of a concave nosed axisymmetric body on a free surface," *Applied Physics Letters*, vol. 106, no. 6, p. 064101, Feb. 2015.

[38] *H2a-XLR Hydrophone user's guide*, Aquarian Audio Products, https://www.aquarianaudio.com/AqAudDocs/H2a_XLR_manual.pdf.

[39] M. Minnaert, "XVI. on musical air-bubbles and the sounds of running water," *The London, Edinburgh, and Dublin Philosophical Magazine and Journal of Science*, vol. 16, no. 104, pp. 235–248, Aug. 1933.

[40] *MPU-9250 Product specification*, PS-MPU-9250A-01, Rev. 1.1, InvenSense Inc., https://invensense.tdk.com/wp-content/uploads/2015/02/PS-MPU-9250A-01-v1.1.pdf, Jun. 2016.